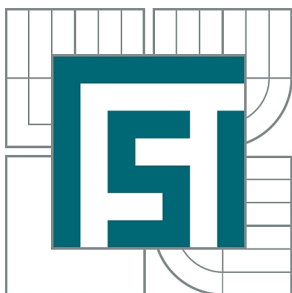




VYSOKÉ UČENÍ TECHNICKÉ V BRNĚ

BRNO UNIVERSITY OF TECHNOLOGY



FAKULTA STROJNÍHO INŽENÝRSTVÍ  
ÚSTAV MATERIÁLOVÝCH VĚD A INŽENÝRSTVÍ

FACULTY OF MECHANICAL ENGINEERING  
INSTITUTE OF MATERIALS SCIENCE AND ENGINEERING

## BIOCERAMIC MATERIALS FOR ADVANCED MEDICAL APPLICATIONS

BIOKERAMICKÉ MATERIÁLY PRO POKROČILÉ LÉKAŘSKÉ APLIKACE

DIZERTAČNÍ PRÁCE

DOCTORAL THESIS

AUTOR PRÁCE

AUTHOR

Ing. LENKA NOVOTNÁ

VEDOUCÍ PRÁCE

SUPERVISOR

prof. RNDr. JAROSLAV CIHLÁŘ, CSc.

BRNO 2015

## **ABSTRACT**

The aim of this thesis was to prepare three-dimensional scaffolds that can be potentially used for the reconstruction and regeneration of damaged bone tissues. Two techniques were used to create the porous ceramic scaffolds – polymer replica technique and polymerization in situ. A variety of bioceramic materials were studied, mainly alumina, zirconia and calcium phosphates. The effect of processing parameters, such as composition of suspensions, as well as the effect of heat treatment on structure and final properties of the prepared scaffolds were evaluated. Morphology of the sintered scaffolds was characterised by scanning electron microscopy; in particular pore size, pores interconnection, total porosity and density were described. Phase composition, compressive strength and biological properties such as bioactivity and cytotoxicity were also discussed.

The dissertation is divided into several sections. The literature review briefly summarizes the structure and properties of bones, the requirements for scaffolds, advantages and disadvantages of currently used materials and methods of ceramic foam preparation. The first part of experiments dealt with scaffolds prepared by polymer replica technique. All fabricated foams had interconnected pores with size in the range of 300 to 2000  $\mu\text{m}$ , total porosity was 50–99%. The compressive strength of calcium phosphate foams prepared by replica technique reached about 0.3 MPa (at 80 % porosity). Reinforcement of the scaffolds was reached by using bio-inert cores or by incorporation of silica into the composite structure. The strength of calcium phosphate/silica scaffold increased above 20 MPa. The last section of experimental part discusses in situ blown calcium phosphate scaffolds, created by using the formation process of polyurethane foam with diisocyanate and polyol components. The sintered scaffolds had mainly interconnected macroporous structure with pore size ranging 80 to 550  $\mu\text{m}$ . The total porosity was about 76 to 99 %. The advantage of this method compared to the polymer replica technique was that the struts were completely filled.

None of the studied materials was cytotoxic and moreover all studied foams exhibited bioactive behaviour. The most promising adept for application in bone tissue engineering seems to be composite material containing calcium phosphates reinforced by silica.

## **ABSTRAKT**

Cílem disertační práce bylo připravit trojrozměrné biokeramické podpůrné systémy („scaffoldy“), které by v budoucnu mohly pomoci při rekonstrukci a regeneraci poškozených kostních tkání. Porézní keramické pěny byly připraveny dvěma způsoby – replikační technikou a polymerizací in situ. Co se složení týče, byly studovány keramické materiály zejména na bázi oxidu hlinitého, zirkoničitého a kalcium fosfátů. Byl studován jednak vliv procesních parametrů jako je složení suspenzí a jejich viskozit, dále pak vliv tepelného zpracování na strukturu a výsledné vlastnosti připravených materiálů. U slinutých pěn byla pomocí rastrovací elektronové mikroskopie hodnocena zejména morfologie – velikost pórů, jejich propojenost a celková porozita, charakterizace mikrostruktury nebyla opomenuta. Dále bylo stanoveno

fázové složení a pevnost v tlaku. Z biologických vlastností byla testována a diskutována bioaktivita a cytotoxicita materiálů.

Disertační práce je členěna do několika částí. V literární rešerši je popsána stavba a vlastnosti kosti, požadavky kladené na kostní náhrady, výhody a nevýhody současně používaných materiálů a způsoby přípravy keramických pěn. Následuje experimentální část, kde byly nejprve studovány pěny připravené replikační technikou. Všechny takto vyrobené pěny měly propojené póry o velikostech 300 až 2000  $\mu\text{m}$ , celková porozita se pohybovala v rozmezí 50 – 99 %. Pevnost pěn na bázi kalcium fosfátů – 0,3 MPa (při celkové porozitě 80%) byla nedostatečná pro kostní náhrady, kde je požadována pevnost větší než 2 MPa. Kalcium fosfátové keramiky byly tedy zpevněny buďto inertním jádrem na bázi oxidu hlinitého nebo ATZ (oxidem zirkoničitým zhouževnatělým oxidem hlinitým). Dále byl připraven částicový kompozit, ve kterém byl hydroxyapatit pojený oxidem křemičitým. Pevnost pěn se podařilo zvýšit až na více než 20 MPa. V poslední kapitole experimentální části byly studovány keramické pěny pěněné in situ, kde byly póry vytvářeny oxidem uhličitým unikajícím během reakce mezi diisokyanátem a polyalkoholem. Po vypálení polymerního pojiva měly pěny propojené póry o průměrné velikosti 80 až 550  $\mu\text{m}$ . Celková porozita se pohybovala v rozmezí 76 – 99%. Výhodou oproti replikační technice byly plné trámečky bez velké středové dutiny vznikající vypálením polymerní předlohy.

Žádný ze studovaných materiálů nebyl pro buňky toxický, navíc všechny studované pěny vykazovaly bioaktivní chování. Z hlediska kostního tkáňového inženýrství se jako nejslibnější jeví kompozitní materiál zpevněný oxidem křemičitým.

## KEYWORDS

Bioceramics, scaffold, calcium phosphates, polymer replica technique

## KLÍČOVÁ SLOVA

Biokeramické materiály, skafold, kalcium fosfáty, polymerní replikační technika

## BIBLIOGRAPHICAL REFERENCE

Novotna, L. *Bioceramic materials for advanced medical applications*. Brno: Brno University of Technology, Faculty of Mechanical Engineering, 2015. 99 p. Supervisor of doctoral thesis prof. RNDr. Jaroslav Cihlář, CSc.

## BIBLIOGRAFICKÁ CITACE

Novotná, L. *Biokeramické materiály pro pokročilé lékařské aplikace*. Brno: Vysoké učení technické v Brně, Fakulta strojního inženýrství, 2015. 99 s. Vedoucí dizertační práce prof. RNDr. Jaroslav Cihlář, CSc.

## **ACKNOWLEDGEMENT**

First, I would like to express my gratitude to my supervisor, prof. Jaroslav Cihlář, for his helpful advice and patience during my PhD studies. I also thank my colleagues for their useful comments and remarks. I am thankful for the help and advice of Dr. Eva Bartoníčková, especially in the beginning of my doctoral studies. Many thanks go to Dr. Zdeněk Chlup who measured the mechanical properties and to Dr. Josef Jaroš who helped me with evaluation of biological properties of silica reinforced scaffolds.

Finally, I would also like to sincerely thank my husband and my parents who have supported me throughout my whole studies.

## **STATEMENT**

I hereby declare that I have written the PhD thesis on my own according to advice of my supervisor prof. Jaroslav Cihlář and that all the literary sources are quoted correctly and completely. This dissertation thesis is the property of the Faculty of Mechanical Engineering in Brno and it can be used for commercial purposes only with consent of the doctoral thesis supervisor and the dean of FME.

Ing. Lenka Novotná

# CONTENT

1	INTRODUCTION .....	1
2	LITERATURE REVIEW.....	2
2.1	Bone structure.....	2
2.1.1	The major components .....	3
2.1.2	Types of osseous tissue .....	4
2.1.3	Mechanical properties of bone .....	5
2.1.4	Principles of bone remodelling and healing.....	7
2.2	Artificial materials for bone tissue engineering.....	8
2.2.1	Requirements for bone scaffold.....	9
2.2.2	Types of biomaterials .....	10
2.2.3	Metals.....	10
2.2.4	Polymers.....	11
2.2.5	Ceramics .....	11
2.2.6	Composites.....	16
2.3	Ceramic foams – processing techniques.....	17
2.3.1	Partial sintering.....	17
2.3.2	Sacrificial fugitives .....	18
2.3.3	Replica technique .....	20
2.3.4	Direct foaming .....	22
2.3.5	Solid freeform fabrication .....	23
3	AIMS OF THE THESIS.....	24
4	EXPERIMENTAL.....	25
4.1	Materials.....	25
4.1.1	Polymer templates .....	25
4.1.2	Ceramic powders.....	25
4.1.3	Binders.....	25
4.1.4	Other materials.....	26
4.2	Methodology .....	26
4.2.1	Characterization of powders, suspensions and sintered scaffolds.....	26
4.2.2	Mechanical testing .....	28
4.2.3	Biological properties.....	29
4.3	Ceramic foam processing .....	31
4.3.1	Polymer replica technique.....	31
4.3.2	CaP scaffold prepared from rigid polyurethane foam .....	35
5	RESULTS AND DISCUSSION .....	37
5.1	Bioactive ceramics based on alumina core .....	37
5.1.1	Characterization of suspensions.....	37
5.1.2	Foam characterisation.....	38
5.1.3	Biological properties – bioactivity testing in simulated body fluid.....	41
5.1.4	Mechanical properties.....	42
5.1.5	Summary of Chapter 5.1.....	43
5.2	Bioactive ceramics based on alumina toughened zirconia .....	44
5.2.1	Characterization of suspensions and sintered scaffolds.....	44
5.2.2	Mechanical tests.....	47
5.2.3	Biological properties.....	48

5.2.4	Summary of chapter 5.2 .....	49
5.3	Calcium phosphate scaffolds .....	50
5.4	Calcium phosphate scaffolds reinforced by silica .....	50
5.4.1	Characterisation of scaffolds – processing parameters .....	50
5.4.2	Phase composition .....	51
5.4.3	Characterisation of structure and morphology of scaffolds .....	54
5.4.4	Characterisation of pore structure of scaffolds .....	55
5.4.5	Biological properties - bioactivity .....	56
5.4.6	Biocompatibility of calcium phosphate scaffolds with human cells .....	58
5.4.7	Mechanical properties.....	61
5.4.8	Summary of Chapter 5.4.....	62
5.5	Calcium phosphate scaffolds produced from CaP / PU composite foam .....	62
5.5.1	Thermal decomposition of CaP / PU scaffold.....	62
5.5.2	Phase composition .....	63
5.5.3	Foam characterisation - influence of chemical composition .....	65
5.5.4	Mechanical properties.....	75
5.5.5	Summary of Chapter 5.5.....	76
6	CONCLUSIONS .....	77
7	REFERENCES.....	79
	List of abbreviations .....	89
	List of figures .....	90
	List of tables.....	93

# 1 INTRODUCTION

The life expectancy increased by about 30 years during the 20th century [1]. This rapid rise has brought new health issues. Nowadays, we face problems relating to numerous bone disorders, thus, the need for load-bearing bone graft substitutes is rising hand in hand with the amount of active elderly people.

Bone is one of the tissues which are able to completely regenerate by themselves, but only in case that the damaged part is small enough. If not, it is necessary to help bone to restore its damaged part by using bone grafts [2]. Currently, a few million people need a bone graft each year [3] and it is expected that the demand will grow steadily.

The best grafts have mechanical and biological properties as similar as possible to those of normal bone. The most suitable properties naturally have autografts, i.e. parts of bone harvested from the patient's own body, usually from an iliac crest. Autografts eliminate a risk of immunogenic rejection; on the other hand, drawbacks are a lack of available material and the necessity of two surgical procedures, leading to more pain and the higher risk of infection. Moreover, up to 30% occurrence of complications was reported [2]. A possible alternative to autografts is using of allografts. The allograft is a bone taken from another patient, usually obtained from a bone bank. Nearly one third of all bone grafts used in North America are allografts [4]. Allografts have osteoconductive properties; however, they carry the risk of infection, rejection and disease transmission. These disadvantages are minimized through a multi-step sterilization process, which leaves most allograft tissues void of its osteoinductive potential and unfortunately also reduces the mechanical properties of the replacement. Because of the above mentioned weaknesses the need for development of a new type of graft is strong and synthetic scaffold seems to be a promising way.

This thesis aims to contribute to the search for a suitable bone substitute. Several types of porous ceramic materials were studied. The first part of the experiments were focused on the scaffolds prepared by polymer replica technique. The objective was to prepare scaffolds with higher strength than the strength of porous hydroxyapatite. Strengthening was achieved by using bio-inert cores and by incorporation of silica into the structure. The second part was oriented toward in situ blown calcium phosphate scaffolds which strength was higher compared to polymer replica technique due to dense struts.

## 2 LITERATURE REVIEW

### 2.1 Bone structure

Bone can be referred to either as an organ or a tissue. Generally, bones are organs made up of bone tissue, bone marrow, blood vessels, epithelium, and nerves, while the term bone tissue specifically refers to the mineral matrix that forms the rigid sections of the organ [5-7]. Bone is one of the hardest tissues in the body — this connective tissue is composed of extracellular matrix and cells (osteocytes, osteoblasts, osteoclasts). Bone serves several functions in the organism: (1) a structural support for the mechanical action of soft tissues, (2) a protection of soft organs and tissues, (3) a source of cells that produce red and white blood cells, and (4) a mineral reservoir [8].

Bones exhibit a complex hierarchical structure (see Fig. 1) which provides unique mechanical, chemical and biological functions. Seven structural levels can be distinguished in bone's structure [9-12]:

- 1) The sub-nano structure (less than a few hundred nanometres): molecular structure of mineral, collagen and non-collagenous organic proteins.
- 2) The nanostructure (0.2–1  $\mu\text{m}$ ): mineralized collagen fibrils.
- 3) The nanostructure (1–10  $\mu\text{m}$ ): fibril arrays.
- 4) The sub-microstructure (3–50  $\mu\text{m}$ ): fibre patterns, single lamellae.
- 5) The microstructure (50–500  $\mu\text{m}$ ): Haversian system, osteons, trabeculae.
- 6) The mesostructure: cortical and cancellous bone.
- 7) The macrostructure: the whole shape of bone.

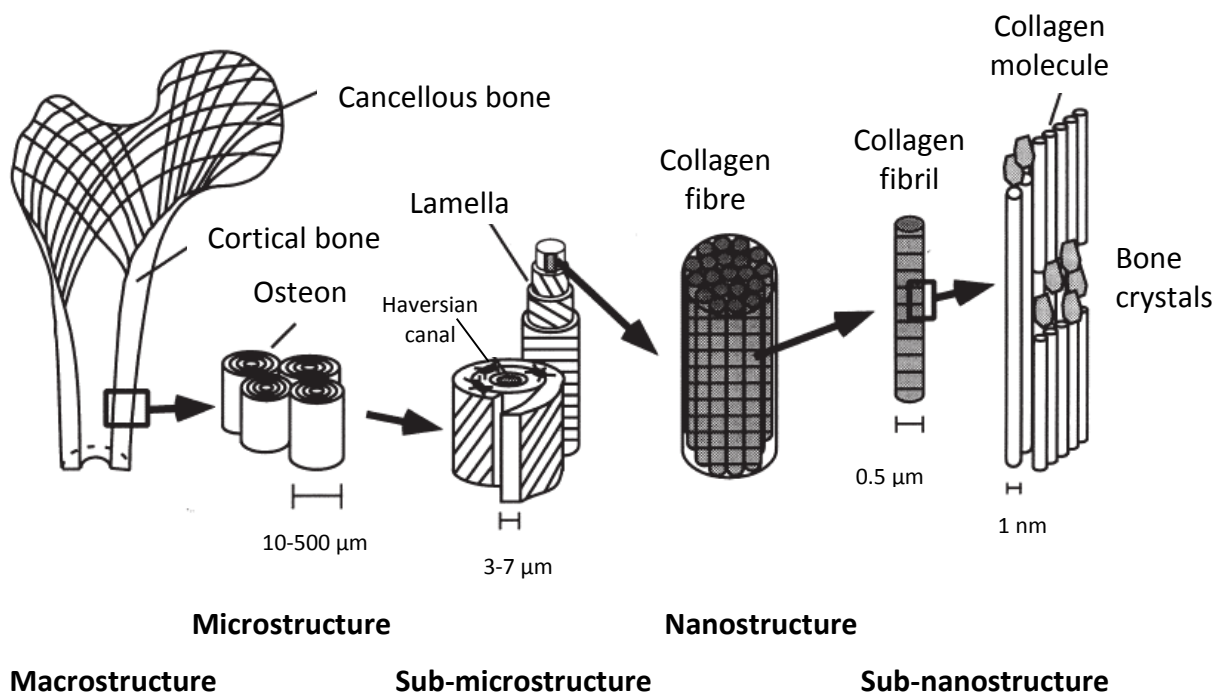
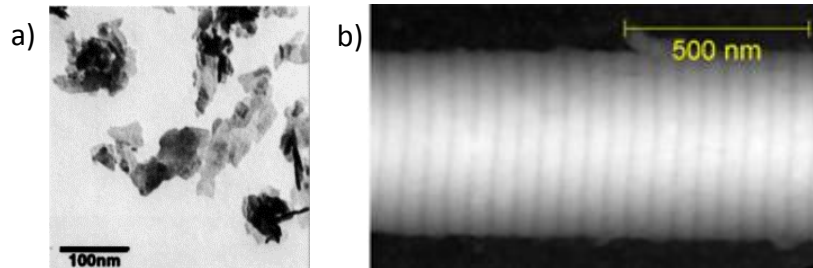


Fig. 1 Hierarchical structure of bone [10].



### 2.1.1 The major components

Three main components can be distinguished at the sub-nanostructure level: (1) small plate-shaped crystals of apatite (see Fig. 2a), (2) macromolecules, of which type I collagen is the major constituent, and (3) water [5].



**Fig. 2** Major components of bone: (a) isolated apatite crystals [11]; (b) collagen fibril [13].

#### **Mineral phase**

The mineral phase represents about two thirds of the weight of a dry bone, or half of its volume [5]. The chemical composition of bone crystals resembles the chemical compositions of stoichiometric hydroxyapatite (HA). The difference is that the biological bone crystals contain significant and varying amounts of carbonate and hydrogen-phosphate ions and less hydroxyl groups than is in the stoichiometric hydroxyapatites [10, 14]. Bone mineral can be thus considered as an impure form of HA, with a variable Ca/P molar ratio in the range 1.6–1.7 (the theoretical value for stoichiometric hydroxyapatite is 1.67) [15].

The general formula of apatites is  $\text{Ca}_{10}(\text{PO}_4)_6\text{X}_2$  where X denotes  $\text{F}^-$ ,  $\text{OH}^-$  (hydroxyapatite) or  $\text{Cl}^-$ . Indexes show that crystallographic unit cell consists of two formula units  $\text{Ca}_5(\text{PO}_4)_3\text{X}$ . As is evident from Fig. 3, hydroxyapatite crystallizes in the hexagonal system.

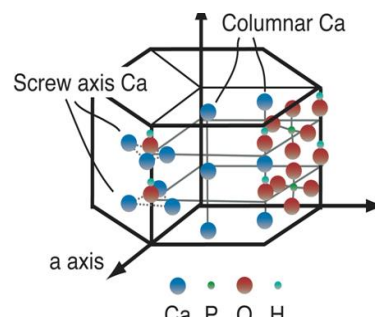


**Fig. 3** Structure of hydroxyapatite [16].

The apatite lattice is prone to substitutions, vacancies, and solid solutions, such as  $\text{CO}_3^{2-}$ ,  $\text{F}^-$ ,  $\text{Cl}^-$ ,  $\text{Na}^+$ ,  $\text{K}^+$ ,  $\text{Fe}^{2+}$ ,  $\text{Zn}^{2+}$ ,  $\text{Sr}^{2+}$ ,  $\text{Mg}^{2+}$  and citrate [17]. A bone apatite contains about 7–7.5 wt. % of carbonate which dominantly substitutes  $\text{PO}_4^{3-}$  ion [5, 17, 18]. Wopenka [17] documented that carbonate substitution in hydroxyapatite causes changes in several physical properties; a drop of the thermal stability and reduced crystallite volume was observed; the a–axial length decreases whereas the c–axial length increases compared to non-substituted ceramic apatites. Another consequence of substitution is that the carbonate-containing apatite has higher solubility compared to the carbonate-free

apatite because the  $\text{Ca-CO}_3^{2-}$  bond is weaker than the  $\text{Ca-PO}_4^{3-}$  bond. Furthermore, simultaneous presence of other substituting ions influences the morphology of biologically produced apatite which forms nanocrystalline blocks or platelets. Contrary, synthetically and geologically formed apatite usually occurs in the shape of prisms and needles [17].

The documented dimensions of apatite crystals in bone are following: the length of 30–50 nm, width of 15–30 nm and thickness of 2–10 nm [11, 19]. AFM studies revealed that the bone crystals may be longer than those observed by TEM, with widths and lengths ranging from 30 to 200 nm [20].

### **Collagen framework**

The organic matrix of the bone consists of collagen (85–90 %) and a series of non-collagenous proteins and lipids. The collagen (type I) molecules secreted by osteoblasts are self-assembled into fibrils. Each fibril consists of three (two  $\alpha_1$  and one  $\alpha_2$ ) polypeptide chains about 1000 amino acids long which are wound together in a triple helix. A triple-helical molecule is cylindrically shaped with an average diameter of around 1.5 nm, and lengths of 300 nm (see Fig. 4). The fibrils are all parallel with their ends separated by gaps of about 35 nm; furthermore, the neighbouring triple-helical molecules are offset or staggered by 67 nm [11, 21-23].

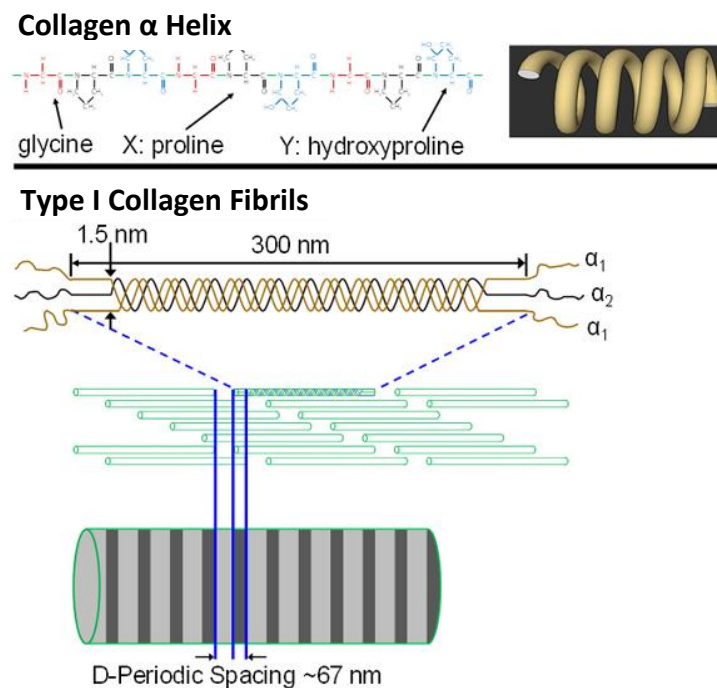


**Fig. 4** Collagen: from top to bottom—collagen  $\alpha$ -helix composed of amino acids, single triple-helical molecule, 2-dimensional section through part of a fibril showing the staggered array, a collagen fibril [13].

### **2.1.2 Types of osseous tissue**

At the mesostructure level bone exists in two forms: cortical (also known as compact or dense) and cancellous (known as spongy, or trabecular) bone. Long bones consist of a dense

cortical shell with a porous, cancellous interior (see Fig. 5); whilst flat bones such as the calvaria have a sandwich structure; two thin layers of compact bone enclosing between them a variable quantity of cancellous bone [24].

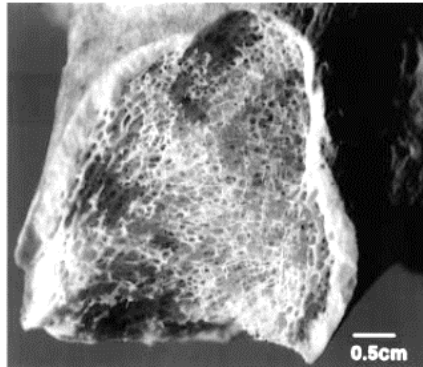


**Fig. 5** Fracture surface of human femur [11].

Cortical and cancellous bones can be distinguished by the porosity or more precisely by means of histological evaluation. The porosity of the compact bone is about 5–30 %, the porosity of the cancellous bone varied between 30–90 % [25]. In general, cancellous bones are much more metabolically active, thus they are remodelled more often than cortical bones. The cancellous bone is composed of a network of trabeculae that make the overall organ lighter and allows enough free space for blood vessels and marrow. Even though cancellous bone accounts only 20 % of total bone mass, it covers nearly ten times the surface area of compact bone [4, 9, 10, 21, 23].

### 2.1.3 Mechanical properties of bone

Estimation of mechanical properties of bone is a quite challenging issue. Mechanical properties vary not only from place to place, patient to patient; they are influenced by age, gender and health of donor, by the freshness of samples, mineral and water content, and so on [26]. In general, bone is an anisotropic material with different properties in longitudinal and transverse directions. Mechanical properties of bone depend especially on the degree of mineralization and porosity of the matrix. Generally, the bone matrix is more mineralized and thus stiffer and more brittle when the human gets older [27].

#### **Modulus**

Bone can be simply considered as a fibre composite; hereby the Young's modulus can be calculated using the rule of mixtures (eq. 1) and the inverse rule of mixtures (eq. 2):

$$E_{ax} = f \cdot E_f + (1 - f) \cdot E_m, \quad (1)$$

$$E_{trans} = \left[ \frac{f}{E_f} + \frac{(1-f)}{E_m} \right]^{-1} \quad (2)$$

where *ax* means axial and *trans* transverse,  $E_f$ ,  $E_m$  are Young's Modulus of fibres and matrix,  $f$  is volume fraction of fibres [26]. These equations show that bone is stiffer in the axial direction, parallel to the osteons. The measured modulus in axial direction

is considerably lower, because collagen fibres are not oriented parallel to the axis and bone mineral do not form a continuous matrix.

The Young's modulus is mainly a function of bone density [27]. In theoretical calculations, pores can be considered as the third phase. As is obvious from the Table 1, the Young's modulus of cortical bone is one order of magnitude higher than the cancellous bone one. The measured values decrease with a temperature increase; and the modulus is highly dependent on the strain rate (the modulus is increasing with an increasing strain rate) [26].

The elongation of bone is only 0.2–4.5% in case of cortical bone and 1.5–7 % in case of trabecular bone [26, 28].

**Table 1** Young's modulus of bone and its components (GPa) [26-29].

Material	Young's modulus (GPa)	Density ( $\text{g}\cdot\text{cm}^{-3}$ )
Collagen (dry)	6	1.33
Hydroxyapatite	80	3.16
Cortical bone, longitudinal direction	11–21 (up to 55)	2.5
Cortical bone, transverse direction	5–13	2.5
Cancellous bone	0.01–0.5	0.2-2

### **Strength**

The human skeleton is a highly organized system, accordingly to functions. Particular bones in the body need to withstand different mechanical forces, so there is a huge variation in measured values of all tensile, compressive, shear, torsional, and bending strength of bones (see Tab. 2) [27]. Bone is the strongest in compression, the weakest in shear, and, intermediate in tension. Bones must be loaded constantly, in order to perform their functions and to be able to remodel, and thus remain healthy. If they are under-stressed for prolonged periods of time, they become thinner and less strong (in case of bed ridden patients or astronauts). Oppositely, higher levels of stress lead to increase of bone mass. In general strength decreases when a person gets older [26].

**Table 2** Strength of bone [26, 27].

Strength	Longitudinal	Transverse
Tensile strength (MPa)	60–70 (femur: 89–118)	approx. 50
Compressive strength (MPa)	70–280 cortical bone	approx. 50
Compressive strength (MPa)	0.2–20 cancellous bone	
Bending strength (MPa)	approx. 76, resp. 28–281 (femur)	
Torsional strength (MPa)	65–71 (femur)	
Flaking strength (MPa)	116 (femur)	40–92 (femur)

### **Fracture toughness**

The fracture toughness of living bone is excellent, the fracture energy ( $G_c = 1.5 \text{ kJ}\cdot\text{m}^{-2}$ ) is nearly comparable to steel [27]. As well as other mechanical properties, the measured value is depended on the measuring direction. Higher values of fracture toughness have been obtained in the transverse direction because of the unique hierarchical structure, where the canal inside the osteon can stop vertical external crack by lowering the critical

stress-intensity constant at the crack tip. The lower fracture toughness in longitudinal direction can be moreover explained by the presence of the cement lines, which are the weakest parts of the structure [30]. The fracture toughness of cortical bone is typically in the range 2–12 MPa·m<sup>1/2</sup> [29].

Bones naturally exhibit several toughening mechanisms, which are shown in Fig. 6. At the lowest level, plasticity is achieved through the mechanisms of molecular uncoiling and intermolecular sliding of molecules of collagen. On the scale of the fibril arrays, microcracking and fibrillar sliding act as plasticity mechanisms. At micrometre dimensions, the breaking of sacrificial bonds at the interfaces of fibril arrays leads to increased energy dissipation, together with crack bridging by collagen fibrils. In the range of tens to hundreds of micrometres, the fracture energy is reduced by the crack deflection [12, 30].

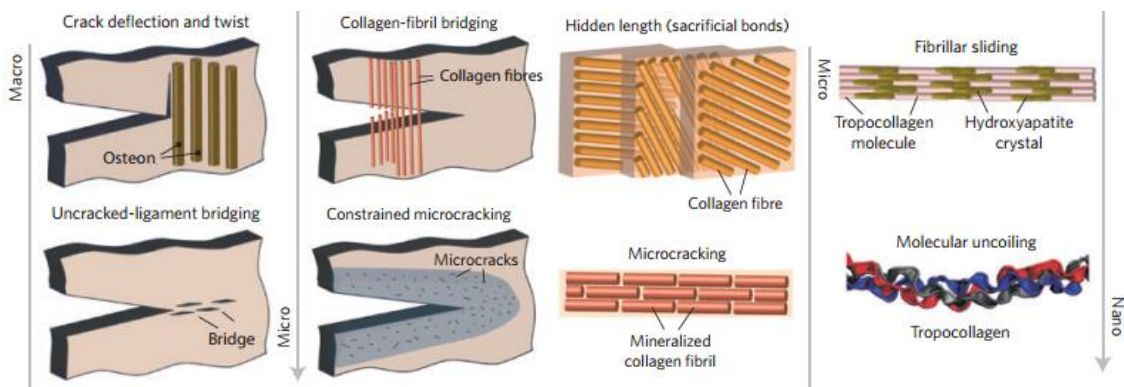


Fig. 6 The prevailing toughening mechanisms from the nano to macro structure [12].

## 2.1.4 Principles of bone remodelling and healing

### *Bone remodelling*

Bone is a dynamic living tissue which constantly undergoes remodelling. The remodelling cycle (see Fig. 7) lasts around 6 months. About 10 % (25 % of trabecular bone while only 3 % of cortical bone) of the skeleton is renewed by remodelling each year [31].

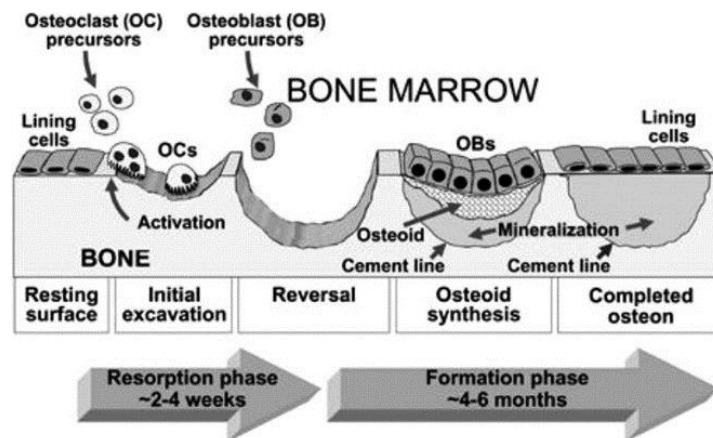
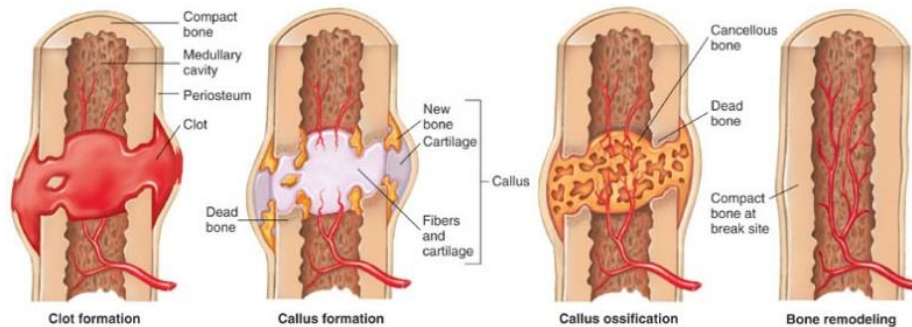


Fig. 7 Scheme of bone remodelling process [32].

The old bone is removed by osteoclasts whereas new tissue is formed by osteoblasts. Osteoclasts dissolve the mineral phase via locally decreasing pH, resulted a small cavity created on the surface. Subsequently, bone forming cells called osteoblasts begin to fill in the cavity with the osteoid which mineralized in new bone tissue [32]. Osteoblasts activity decreases with age leading to imbalance of resorption and formation of new bone.

### ***Bone healing***

The body begins the healing process immediately after the breaking a bone. A clot forms at the site of the fracture within 48 to 72 hours after the injury, resulting in an inadequate blood supply that leads to the local bone necrosis. The dead cells provoke migration of fibroblasts and osteoblasts to the fracture site (within 3 days to 2 weeks). A fibrocartilaginous soft callus is formed around the fracture side (within 2 to 6 weeks). The callus is then transformed into hard bone callus (within 3 weeks to 6 months); excessive material of the bone is resorbed. Fig. 8 summarizes the stages of bone healing. Healing takes from about 6 weeks (young, healthy adult) to 3–6 months (older person with reduced bone mass) [24].



**Fig. 8** Schematic illustration of the bone healing process [24].

## **2.2 Artificial materials for bone tissue engineering**

Tissue engineering is a multidisciplinary field involving material sciences, life sciences, medicine and clinical practice to solve the critical medical problems, such as tissue loss and organ failure. Before a more detailed description of tissue engineering, it is useful to define basic terms that are often confusing: osteoconduction, osteoinduction, osteoproduction, osteogenesis and osseointegration.

**Osteoconduction** is a process whereby microscopic and macroscopic scaffolding is provided for inward migration of cellular elements involved in bone formation. An **osteoconductive** material permits bone growth on its surface or down into pores or channels and thus help the reparative growth of the natural bone [33].

**Osteoinduction** is a process which encouraging undifferentiated cells to differentiate into active osteoblasts under the influence of a diffusible Bone Morphogenetic Protein, the type of growth factor [33].

The term **osseointegration** means the formation of a direct interface (without intervening soft tissue) between an implant and bone. Nowadays, an implant is considered to

be osseointegrated when there is no progressive relative movement between the implant and the bone in direct contact [34].

**Osteoproduction** is the ability of directly producing bone via the existence of bone-forming cells within the graft. It is a combination of osteoinductive, osteoconductive, and/or osteogenic properties of a grafting material [35, 36].

**Osteogenesis** means that new bone can be formed from the transplanted living cells [37].

### 2.2.1 Requirements for bone scaffold

Currently used implants usually lack three important characteristics of living tissues: (1) the ability to self-repair; (2) the ability to maintain a blood supply; and (3) the ability to modify their structure and properties in response to environmental factors such as mechanical load [38]. Nowadays, the goal of bone tissue engineering is not to permanently replace the damaged bone tissue by synthetic scaffold, but provide a support for its regeneration as long as necessary. The scaffold should help to stimulate bone growth and attract newly formed bone tissue, before being remodelled [38].

Because a human body is a complex and sensitive system, the requirements for scaffold materials are manifold and extremely challenging. The ideal scaffold for bone tissue engineering should meet the following criteria [39]:

The **biocompatibility** is an essential property; it means that the material must not elicit an inflammatory response nor demonstrate immunogenicity or cytotoxicity.

The scaffolds are artificial, lattice-like structures capable of supporting a tissue formation. This **three dimensional structures** are typically engineered with pores allowing cells to migrate throughout the material and support vascularization of the ingrown tissue. A blood supply in and around the implant would be created within a few weeks after implantation.

Pores should be interconnected with **pore size** minimally 100  $\mu\text{m}$  in diameter (ideally about 150 - 500  $\mu\text{m}$ ) [40, 41]. Besides macropores, microporosity of the walls (< 100  $\mu\text{m}$ ) is desirable because it provides a larger surface area which is significant for protein adsorption, cellular adhesion and proliferation [41].

Besides that, scaffolds should be further able to create a **stable interface** with the host bone without fibrous connective tissue. Its surface texture should promote cell adhesion and adsorption of biological metabolites [42]. In addition, it should support cell differentiation and proliferation [38].

Over a few months' time, the scaffold ought to **resorb** in the body, leaving behind the natural tissue. Resorption kinetics should be equal to the bone repair rate in order to facilitate load transfer to developing bone. The by-products must not be toxic and should be easily eliminated via the respiratory or urinary systems [43].

Above that, **mechanical properties** of the scaffold must be sufficient and the scaffold must not collapse during handling and *in vivo* during the normal physical activities. Mechanical

properties should be ideally similar to those of the host bone to avoid several problems such as stress shielding. Stress shielding occurs if the Young's modulus of an implant is higher than that of bone. If it happens, the implant carries nearly all the load, the result bone becomes weaker, and the interface between the bone and the implant deteriorates [36]. The optimal Young's modulus of dense implant should be in range 15–20 GPa or 0.1–2 GPa in the case of cellular scaffolds. Compressive strength should be 100 to 200 MPa, or 2 to 20 MPa respectively. Last but not least, scaffolds should be **easily manufactured** in desired shapes which would match the defect in the bone.

Hence, the intrinsic structure as well as the composition plays critical roles in the success of a scaffold.

### 2.2.2 Types of biomaterials

In general, scaffolds are made of organic or inorganic materials. Up to date, the most published papers in the field of biomaterials deal with polymers [41].

A material that would meet all requirements for an ideal bone graft has not been developed so far. Metals, for example, exhibit mechanical properties appropriate for load bearing applications but their biocompatibility is not satisfactory. Ceramic materials are on the other hand usually biocompatible, sometimes even bioactive; however, their innate brittleness limits their widespread. Polymeric porous scaffolds can be resorbable *in vivo* but they have insufficient stiffness and compressive strength... Similar as in bone, it is convenient to combine different groups of materials with the aim to increase the mechanical stability of the scaffold and improve the tissue interaction. In the last decade, there have been many efforts to develop scaffolds with a drug-delivery capacity. These scaffolds can locally release growth factors or antibiotics to enhance bone ingrowth to treated bone defects and thus support wound healing. Various types of materials were intensively studied.

### 2.2.3 Metals

The main advantage of metal implants is their superior mechanical properties, such as high tensile strength and fatigue resistance. Metals are so far the most often implanted material for load bearing applications. Disadvantages are the lack of tissue adherence and the risk of toxicity due to accumulation of released metal ions [41, 44]. Moreover, the higher Young's modulus induces stress shielding.

Commonly used metals are stainless steel or titanium alloys (such as Ti-6Al-4V). Titanium and its alloys are usually used for internal and external fixation and for hard tissue replacements of bones, joints and dental implants. The benefit of titanium is a spontaneous formation of protective titanium oxide on its surface. Porous metallic scaffolds are made of titanium, tantalum or magnesium [3, 44]. Magnesium alloys can degrade *in vivo* by MgOH which can temporarily enhance osteoblast activity [2]. Metallic grafts have few indications such as in spine surgery [45].



## 2.2.4 Polymers

Organic materials are the most studied group of biomaterials mainly because of their biocompatibility or sometimes even bioactivity or biodegradability [2]. Polymers can be both naturally derived and synthetic origin. Natural polymers used for scaffolds are collagen, fibrin, alginate, silk, hyaluronan, and chitosan [44]. Commonly used synthetic polymers are poly(lactic acid) (PLA), poly(glycolic acid) (PGA), their copolymer (PLGA), polyethylene glycol (PEG) and polycaprolactone (PCL), poly(propylene fumarate) (PPF) [46]. An advantage of synthetic polymers is a tuneable biodegradation and highly predictable properties [41]. Scaffolds with different porosities and surface characteristics can be processed by different techniques such as gas foaming, emulsion freeze drying, porogen leaching, thermally induced phase separation, supercritical fluid processing, nanofibre electrospinning process, and 3D printing [47, 48].

Polymers degrade *in vivo* primary by chemical reactions like hydrolysis and only slightly by enzymatic and cellular pathways. Degradation of certain polymers (such as PLA, PGA) is associated with an increasing acidity of local environment which can negatively influence tissue responses [46]. Some of the degradation products may even cause immunological reactions. Polymers exhibit several problems such as absence of direct bone bonding and integration. Young's modulus (7 MPa for elastic polymers and 4 GPa for stiff polymers) is lower than that of bone [41]. Polymers usually do not reach sufficient mechanical stability and thus cannot be used for load bearing applications [2, 41, 45].

A more detailed description of purely organic materials is behind the scope of this thesis and can be found elsewhere [48-51].

## 2.2.5 Ceramics

Oxide ceramics typically exhibit an excellent biocompatibility. According to the level of interaction with tissues, Hench [36] divided materials into the following categories: (1) nearly inert, (2) porous, (3a) bioactive class A, (3b) bioactive class B, and (4) resorbable. The level of bioreactivity is illustrated in Fig. 9.

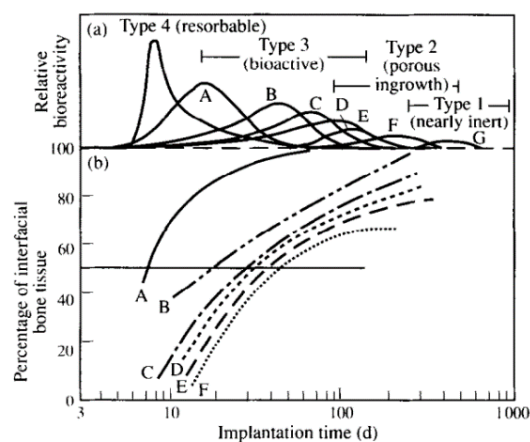


**Fig. 9** Classification of bioceramic implants according to the bioreactivity and time dependence of formation of bone bonding at an implant interface: (A) 45S5 Bioglass, (B) Mina13 Ceravital, (C) 55S4.3 Bioglass, (D) A/W glass-ceramics, (E) HA, (F) KGy213Ceravital, (G)  $\text{Al}_2\text{O}_3\text{-Si}_3\text{N}_4$  [36].

### ***Bioinert ceramics***

In fact, no material implanted into living tissues is strictly inert. A tissue tends to encapsulate the implant by a non-adherent fibrous layer. The interface is neither chemically nor biologically bonded so micromotion can occur. Bioinert ceramics are often used for articulating surfaces because of their excellent tribological properties.

- Alumina

Alumina has found applications in tissue engineering since 1970s [52]. It is mainly used for load-bearing hip prosthesis or dental implants. More than 10 million alumina femoral heads were implanted by 2006. Alumina implants are usually made of very fine grained polycrystalline alumina; chemically, they are compounded of highly pure (99.5%)  $Al_2O_3$  with a small amount of MgO which serves as a grain-grow inhibitor. Alumina exhibits excellent biocompatibility and wear resistance however flexural strength is only moderate and fracture toughness is quite low [52]. Mechanical properties are listed in Table 3

- Zirconia

Zirconia [53] is a material with undoubtedly best mechanical properties among other bioceramics. It has relatively high flexural strength, lower modulus than alumina, and due to stabilization of tetragonal phase excellent fracture toughness (see Table 3). Zirconia can be stabilized by e.g. Y, Mg, Ca, Ce oxides. Tetragonal phase is usually stabilized by 3 mol % of  $Y_2O_3$ . A disadvantage of Y-ZrO<sub>2</sub> is aging which occurs in body fluids. The aging results in a slightly decrease of strength and fracture toughness [52]. Typical applications in biomedicine are similar to alumina.

**Table 3** Mechanical properties of bioinert ceramics [52, 53]

Material	Density (g·cm <sup>-3</sup> )	Compressive strength (MPa)	Young modulus (GPa)	Fracture toughness (MPa·m <sup>1/2</sup> )	Temp. coeff. (ppm/°C)	Hardness (HV 0.1)	Fr. surface energy (J·m <sup>-2</sup> )
Al <sub>2</sub> O <sub>3</sub>	3.85-3.99	3000-5000	380-410	3-6	6-9	2200	7.6-30
PSZ	5.6-5.89	1850-2000	195-210	5-8	7-10	1200	160-350
TZP	5.6-5.89	1850-2000	195-210	7-10	11	1200	160-350

### ***Bioactive ceramics***

Hench defined the concept of bioactivity in 1971 as follows: “A bioactive material is one that elicits a specific biological response at the interface of the material which results in the formation of a bond between the tissues and the material” [54]. A common characteristic of bioactive ceramics and glasses is a time-dependent kinetic modification of the surface that occurs after implantation. The bonding interface with tissues is provided by a biologically active layer of hydroxy carbonate apatite (HCA) created on the surface. The HCA phase formed on bioactive implants is chemically and structurally close to the mineral phase in bone. The HCA is the only common characteristic of all the known bioactive implant materials. The *in vivo* formation of an apatite layer on the surface of bioactive ceramics can be reproduced *in vitro* by a protein-free and acellular simulated body fluid (SBF), which has an ion concentration similar to the human blood

plasma [36]. For more detailed information see Chapter 4.2.3. The rate of development of the bond is described by level of bioactivity  $I_B$ , which is related to the time when more than 50% of the interface is bonded [36].

Hench distinguished two types of bioactive materials: (A) class A, osteopductive materials which can directly bond to both hard and soft tissue and (B) class B, osteoconductive materials which elicits only an extracellular response at its interface. Only a few bioglasses belong to class A [36].

- Calcium phosphates substituted by silica

Silica-based materials have many applications in medicine and biotechnology, e.g. for bone-repairing devices [55-61], drug delivery systems [62] and cancer therapies [63-66]. Especially silica-based glasses became due to their bioactivity the most widely investigated materials for tissue regeneration during the last 40 years [55, 56]. Detailed information can be found in one of the very nice reviews written by father of bioglass, Larry Hench [67-69].

- Bioactive glass

Bioactive glass was discovered by Hench in 1969. It exhibits an excellent biocompatibility as well as the bone bonding ability. Through interfacial and cell mediated reactions, bioactive glass develops a calcium deficient, carbonated phosphate surface layer that allows chemically bonding to host tissue. Bioactive glasses furthermore support enzyme activity, vascularization, osteoblast adhesion, growth, differentiation; and induce the differentiation of mesenchymal cells into osteoblasts [29].

Nearly all bioactive glasses are composed of  $\text{SiO}_2$ ,  $\text{Na}_2\text{O}$ ,  $\text{CaO}$ , and  $\text{P}_2\text{O}_5$ . Commonly used 45S5 Bioglass contains 45 wt%  $\text{SiO}_2$ , 24.5 wt%  $\text{Na}_2\text{O}$ , 24.5 wt%  $\text{CaO}$  and 6 wt%  $\text{P}_2\text{O}_5$  [58]. Bioglasses are by bioactivity level divided into several groups. According to Fig. 10, glasses in the centre (red region) have the highest level of bioactivity, i.e. they are class-A bioactive. Glasses of compositions in region B are only osteoconductive.

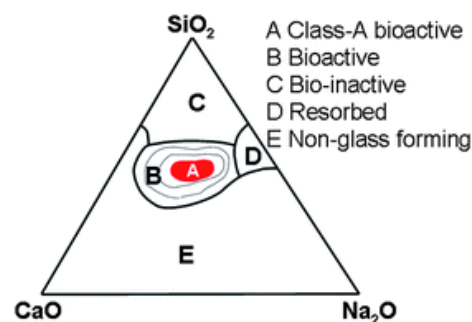


**Fig. 10** Phase diagram of bioglasses, 6 wt%  $\text{P}_2\text{O}_5$  [70].

Bioglasses are biologically active in case of containing vitreous phase. If they are in region E of Fig. 10 they are crystallized and thus bioinert. This limits their application as scaffold materials, because full crystallization happens prior to densification by viscous flow sintering. Extensive sintering is necessary to densify the struts of a scaffold to achieve the required mechanical properties.

Overall, mechanical properties are not good (see Table 4). Fracture toughness (approximately  $1 \text{ MPa}\cdot\text{m}^{1/2}$ [71]) and mechanical strength are low, especially in porous form, hence, bioactive glasses cannot be used for load-bearing applications.

- Glass-ceramics

The glass-ceramics is a material which is obtained by using of an appropriate thermal treatment of glass that results in the nucleation and growth of specific crystal phases within the residual vitreous matrix. In general, mechanical properties are improved compared to the bioglass (see Table 4). The oldest type is Ceravital glass-ceramic which bioactivity is two times lower than that of bioglass of similar composition [72].

Apatite-wollastonite (A/W) glass-ceramic is composed of oxyfluorapatite, wollastonite ( $\beta\text{-CaSiO}_3$ ) and vitreous phase. Bending strength and fracture toughness of A/W glass-ceramics is improved because of the precipitation to wollastonite as well as apatite phases [29].

**Table 4** Mechanical properties of bioglass and glass-ceramics [73].

	<b>Bioglass 45S5</b>	<b>Ceravital</b>	<b>A/W</b>
Flexural strength (MPa)	42	100-150	220
Compressive strength (MPa)	160-190	500	1060
Young's Modulus (GPa)	35	100-159	118

- Hydroxyapatite

Hydroxyapatite is a non-resorbable calcium phosphate. Due to chemical composition and crystallography similarity to bone mineral, hydroxyapatite exhibits an excellent biocompatibility, and therefore it is extensively studied for bone tissue substitutions. Despite not being osteoinductive, hydroxyapatite is osteoconductive and able to directly bond to bone. HA enhance the attachment, differentiation, and proliferation of relevant cells (such as osteoblasts and mesenchymal cells). Its application in bone tissue engineering is, however, limited due to low mechanical strength and very slow biodegradation. The dissolution rate of synthetic HA is depended on the crystallinity, porosity and composition (impurities) of the HA phase; type, concentration and pH of the solution, degree of the solution saturation, solid/solution ratio, etc. Crystalline HA exhibits the slowest degradation rate of all other calcium phosphates

Mechanical properties are influenced by porosity, crystallinity, grain size, and composition as well. The stiffness, strength and toughness can be enhanced by using crystalline, low porous small-grain-sized HA. Compared to a cortical bone, compressive strength of synthetic HA is higher, however, fracture toughness is significantly lower due to missing collagen fibres [29]. Mechanical properties are summarized in Table 5.

**Table 5** Mechanical properties of calcium phosphates [74].

	<b>K<sub>1c</sub> (MPa<sup>m</sup><sup>1/2</sup>)</b>	<b>strength (MPa)</b>	<b>Vickers hardness</b>
Hydroxyapatite [74]	0.9	50-60	500
Dense HA [75]	1	compressive: 430-920 tensile: 17-110	500
Tricalcium phosphate	1.3	50-60	900

### ***Resorbable bioceramics***

Resorbability is the important parameter in bone tissue engineering. Ceramic scaffold should degrade in desired time, i.e. when the newly formed tissue is strong enough to withstand the applied load. Unfortunately, no material has fulfilled this criterion yet and thus mechanically unstable bone defects have to be temporary stabilized with a non-resorbable metallic fixation [3]. In that case, the mechanical properties of graft are then the minor issue and the most important characteristic becomes the resorption rate of the graft.

Resorption rate of scaffolds is controlled by two main approaches: (1) by optimization of geometry. A key feature is the presence of sufficiently large interconnected pores to enable the invasion of blood vessels and cells, hence enabling biodegradation of material and bone ingrowth. (2) By modified chemistry, which can influence the thermodynamic stability, in particular the solubility [3].

- *Bioactive glass*

One of the main advantages of bioactive glasses is controlled range of chemical properties and thus the rate of bioresorption. It is possible to design the degradation properties of glasses specific to a particular application of bone tissue engineering. Glasses with compositions in region D of Fig. 10 are being resorbed in tissue within 10–30 day-long period [72].

- *Tricalcium phosphate (TCP)*

In the field of calcium phosphate materials, there has been a shift of interest from hydroxyapatite, to chemically more reactive compounds such as composites between HA and  $\beta$ -tricalcium phosphate (so-called “biphasic calcium phosphates” – BCP),  $\beta$ -TCP,  $\alpha$ -TCP, octocalcium phosphate (OCP), dicalcium phosphate dihydrate (DCPD) and anhydrous dicalcium phosphate (DCP) [3].

The dissolution rate of calcium phosphates decreases in the following order:

Amorphous HA >  $\alpha$ -TCP >  $\beta$ -TCP > Crystalline HA [29, 76].

Calcium phosphate is *in vivo* resorbed by the action of osteoclasts. These cells can dissolve calcium phosphate by local change of pH due to releasing small amounts of hydrochloric acid at the surface [3, 77]. Calcium phosphate is the only type of material whose degradation products can be used for new bone formation [3].

Tricalcium phosphates (TCP,  $\text{Ca}_3(\text{PO}_4)_2$ ) can be found in three modifications:  $\alpha$ ,  $\beta$  and  $\alpha'$ .  $\alpha'$ -TCP exists only above 1430 °C, below the transition temperature it transforms into  $\alpha$  phase.  $\beta$ -TCP is stable at room temperature and transforms to  $\alpha$ -TCP at 1125 °C.  $\alpha$ -TCP is thermodynamically metastable below that temperature, and it can be retained during cooling to room temperature. Impurities of Mg, Sr and Zn substituting calcium stabilize the  $\beta$ -phase, whereas small amounts of Si substituting phosphorus stabilize the  $\alpha$ -phase [78].

$\alpha$ - and  $\beta$ -TCP have different structure, density and solubility, which determine their biological properties and applications. Both are used in several clinical applications:  $\beta$ -TCP serves as the component of commercial bioceramics, whereas  $\alpha$ -TCP is the major constituent of the powder component of bone cement [76].  $\alpha$ -TCP is non-toxic, osteoconductive and bioactive ceramics, it crystallizes in the monoclinic space group. It is an interesting material due to its biodegradability; it resorbs faster than HA,  $\beta$ -TCP and BCP

Biphasic calcium phosphate combines compounds with different solubility.  $\beta$ -TCP resorbs 10-20 times faster than crystalline HA; it takes about six to 18 months [77]. The optimal dissolution rate *in vivo* can be tuned by combination of different ratios of HA and  $\beta$ -TCP in BCP.

## 2.2.6 Composites

Composite materials advantageously combine properties of at least two types of materials to enhance mechanical and biological properties of the whole scaffold to bring it near demands of the host tissue. The dispersed phase is usually harder whereas the matrix serves as a stress transfer medium. Composites are categorized into (1) particle- or (2) fibre-reinforced and (3) structural composites [41]. A prediction of final properties can be made by the “rule of mixtures”. Commonly fabricated composites use polymer matrix and ceramics as the reinforcing phase.

Composites demonstrate improved compressive load-bearing capabilities, bioactivity and host-implant interface [41]. Different groups of materials can be arbitrarily combined. Clinical relevance has mainly the polymer/ceramic system. An advantage of this system is optimal elastic modulus which can be comparable with that of bone. The core can be polymeric and shell can be ceramic and vice versa.

### ***Ceramics/polymer composite***

Johnson and Tavakley [79] patented a system with polymeric core (PLA, PGA, PLGA, natural polymers) coated with calcium phosphate outer layer which facilitates the cell attachment. This composite with a huge surface area can be used as cartilage substituent. [80]. Wang et al. [37] studied the hydroxyapatite-polyamide structure with mechanical strength comparable to bone. He prepared nano HA/PA porous scaffold by thermally induced phase inversion. Another possible approach to obtain composite structure is via biomimetic process. Porous PLLA was soaked in simulated body fluid to allow development of apatite throughout the scaffold. The formation of HA was enhanced by hydrolysis and nucleation [81].

Polymer/ceramic composite can be also easily obtain be soaking of calcium phosphate ceramics in adequate polymer such as PGA. If the crack propagates, the polymer matrix bridges the strain.

### ***Ceramic/ceramic composite***

Various ceramic materials have different properties. Bioactive ceramics is usually weak and brittle and vice versa zirconia exhibits outstanding strength and fracture toughness even though its surface is nearly inert, leading to *in situ* slippage. Hence it is convenient to coat it by bioactive material such as calcium phosphate.

Zhang [82] patented ceramic material with gradient structure where elastic modulus increased toward the core. Composite was based on (Y-, Mg-, Ce-, Ca-) stabilized zirconia which was subsequently infiltrated by glass-ceramic phase. After the infiltration of glass, the strength of composite increased three times compared to pure zirconia. This material above that, exhibited lower elastic modulus and bioactive surface.

Kim et al. [83, 84] prepared zirconia foams with bioactive hydroxyapatite layer. He overcame the problem with insufficient direct bonding between zirconia and HA by more stable fluoroapatite interlayer. Miao et al. [85] studied zirconia (with addition of alumina) with hydroxyapatite-borosilicate glass coatings. The porous ceramics had compressive strengths of 5.3 to 36.8 MPa and Young's moduli of 0.30–2.25 GPa, favourably comparable to the mechanical properties of cancellous bones.

## **2.3 Ceramic foams – processing techniques**

In the early days of ceramic processing, the goal was to eliminate pores from the ceramic structure and thereby partially overcome the Achilles' heel, inherent brittleness. On the other hand, porous (cellular) ceramic materials have many special properties which cannot be achieved by their dense counterparts. Ceramic foams are nowadays widely used as filters, absorbents, catalysts and catalyst supports, lightweight structural components and thermal insulators [86, 87].

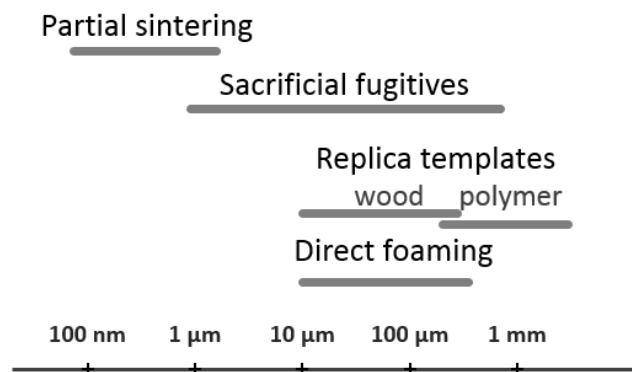


**Fig. 11** Classification of processing methods by pore size [88-90].

Fig. 11 gives an overview of processing techniques of porous ceramics: (1) partial sintering, (2) sacrificial fugitives, (3) polymer replica technique, (4) direct foaming and (5) solid freeform fabrication.

### **2.3.1 Partial sintering**

Partial sintering is the simplest method suitable for processing of structures with randomly arranged irregular pores (see scheme in Fig. 12).

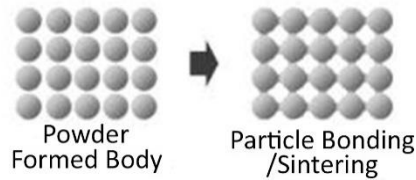


**Fig. 12** Scheme of fabrication process by partial sintering [88].

Pore size and porosity can be controlled by the pore size of a raw powder and by sintering conditions (lower temperature and shorter time than required for full densification [88]). The particle size of starting powder should be two to five times larger than the desired pore size. The final porosity is usually lower than 50 % [88-90]. The resulting pores are too small to allow bone tissue penetrate inside, thus this technique cannot be used separately in tissue engineering. However, it can be convenient to combine this method with another because the rough surface can help to attach cells or signal molecules [90].

### 2.3.2 Sacrificial fugitives

Porous ceramics can be fabricated by mixing of an appropriate amount of sacrificial fugitives with a ceramic powder, as shown in Fig. 13. The porosity of thus prepared ceramics is ranging between 20 % and 90 %, pore size varies between 1  $\mu\text{m}$  and 700  $\mu\text{m}$ , the drawback of this method can be poor interconnectivity [89].

The biphasic composite containing a continuous ceramic matrix and a homogeneously dispersed sacrificial phase is usually prepared by (1) pressing of a powder mixture of the two components, (2) slip, tape or direct casting of two-phase suspension, or (3) impregnation of previously consolidated preforms of the sacrificial material with a preceramic polymer or ceramic suspension [89]. Pore forming agents can be synthetic organic matters (polymer beads), natural organic matters (starch, sucrose [91], gelatine, cellulose), inorganic matters (nickel, carbon, glass particles, etc.) and liquid (water) [88].

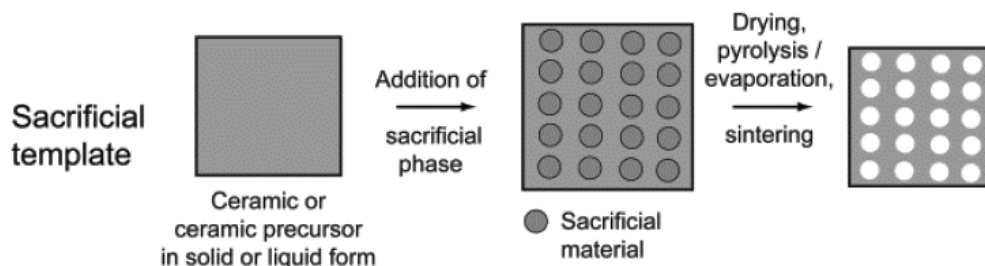


**Fig. 13** The scheme of sacrificial fugitive method [89].

Organic fugitives are usually extracted by pyrolysis (200 - 600  $^{\circ}\text{C}$ ). During this process, the huge amount of generated gas can lead to a crack formation, therefore burning rate must be slow enough [88]. Ceramic and metallic particles are usually extracted by chemical way (e.g. by acidic leaching). Before the removal of the sacrificed template, the continuous matrix must be at least partially consolidated. If not, the structure could collapse. Consolidation can be achieved by binders, setting agents or alternatively by the sol-gel transition. In case of preceramic polymers, the consolidation is achieved by macromolecules linking at temperatures slightly below pyrolysis temperature.



Ceramic structure with small pores can be obtained by incorporation of oil into aqueous or non-aqueous emulsion by simple agitation or mixing [92]. Very small pores are achieved using immiscible liquids having low interfacial energy. The template is subsequently removed under mild conditions [89]. Sacrificial template method can be used for scaffold fabrication as well. Descamps et al. [93] prepared gradient structure from TCP and PMMA beads by slip casting (Fig. 14). They achieved higher interconnectivity of the pores due to heat treatment of PMMA beads. The necks between particles were formed during the dwell at 180 °C [93, 94].

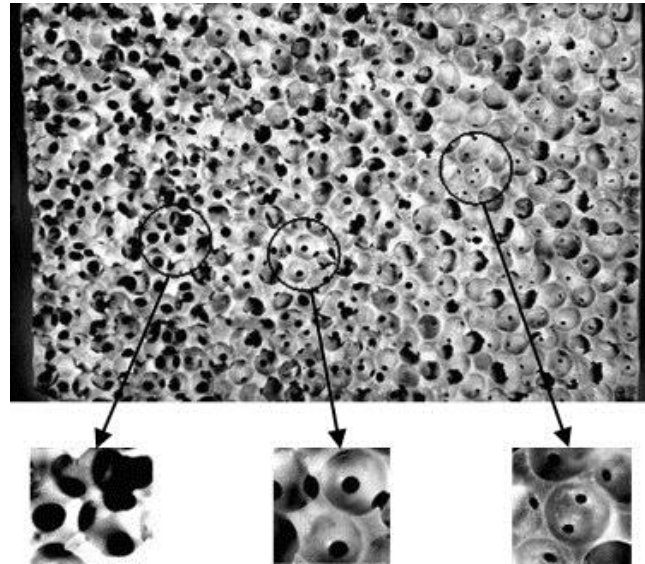


**Fig. 14** Gradient macroporous foam prepared from  $\beta$ -TCP and PMMA balls of 600-700  $\mu\text{m}$  [93].

As was previously mentioned, using liquid as a sacrificial fugitive is very promising. An example of this method is freeze casting which is widely used for preparation of bioactive scaffolds based on calcium phosphates (microstructure is presented in Fig. 15).

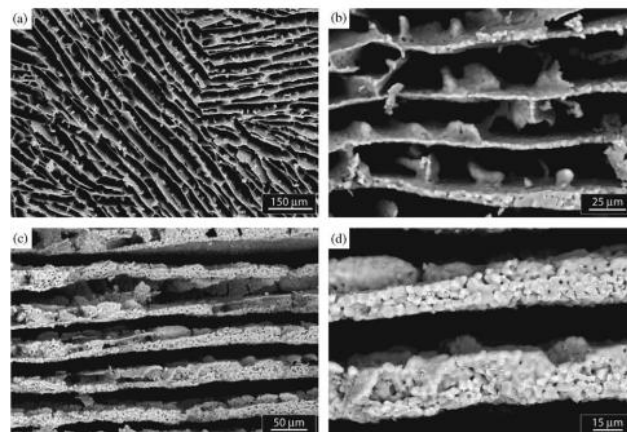


**Fig. 15** Microstructure of porous HA samples with 64% porosity [95].

The principle of this method is using water or a high-melting point oil (such as camphene [96]) as sacrificial material. The suspension is subjected to unidirectional freezing, wherein the ice crystals are formed. The dendritically oriented ceramic phase is obtained after sublimation of the ice under vacuum [97]. Advantages are following: simple sintering without necessity of template burnout, anisotropic morphology, environmentally friendliness.

Porosity level is controlled by concentration of suspension, however, it is difficult to obtain pores larger than 10  $\mu\text{m}$  [38]. So prepared scaffolds exhibit excellent compressive strength. Deville et al. [95] prepared HA scaffolds with unusually high compressive strength: 145 MPa at 47% porosity and 65 MPa at 56% porosity.

### 2.3.3 Replica technique

This technique is based on impregnation of a cellular structure with a ceramic slurry in order to obtain the ceramic structure exhibiting the same morphology as the original template (as shown in Fig. 16). Templates can be either synthetic or natural origin. The method was developed in the early 1960s; since then it has become the most popular method and that is why it is still extensively used in industry mainly to prepare ceramic filters for molten metal filtration.

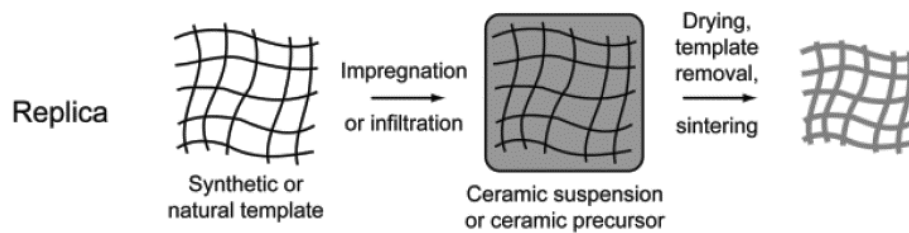


**Fig. 16** The scheme of replica technique [89].

Cellular ceramics obtained by this method are characterized by a reticulated structure of highly interconnected pores within the range 200  $\mu\text{m}$  to 3 mm. The overall open porosity vary between 40 % and 98 %. The smallest pore size which can be achieved by this method is limited to 150  $\mu\text{m}$  [86, 88, 89].

#### ***Synthetic template***

Replicating the polymeric template is the easiest way how to obtain ceramics with the desirable pore size. The procedure consists of several steps, the polymeric sponge (typically polyurethane) is soaked into a suspension, the redundant suspension is then removed by rollers or by centrifuge. The suspension should have an optimal viscosity to avoid dripping and simultaneously to be easily partially removed under the shearing conditions, in other words, thixotropic behaviour is needed. According to the literature, best results were obtain using suspensions which viscosities decreased from 10–30 Pa·s at a shear rate of 5  $\text{s}^{-1}$  down to 1–6 Pa·s at a shear rate of 100  $\text{s}^{-1}$  [98]. After dipping in the suspension, the coated template (see Fig. 17) is being dried and subsequently pyrolysed. Heating rates should be lower than 1  $^{\circ}\text{C}/\text{min}$  to avoid cracking of the coated struts due to decomposition and diffusion of the template material. Binders and plasticizers added to the suspension can help the struts to prevent cracking. Colloidal aluminium orthophosphate, potassium and sodium silicates, hydratable alumina, colloidal silica, polyvinyl butyral and polymerizable monomers are often used as binders. After the template-burnout, the ceramics is finally sintered at optimal temperature in an appropriate atmosphere. Replica technique can be applied to a variety of materials which are able to be dispersed into a suspension. In some cases, mainly in Si-C based ceramics, the suspension can be replaced by preceramic polymers [89].

Even though this method is quite easy and versatile, the drawback is lower mechanical properties than would be expected. It is caused by hollow struts which remain after polymer removal during sintering. If the layer is too thin or if the heating rate is not slow enough the layer can moreover crack during pyrolysis of the template. It has been made several attempts to overcome this disadvantage. As is known, strength increases with wall thickness, so the strut size can be increased by repeating the impregnating of the polymeric template and drying several times. Alternatively, it is possible to recoat the pre-sintered ceramic foam by a low viscosity suspension [99]. Strength can be also enhanced by immersion of sintered ceramics in a suspension containing colloidal oxides, which can due to their small dimension easily penetrate into the structure and there filled micro-cracks [86].

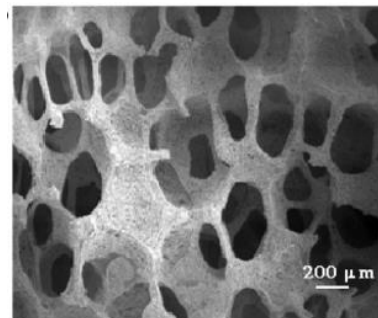


**Fig. 17** Polyurethane sponge impregnated by bioglass [100].

### ***Natural templates***

As was previously mentioned, not only synthetic polymer templates can be replicated. The main advantage of natural templates is their complicated, often hierarchical, morphology which can be hardly produced artificially. **Corals** have been used as natural template since 1970s. Their structure has been replicated through a lost-wax method. First step involves impregnation by wax under vacuum. After wax hardening, the calcium carbonate is leached out using a strong acidic solution. The negative wax model is subsequently impregnated with a ceramic suspension. The organic material is then removed by pyrolysis. Another approach is direct conversion of the cellular structure of corals into hydroxyapatite by hydrothermal treatments at high temperature and pressure. It occurs in a phosphate solution where the carbonate ions from  $\text{CaCO}_3$  are replaced by phosphate ions from hydroxyapatite.

Another very interesting and for tissue engineering promising approach is to mimic structure of **wood** (see Fig. 18). Anisotropic aligned pores copying oriented vessels in the wood are a benefit of this method. The preparation is quite time-consuming procedure requiring several steps. First step involves heat treatment of the wood structure under inert atmosphere at temperatures within 600–1800 °C. The resulting carbon cellular preform is subsequently infiltrated by gases or liquids at high temperatures or by liquid sols at room temperatures. The latter approach needs subsequent oxidation to render the ceramics. The microstructure of prepared ceramics is very close to the original wood template. Pores are much smaller than in case of using polymer templates. They vary from 10 up to 300 μm. The porosity is ranging from 25 to

95 %. The mechanical properties are anisotropic due to anisotropic structure of wood cells. The strength in the axial direction is higher than that in the perpendicular direction. Mechanical properties might be degraded similar as in the case of synthetic template due to flaws in struts generated during the pyrolysis [89, 101, 102].

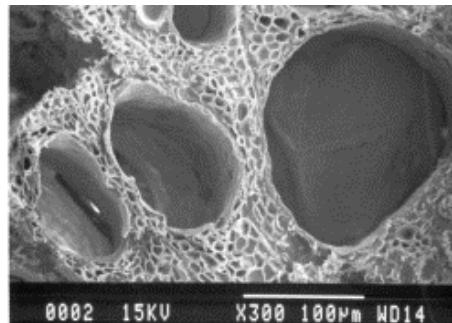


**Fig. 18** SEM image of ceramics derived from oak [102].

### 2.3.4 Direct foaming

The direct foaming is a technique based on incorporation of a gaseous phase into a ceramic suspension through mechanical frothing or gas released by chemical reaction. The procedure which is illustrated in Fig. 19 allows low-cost and easy production of open or close-cells ceramic foams with wide pore size distribution between 10  $\mu\text{m}$  and several mm (usually 10 - 300  $\mu\text{m}$ ) [89]. Porosity, proportional to the amount of gas incorporated into the suspension, lies between 45 % and 95 %.

Critical issue of direct foaming is the stabilization of the bubbles in the suspension. Gas bubbles tend to coalesce in thermodynamically unstable wet foam in order to reduce the total Gibbs free energy of the system. To avoid large pores in the final ceramics it is necessary to stabilize gas bubbles with surfactants or surface modified particle. Surfactants are classified as non-ionic, anionic, cationic or protein.

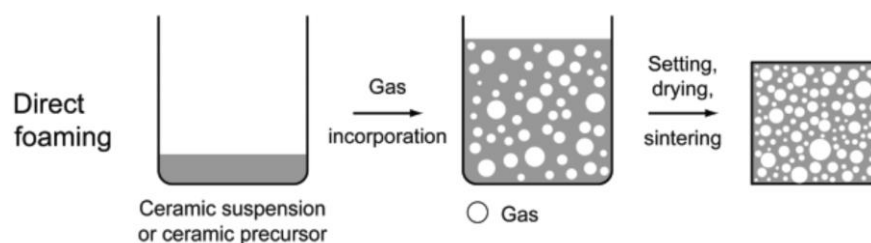


**Fig. 19** Scheme of direct foaming [89].

Another direct foaming technique is based on emulsifying a homogeneously dispersed alkane or air-alkane phase in the stabilised aqueous powder suspension. Foaming is made due to evaporation of alkane droplet.

Fig. 20 presents three stages of foaming process: (a) alkane emulsion in the powder suspension, (b) transition of emulsion to wet foam and (c) transition to stable foam – formation of polyhedral structure [103].

The advantage of direct foaming is a final structure with dense ceramic struts which exhibit only limited amount of defects. For example, compressive strength of alumina can

reach about 16 MPa at 88% porosity [88]. By this method it is also possible to prepare porous structures with a graded porosity. This method is not suitable for processing of large sample sizes because of cracking problems which usually occurs during a drying/sintering step [104].

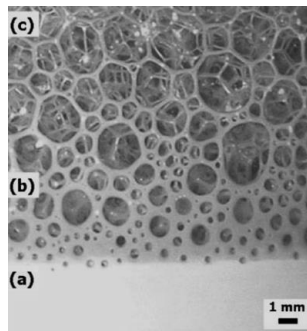


**Fig. 20** Alumina foam prepared by direct foaming of emulsified ceramic powder suspensions [103].

### 2.3.5 Solid freeform fabrication

Solid freeform fabrication (SFF) (often referred as rapid prototyping) is a technique which is able to quickly produce complex 3D objects without the need of using moulds or other forming tools. Ceramic bodies are formed directly based on data generated by CAD systems. An image of a bone defect in a patient can be acquired by e.g. computer tomography. A 3D CAD computer model is then developed from this scan. A common feature is that the CAD model is sliced and the ceramic body is built layer by layer [105, 106].

The mostly used techniques in rapid prototyping are: (1) 3D printing (3D-P), (2) direct ink-jet printing, (3) stereolithography, (4) fused deposition modelling, (5) robocasting and (6) selective laser sintering / melting (SLS / SLM).

3D powder bed printing consists of several steps. Initially, one thin layer of powder, such as calcium phosphate, is smoothly dispersed on a platform. A suitable binder is subsequently printed into the powder bed to bind the desired particles within the layer. Next layer is dispersed on top of the first layer. The printed binder binds the particles of the second layer and to the previous bound layer. The whole scaffold is shaped layer by layer by this way. Binder is finally removed at high temperature during consolidation [2]. This procedure is exemplified in Fig. 21.

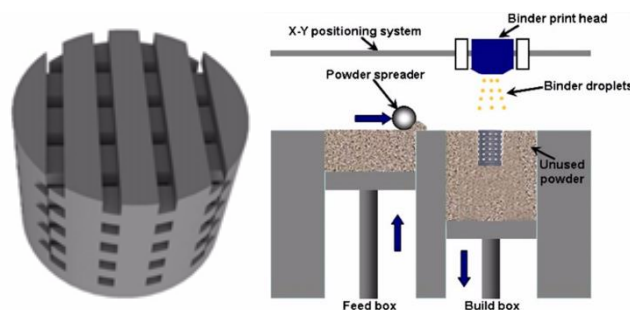


**Fig. 21** Solid freeform fabrication: (a) CAD image of porous scaffold, (b) schematic drawing representing the 3D printing process [107].

SLM technique works on a similar principle with the difference that the particles are not bonded by printed binder, but directly sintered using a laser [2].

### **3 AIMS OF THE THESIS**

In accordance with the literature search, the following objectives of the thesis have been established. The main goal was to prepare porous ceramic materials with sufficient mechanical and biological properties that could potentially serve as substitutes of hard tissues.

To solve this goal, research was divided into the following steps:

- Development of ceramic foams with hierarchical porosity up to pore sizes 1500  $\mu\text{m}$  via replication technique. One approach included composite ceramic scaffolds with enhanced mechanical stability due to strong bioinert core based on alumina and/or zirconia. The second approach was focused on development of fully bioactive ceramic scaffolds based on calcium phosphates.
- Development of bioactive scaffolds by burning out the organic compounds from in situ blown polyurethane / calcium phosphate composite.
- Study of mechanical and biological properties of the prepared scaffolds.

## 4 EXPERIMENTAL

### 4.1 Materials

#### 4.1.1 Polymer templates

Reticulated polyester based polyurethane foams with open cell structure were used as templates for processing of ceramic scaffolds by polymer replica technique. Commercial polymer foams Bulpren (Eurofoam, Czech Republic) of five different pore sizes were chosen (see Table 6). Foam structure was entirely open and did not contain any closed cells, same as cancellous bone. Templates of different shapes (blocks, cylinders) and dimensions were prepared for mechanical and biological testing.

**Table 6** Polymer templates and their characterisation

Type	Pores per inch (ppi)	Cell diameter ( $\mu\text{m}$ )
Bulpren S 31048	90	440 - 520
Bulpren S 31062	75	520 - 720
Bulpren S 28089	60	740 - 1040
Bulpren S 28133	45	1080 - 1580
Bulpren S 28190	30	1650 - 2150

#### 4.1.2 Ceramic powders

Three different oxides and two calcium phosphate commercial powders were used in the experiments.

White fused corundum F1200 (Koltex, Czech Republic), grain size 2.1  $\mu\text{m}$  (sieve sizes of FEPA grit F1200). Chemical analysis: 99.5 wt. %  $\text{Al}_2\text{O}_3$ , 0.07 wt. %  $\text{Fe}_2\text{O}_3$ , 0.056 wt. %  $\text{SiO}_2$ , 0.21 wt. %  $\text{Na}_2\text{O}$ .

Synthetic alumina RC HPDBM (Malakoff Ind., US), grain size 0.5  $\mu\text{m}$ , specific surface area 7.4  $\text{m}^2\text{g}^{-1}$ . Chemical analysis: 50 ppm Fe, 30 ppm Na, 45 ppm Si, 45 ppm Ca.

Yttria stabilized zirconia HWY5.5 SD (Guang Dong Huawang Materials, China). Specific surface area 11  $\text{m}^2/\text{g}$ , grain size 2.8  $\mu\text{m}$ . Chemical analysis: 5.5 wt. %  $\text{Y}_2\text{O}_3$ , < 150 ppm  $\text{SiO}_2$ , < 50 ppm  $\text{Fe}_2\text{O}_3$ , < 50 ppm  $\text{TiO}_2$ , < 50 ppm  $\text{Na}_2\text{O}$ .

Hydroxyapatite p.a. (Fluka, Switzerland);  $\text{Ca}_5(\text{PO}_4)_3(\text{OH})$ , HA, assay > 90%; average size of agglomerates 18.5  $\mu\text{m}$ ; specific surface area: 33.8  $\text{m}^2/\text{g}$ .

Beta-tricalcium phosphate p.a. (Fluka, Switzerland);  $\text{Ca}_3(\text{PO}_4)_2$ , assay > 97%; mean size of agglomerates 7.7  $\mu\text{m}$ ; specific surface area: 1.6  $\text{m}^2/\text{g}$ .

#### 4.1.3 Binders

Powders were bonded by polymeric binders (PVA, PVB) or by colloidal solutions ( $\text{AlOOH}$ ,  $\text{SiO}_2$ ).

Disperal P3 no.10090 (Condea Chemie GmbH, German), highly dispersible alumina powder-boehmite ( $\text{AlOOH}$ ) of grain size 2.6 nm, specific surface area 330  $\text{m}^2/\text{g}$ , chemical

analysis: 20 ppm Na<sub>2</sub>O, 100 ppm Fe<sub>2</sub>O<sub>3</sub>, 120 ppm SiO<sub>2</sub>, 4% NO<sub>3</sub>.

Ludox SK-R (Grace, U.S.), colloidal silica, average grain size 12 nm; specific surface area: 230 m<sup>2</sup>/g, pH 7.

Butvar B79 (PVB, Solutia Inc., US), 88% polyvinylbutyral, 11% polyvinyl alcohol, max 2.5% polyvinyl acetate.

Polyvinylalcohol – Mowiol 4–88, Mowiol 10–98 and Mowiol 20–98 (Sigma Aldrich, Germany). Molecular weight and hydrolysis degree are shown in Table 7.

**Table 7** Types of PVA and their molecular weight and degree of hydrolysis

	Molecular weight	Hydrolysis (mol%)
Mowiol 4–88	~ 31,000	86.7–88.7
Mowiol 10–98	~ 61,000	98.0–98.8
Mowiol 20–98	~ 125,000	98.0–98.8

#### 4.1.4 Other materials

Besides powders and binders, other additives such as plasticizers, deflocculate or defoaming agents were added to prepare stable suspensions. Diisocyanate and polyol were used for in situ blown polyurethane /calcium phosphate composites.

n-Octanol (C<sub>8</sub>H<sub>18</sub>O, Lachema, Czech Republic) used as defoaming agent in PVA suspensions.

Glycerol (Onex, Czech Republic) served as plasticizer in PVA suspensions.

Dolapix CE64 (Zschimmer Schwarz, Germany). The dispersing and deflocculating agent.

Ongronat<sup>®</sup> 2500 MDI (BorsodChem Zrt., Hungary). MDI (2,2' / 2,4' and 4,4'- methylene diphenyl diisocyanate) is an aromatic isocyanate and a key polyurethane raw material containing 30.5 %NCO. Ongronat is suited for the manufacture of rigid foams, structural foams and adhesives.

Polyol Stepanpol PS-2412 (Stepan Company, US). STEPANPOL PS-2412 is a modified phthalic anhydride-based aromatic polyester polyol designed for use in rigid foam applications. Hydroxyl number is 230-250 mg KOH/g, water content is max 0.15 wt. %.

Solvents: isopropanol (p.a.; Lach-Ner, Czech Republic) and deionized water (0.1 μS/cm<sup>2</sup>).

## 4.2 Methodology

All methods used in the experiments described in Chapter 5 are summarized below.

### 4.2.1 Characterization of powders, suspensions and sintered scaffolds

#### *Specific surface area*

Specific surface area, S<sub>BET</sub>, of the starting and heat treated powders was evaluated via nitrogen adsorption by ChemBET 3000 (Quantachrome, USA) device. Specific surface area



value can be recalculated into approximate diameters of the ball shaped particles according to the equation (3).

$$D_{BET} = \frac{6}{S_{BET} \cdot \rho_{theor}} [m] \quad (3)$$

### ***Thermal analysis***

Thermal analysis, was performed by 6300 Seiko Instruments TG-DTA. The measurement was conducted in the temperature range between 35 and maximally 1200 °C in argon or in a mixture of air and argon in a ratio of 1:1, flow rate was set to 400 ml / min, temperature increase was 2 °C/min.

### ***Zeta potential***

Zeta potential, a key indicator of the stability of colloidal dispersions, was measured in aqueous dispersions by using Zetasizer 3000 HS (Malvern Instruments, UK).

### ***Rheological properties***

Viscosity of the prepared sols and slurries was measured using a rotary rheometer Mars II Haake (Thermo Scientific, US). Viscosities were determined in concentric cylinder arrangement with the shear rate range 0.5–1000 sec<sup>-1</sup>.

### ***Particle size distribution***

Distribution of particle sizes was determined by laser diffraction on LA 950 (HORIBA, Japan) device. The agglomerates were broken by US before the measuring.

### ***XRD analysis***

Phase composition before and after sintering was determined by X-ray diffractometers SmartLab 3kW (Rigaku, Japan) and PANalytical X'pert (Philips, Netherlands). Evaluation of crystallographic structure was carried out by the Rietveld method.

### ***Scanning electron microscopy***

The morphology of powders and structure of sintered scaffolds were observed using scanning electron microscopy (ZEISS Ultra Plus, Germany, Tescan VEGA TS5136XM, Czech Republic and Philips XL30, Netherlands,).

### ***Light microscopy***

The morphology of scaffolds at magnification below 100× was registered by DinoLite digital camera AM4115ZTL (DinoLite, Netherlands).

### ***Porosity***

The porosity of scaffolds was determined by several methods. Total porosity was calculated from the geometric volume, the mass and the theoretical density as follows [108]:

$$P = \frac{\rho_t - \rho_b}{\rho_t} \times 100\%, \quad (4)$$

where  $\rho_t$  is the theoretical density and  $\rho_b = \frac{m_b}{V_b}$  is the bulk density,  $m_b$  is the mass of

the dry test piece and  $V_b$  is the total geometrical volume (the sum of the volumes of the solid material, the open pores and the closed pores).

The bulk density of struts was determined via Archimedes' principle (EN 623-2) with distilled water [108].

Image analysis was used to determine the porosity of struts, the total porosity and pore (cell) sizes and their distribution. The samples were embedded in a resin, cut, ground and polished by standard ceramographic methods. The pore size was estimated by image analysis of scaffold cross-sections. At least four photographs were acquired by SEM for each sample. Image analysis was done by ImageJ software (National Institutes of Health, US). Fig. 22 gives an overview of image analysis routine. For further analysis it was necessary firstly convert image to binary representation by tresholding. The total porosity was calculated as the count of pixels that represented pores (black pixels). Pore sizes were calculated after the image segmentation by watershed algorithm, a strong tool for separating touching convex shapes. Areas of individual sphere cross-sections were measured and equivalent diameters were calculated.

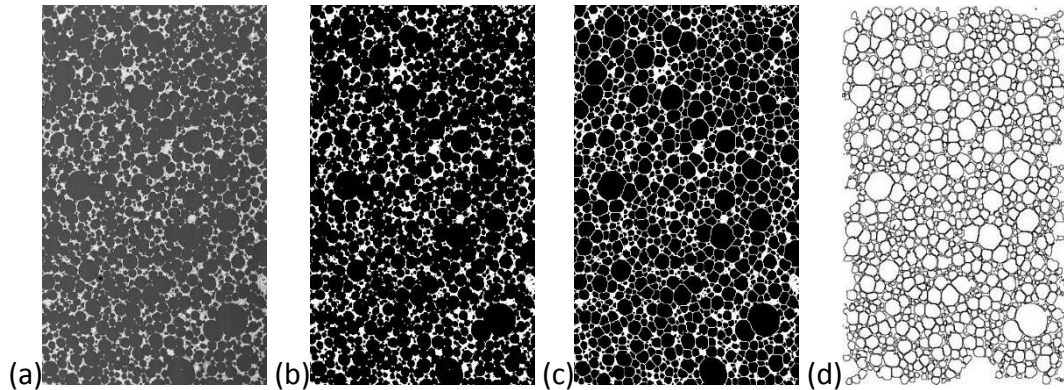


**Fig. 22** Overview of the image analysis process: (a) acquired image, (b) threshold image, (c) applied watershed algorithm, (d) identified pores.

The image analysis data were based on only 2D random sections, pore sizes and their distribution in 3D would differ. The real pore size distribution would be broader because the spheres are rarely cut in the centre. The true 3D mean pore diameter was determined applying simple stereological correction factor 0.785 [109]

$$D_{sphere} = \frac{D_{circ}}{0.785} = 1.274 \cdot D_{circ} , \quad (5)$$

where  $D_{circ}$  is the average circular segment diameter.

## 4.2.2 Mechanical testing

### *Compressive strength*

Mechanical properties of prepared foams were determined using a compression test. High-Precision Electric Actuator Systems 8862 (Instron, US) equipped with 5 kN load cell and precise clip-gauge for the deformation measurement was employed for the loading. Samples were inserted between compressive platens where for better load transfer was inserted also slice of silicone rubber having thickness of 1 mm. An optical system

consisting of Canon D40 camera was sometimes used for recording of damage development during loading and fracture mechanism observation. During the test, high resolution photos of the specimen side were being taken with the interval of 5 seconds. The crosshead speed of 0.5 mm/min was used for loading in all tests. The compressive strength was determined from the maximal obtained force. The loading was stopped when deformation achieved certain value and debris were further investigated by means of light and electron scanning microscopy.

### 4.2.3 Biological properties

#### *Bioactivity testing in SBF solution*

According to Kokubo and Takadama [110], “the essential requirement for a material to bond to living bone is the formation of bone-like apatite on its surface when implanted in the living body”. The *in vivo* apatite formation can be reproduced in a simulated body fluid (SBF), which is an acellular solution of ionic composition (Table 8) similar to human blood plasma however, it lacks many elements such as proteins, CO<sub>2</sub>, and other organic molecules which play an important role in material behaviour *in vivo* [111].

**Table 8** Nominal ion concentrations (in mM) of SBF in comparison to the human blood plasma [110].

	Na <sup>+</sup>	K <sup>+</sup>	Mg <sup>2+</sup>	Ca <sup>2+</sup>	Cl <sup>-</sup>	HCO <sub>3</sub> <sup>-</sup>	HPO <sub>4</sub> <sup>2-</sup>	SO <sub>4</sub> <sup>2-</sup>	pH
Blood plasma	142.0	5.0	1.5	1.5	103.0	27.0	1.0	0.5	7.2–7.4
SBF	142.0	5.0	1.5	2.5	147.8	4.2	1.0	0.5	7.4

The solution was prepared according to the corrected Kokubo recipe [110]. Briefly, 8.035 g NaCl, 0.355 g NaHCO<sub>3</sub>, 0.225 g KCl, 0.231 g K<sub>2</sub>HPO<sub>4</sub>·3H<sub>2</sub>O, 0.311 g MgCl<sub>2</sub>·6H<sub>2</sub>O, 39 ml HCl, 0.292 g CaCl<sub>2</sub>, and 0.072 g Na<sub>2</sub>SO<sub>4</sub> were dissolved one by one in 700 ml H<sub>2</sub>O at 36.5 °C. Tris-hydroxymethyl aminomethane ((HOCH<sub>2</sub>)<sub>3</sub>CNH<sub>2</sub>) (Tris) was added into the solution little by little until the pH reached 7.45, then was lower to 7.42 by dropping 1M HCl; this was repeated until all Tris (6.118 g) was dissolved. When pH was finally adjusted to 7.40 at 36.5 °C, solution was cool down to 20 °C and deionised water was added to 1000 ml. It was necessary to precisely follow the instructions to avoid precipitation of a supersaturated solution. Samples were soaked in SBF at 36.5 °C for 7, 14 and 28 days. After removal from the solution and rinsing with deionized water, the samples were dried at room temperature. The presence of the apatite layer on the surface (see Fig. 23) was examined using scanning electron microscopy and confirmed by energy-dispersive spectroscopy.

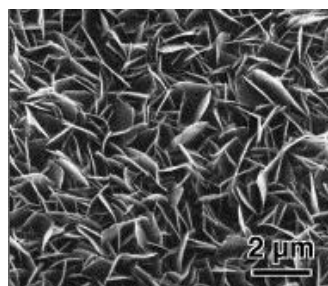


**Fig. 23** SEM image of HA layer created on the surface after immersion in the SBF [111].

The weight of dry test samples was measured before and after the test. The tested material was considered as bioactive in case that the apatite layer was formed on the surface.

### ***Cytotoxicity***

Cytotoxicity of materials was tested *in vitro* using direct contact assay according to EN ISO 10993-5 specifications [112]. Scaffolds or dense discs were sterilized in autoclave for 20 min at 121 °C. Human osteosarcoma cells of cell line MG63 (from European Collection of Cell Cultures) were cultivated at 37 °C in 5 % CO<sub>2</sub> in Eagle Minimum Essential Medium (EMEM) with high glucose, 1 % L-Glutamine, 1 % non-essential amino acids (NEAA), 10 % fetal bovine serum, 1 % antibiotics and 0.3 % gentamicin. Cell line was then inoculated into a measured amount of cultivation medium and transferred to the surface of material sample with the density of 3 500 cells/cm<sup>2</sup> of a cultivation vessel. After exposition period (8 or 72 hours) samples were washed by PBS twice and cells were fixated and dried by increasing alcohol series. Dried cell-seeded samples were examined by SEM. Tolerance of cells towards the tested material was evaluated by calculating the percentage of surface colonization [113].

Besides cytotoxicity, **bioactivity** of test pieces immersed in the culture medium was evaluated. Minimum essential Medium (MEM) is a cell culture medium with ionic concentration similar to SBF. Additionally, it contains the same vitamins, amino acids and glucose as blood plasma. The principle of bone-like apatite formation on surfaces of tested pieces is analogous to that of SBF solution and can be found elsewhere [114-116]. Samples were soaked in a medium for 3 days. The presence of the apatite layer on the surface was studied by SEM.

### ***Cell seeding and cultivation***

Materials were sterilized by UV-irradiation for 20 minutes in flowbox. Samples were wet in DMEM-Glutamax (Life Technologies, Czech Republic), medium for 1 hour and centrifuged on 800×g to eliminate air bubbles from material.

Adipose-derived stem cells were isolated from adipose tissue by centrifugation and collagenase extraction, as described in [117]. Briefly, adipose tissue was digested with 0.1% collagenase type IV for 30 min at 37 °C. Following enzyme activity neutralization by DMEM-F12 with 10% FBS, cells were separated by centrifugation at 600g. The pellet was resuspended in cultivation medium (10% FBS, 0.5% penicillin/streptomycin (GE Healthcare Life Sciences, USA) in DMEM Glutamax) and propagated on a culture dish coated by 0.01% gelatin.

Subsequently, cells were trypsinized and seeded on materials at concentration of 50.000/100 µl for analysis cell viability and 1 million cells/100 µl for evaluation of cell morphology. After 24 hours, samples were taken for analysis after 24 hours of cultivation.

### ***Analysis of cell viability***

Cell viability was assessed on both materials with porosity 75 ppi by fluorescent live/dead assay. Fluorescent stock solution was prepared by dilution of 0.03% w/v

acridine orange and 0.1% w/v of ethidium bromide (Sigma-Aldrich, Czech Republic) into 2% EtOH in distilled H<sub>2</sub>O, with final dilution 1/1000 in 0.1 M phosphate buffer. Fluorescent solution was added to the samples for 5 minutes at room temperature and live/dead cells were visualized using epifluorescence microscope Cell<sup>^</sup>R (Olympus C&S Ltd., Prague, Czech Republic).

#### ***Evaluation of cell morphology by fluorescence microscopy***

Cells cultivated for 24 hours on all materials were fixed with 4% paraformaldehyde dissolved in 0.1 M phosphate buffer and permeabilized by 0.1% Triton TX-100. Actin cytoskeleton was stained with 60 nM Phalloidin Rhodamine (R415, Lifetech, Czech Republic) dissolved in 0.1 M PBS and cell nuclei were stained with 1 µg/mL 4',6-diamidino-2-phenylindole (DAPI), (Sigma-Aldrich, Czech Republic). Samples were observed with epifluorescence microscope Cell<sup>^</sup>R (Olympus C&S Ltd., Prague, Czech Republic).

### **4.3 Ceramic foam processing**

Ceramic scaffolds were prepared by two techniques: by polymer replica technique and by burning out of polyurethane from CaP / PU composites prepared in situ from MDI and polyol.

#### **4.3.1 Polymer replica technique**

This procedure was chosen as optimal because of its versatility and the possibility to fabricate ceramic foams with open porosity which is one of the fundamental parameters in tissue engineering. The formed structure has been closely similar to the structure of trabecular bone.

The key to obtain highly reproducible uniformly covered foams without sealed pores was to handle the multistep processing technique which is illustrated in Fig. 24. In general, polymer sponge templates were cut into desired shapes (blocks or cylinders) and subsequently immersed into the ceramic suspension (the individual compositions are listed in subchapters below this section). The suspension residue was removed by squeezing between two extra polymer foams and by application of compressed air.

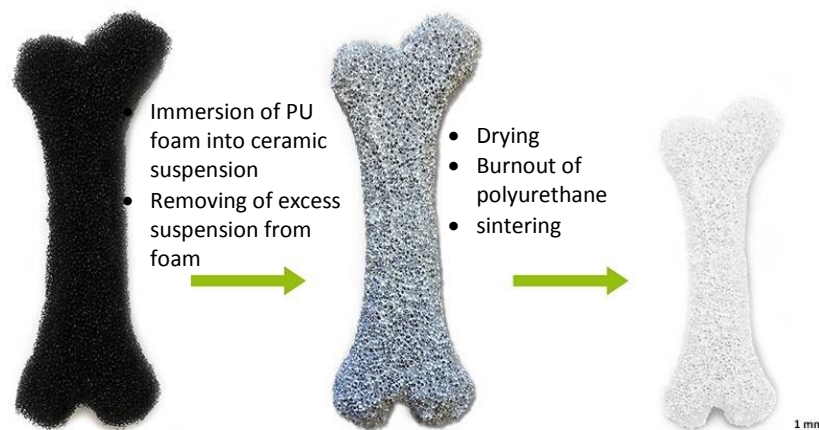


**Fig. 24** A scheme of preparation of ceramic scaffold by replication technique: (a) PU template, (b) template coated by suspension, (c) sintered ceramic body

To achieve lower final porosity, it was possible to repeat this step until desired thickness of struts. So-prepared templates were dried at ambient atmosphere for 24 h. Then the polyurethane sponge was burnt out at 800 °C or 1000 °C for 2 h with slow heating rate (0.5–1 °C/min) to preserve crack formation in a green foam structure. Calcined foams were pressureless sintered in air in a superkanthal furnace with increasing rate 5 °C/min. Some of sintered cores were consequently impregnated by another suspensions with aim to fill the hollow struts and thus to enhance mechanical properties. Reinforced scaffolds were dried and sintered. The last step in case of bioinert ceramic foams was dipping in the calcium phosphate based suspension, drying and sintering.

As was mentioned above, scaffolds of different composition were prepared by this technique. Chemical composition of suspensions, heat treatment and other parameters are described in more detail below.

### ***Alumina based scaffolds***

- PU template: Bulpren S 28190 with initial pore size 30 ppi, 30 × 30 × 30 mm,  $\phi$  28 × 30 mm
- Suspension preparation:

Compositions of studied suspensions are summarized in Table 9.

**Table 9** Composition of suspensions used for alumina scaffolds (“A” in sample identification refers to core suspension, “D” and “R” refers to shell layers)

Suspension	Disperal (g)	H <sub>2</sub> O (g)	Powder (g)
A700	1.92	28.08	70.0 (F1200)
A710	1.86	27.14	71.0 (F1200)
A720	1.79	26.21	72.0 (F1200)
A725	1.76	25.74	72.5 (F1200)
A730	1.73	25.27	73.0 (F1200)
A740	1.66	24.34	74.0 (F1200)
D8	8.0	92.0	×
R35	4.16	60.84	35.0 (RCHP-DBM)
R50	3.20	46.80	50.0 (RCHP-DBM)
Suspension	Butvar (g)	Isopropanol (g)	Powder (g)
HA	0.086	5.61	4.3 (hydroxyapatite)

Alumina core: Disperal was stirred with water at 240 rpm for two hours; the subsequent aging took 2, 4, 6, 8, 24, and 430 h. Alumina powder was added into the aged colloidal solution.

Hydroxyapatite shell: Butvar was left to swell in isopropanol for 1 hour. The resulting solution mixed with hydroxyapatite powder was ball-milled for two hours in polyamide container with zirconia balls to form the suspension.

- Scaffold processing

Alumina cores prepared as described in chapter 4.3.1. were reinforced by two ways: (1) by infiltration of colloidal dispersion of Disperal (“D10”) for 8, 24, 64,

128 h and 5 × 5 h (2) by infiltration of alumina suspension “R35” or “R50”. Scaffolds were soaked under reduced pressure to facilitate penetration into the pores.

- Heat treatment:

Alumina core: PU foam was burnt out at 800 °C for 2 h in air atmosphere. Final sintering was carried at 1400, 1500 and 1600 °C for 2 or 4 h in air.

Disperal / alumina reinforced scaffold: 800 °C/2 h and 1600 °C/2 in air.

Hydroxyapatite shell on alumina: 800 °C/2 h and 1250 °C/2h in air atmosphere.

### **Alumina toughened zirconia based scaffolds**

- PU template: Bulpren S28133 (45 ppi), S 28089 (60 ppi), S 31062 (75 ppi)

- Suspension preparation:

Compositions of studied suspensions are summarized in Table 10

**Table 10** Composition of suspensions used for ATZ scaffolds

Suspension	Disperal (g)	HWY 5.5SD (g)	Water (g)
ATZ_97.5_0.5	1.78	48.22	50.00
ATZ_97.5_0.55	1.96	53.04	45.00
ATZ_97.5_0.6	2.14	57.86	40.00
ATZ_95_0.5	3.52	46.48	50.00
ATZ_95_0.55	3.87	51.13	45.00
ATZ_95_0.6	4.23	55.77	40.00
ATZ_95_0.65	4.58	60.42	35.00
ATZ_90_0.5	6.90	43.10	50.00
ATZ_90_0.55	7.59	47.41	45.00
ATZ_90_0.6	8.28	51.72	40.00
Suspension	Butvar (g)	Isopropanol (g)	Powder (g)
HA_pvb	0.09	5.63	4.28
β-TCP_pvb	0.11	4.68	5.21

Processing of ATZ suspension: zirconia powder (HWY 5.5SD) was bonded by 24hours-aged boehmite sol stabilized by 1 M acetic acid to pH4. The suspension was stirred for 1 hour by overhead stirrer. US was applied for the last 30 min of stirring to crush agglomerates.

CaP suspensions: Butvar was left to swell in isopropanol for 1 h, the powders were added and suspensions were stirred for 2 h by magnetic stirrer at 240 rpm.

- Scaffold processing

ATZ cores were prepared as described in chapter 4.3.1. To achieve different porosities, various number of layers was applied. Each layer was dried at 60 °C until the constant weight. The coating and drying procedure was repeated until the desired number of layers was reached (up to 6).

Sintered ATZ foams were soaked in the CaP suspension at reduced pressure and the excess slurry was removed by compressed air. This step was repeated twice to achieve a homogenous layer.

- Heat treatment:

ATZ core: PU foam and other organic residues were burned out at 800 °C for 2 h in air (temperature increase 1 °C/min). Sintering was carried out at 1550 °C for 2 h in air.

Composites were burned at 800 °C/2 h and sintered at 1200 °C/3h in air atmosphere.

### ***Calcium phosphate based scaffolds***

- PU template: Bulpren S 28133, S 28089, S 31062, S 31048 with initial pore sizes 45, 60, 75 and 90 ppi. Dimensions:  $\phi$  18 × 10 mm;  $\phi$  9.2 × 10 mm, 5 × 2 mm

- Suspension preparation:

CaP powders were bonded by water solution of polyvinylalcohol. Powder was added into solution of polymer binder. The resulting suspension was agitated by 3D motion generated by Turbula device (Willy A. Bachofen AG – Maschinenfabrik, Switzerland) at 98 rpm for 2 h.

Preparation of water suspension: 5 wt. % PVA (Mow 4-88, 10-98, 20-98), 0.01 – 0.1 wt% octanol, 0.2–0.5 wt. % glycerol. PVA was allowed to swell in water before the addition of octanol and glycerol. The solution was then filled by commercial HA or calcined HA powder to achieve weight ratio of 40 to 50 wt. %.

- Scaffold processing

CaP scaffolds were prepared as described in chapter 4.3.1. To achieve different porosities, various dilution of starting concentration was used or various number of layers was applied. Scaffolds were dried at air atmosphere for 24 h.

- Heat treatment:

PU template was burnt out at 1000 °C for 2 h with heating rate 0.5 °C/min, scaffold was finally sintered at 1100 °C/2 h, 1150 °C/2 h, 1200 °C/3h, 1250 °C/3h and 1400 °C/3h in air.

### ***Calcium Phosphate based scaffolds reinforced by silica***

- PU template: Bulpren S 28133, S 28089 S 31062, S 31048 with initial pore sizes 45, 60, 75 and 90 ppi,  $\phi$  9.2 × 10 mm for mechanical and  $\phi$  5 × 2 mm for biological tests.

- Suspension preparation:

HA powder was bonded by colloidal silica solution Ludox. Various HA/SiO<sub>2</sub>/water ratios were tested. Starting compositions are summarized in Table 11. The suspensions were subsequently water diluted according to the pore size of the template.



**Table 11** Compositions of HA/SiO<sub>2</sub> suspensions

	HA powder (g)	Ludox SK-R (g)	Water (g)
HA 95 SiO <sub>2</sub> 5	10	1.97	8.03
HA 90 SiO <sub>2</sub> 10	10	4.17	5.83
HA 85 SiO <sub>2</sub> 15	10	6.62	3.38
HA 80 SiO <sub>2</sub> 20	10	9.37	1.00

Powder was added into the water and Ludox mixture. The resulting suspension was agitated by 3D motion generated by Turbula device (Willy A. Bachofen AG – Maschinenfabrik, Switzerland) at 98 rpm for 2 h.

- Scaffold processing

HA/SiO<sub>2</sub> scaffolds were prepared as described in chapter 4.3.1. To achieve different porosities, various dilution of starting concentration was used. Scaffolds were dried at ambient atmosphere for 24 h.

- Heat treatment:

PU template was burnt out at 1000 °C for 2 h with heating rate 0.5 °C/min, scaffold was finally sintered at 1200 and 1250 °C/3h in air.

### 4.3.2 CaP scaffold prepared from rigid polyurethane foam

Ceramic foams described in this chapter were again obtain by burning out of the organic content from polyurethane / CaP composite. The difference compared to previous chapters was that the composite foam was polymerized in situ. The main advantage of this approach was supposed to be an increase of the strength due to fully filled ceramic struts.

#### ***Preparation of the composite foams***

Porous polyurethane / CaP composite scaffolds were produced by the reaction between the polyisocyanate ONGRONAT 2500 and the polyol STEPANPOL PS-2412. The detailed compositions of the prepared mixtures can be found in Table 12, where the sample name is created as follows: *type of powder, powder/polyurethane ratio in %\_H<sub>2</sub>O in pphp (parts per hundred polyol)\_isocyanate index*.

The required quantities of the polyol, deionized water and powder were rigorously mixed in a mortar for 5 min. The isocyanate was then added into the same mortar and mixed until achieving a homogenous texture (maximally for another 1 min). If the powder/polyol ratio was higher than 2.3 (resp. 2 for uncalcined powder) the excess powder was added into the diisocyanate before the final mixing. The resulting mixture was immediately put into a mould and left there for 24 hours to allow the formation and growth of the composite foam.

**Table 12** Compositions of studied composite foams

Sample	polyol (g)	water (mg)	MDI (g)	CaP powder (g)
HA100_0_105	3.09	0	1.91	5 (HA calcined)
HA100_1_105	2.79	28	2.18	5 (HA calcined)
HA100_2_105	2.55	51	2.40	5 (HA calcined)

HA100_3_105	2.35	70	2.58	5 (HA calcined)
HA100_4_105	2.17	87	2.74	5 (HA calcined)
HA100_5_105	2.02	101	2.88	5 (HA calcined)
HAu100_0_105	3.09	0	1.91	5 (HA uncalcined)
HAu100_2_105	2.55	51	2.40	5 (HA uncalcined)
HAu100_4_105	2.17	87	2.74	5 (HA uncalcined)
HA62_0_105	3.09	0	1.91	3.09 (HA calcined)
HA56_1_105	2.79	28	2.18	2.79 (HA calcined)
HA51_2_105	2.55	51	2.40	2.55 (HA calcined)
HA47_3_105	2.35	70	2.58	2.35 (HA calcined)
HA43_4_105	2.17	87	2.74	2.17 (HA calcined)
HA40_5_105	2.02	101	2.88	2.02 (HA calcined)
HA100_2_75	2.96	59	1.98	5 (HA calcined)
HA100_2_85	2.81	56	2.14	5 (HA calcined)
HA100_2_95	2.67	53	2.27	5 (HA calcined)
HA100_2_115	2.44	49	2.51	5 (HA calcined)
HA100_2_125	2.34	47	2.62	5 (HA calcined)
HA40_2_105	2.55	51	2.40	2 (HA calcined)
HA60_2_105	2.55	51	2.40	3 (HA calcined)
HA80_2_105	2.55	51	2.40	4 (HA calcined)
HA120_2_105	2.55	51	2.40	6 (HA calcined)
HA40_4_105	2.17	87	2.74	2 (HA calcined)
HA60_4_105	2.17	87	2.74	3 (HA calcined)
HA80_4_105	2.17	87	2.74	4 (HA calcined)
HAu61_0_107	6.11	0	3.89	6.13 (HA uncalcined)
TCP74_0.5_95	9.16	45	5.80	11.12 (TCP)
HAu61_0.5_108	6.08	30	3.89	6.11 (HA uncalcined)

After the curing, the green body was removed from the mould and cut into the required shapes. The organic contents were burnt out in air at 800 °C for 2 hours (or 1050 °C/2 h) with a slow heating rate 0.5 °C/min. The ceramic scaffolds were finally sintered at 1050 °C/2 h, 1200 °C/2 h and 1350 °C/2 h in air atmosphere with a heating and cooling rate 5 °C/min.

## 5 RESULTS AND DISCUSSION

### 5.1 Bioactive ceramics based on alumina core

#### 5.1.1 Characterization of suspensions

The rheological behaviour of sols and suspensions was studied in order to find suspension with optimal adhesion to PU template, optimum stability and high cover efficiency. As shown in Fig. 25 the viscosity of 6 wt. % sol of Disperal was influenced by time of aging. When the aging time increased, the viscosity decreased. The shear thinning behaviour occurred in lower shear stresses in the case of shorter aging time (2 and 4 h). The Newtonian behaviour was observed after 6 h of aging. Nevertheless, the optimal aging time was determined to 24 h, when the supposed de-agglomeration of powder was finished and sol was stabilised with almost Newtonian rheological behaviour.

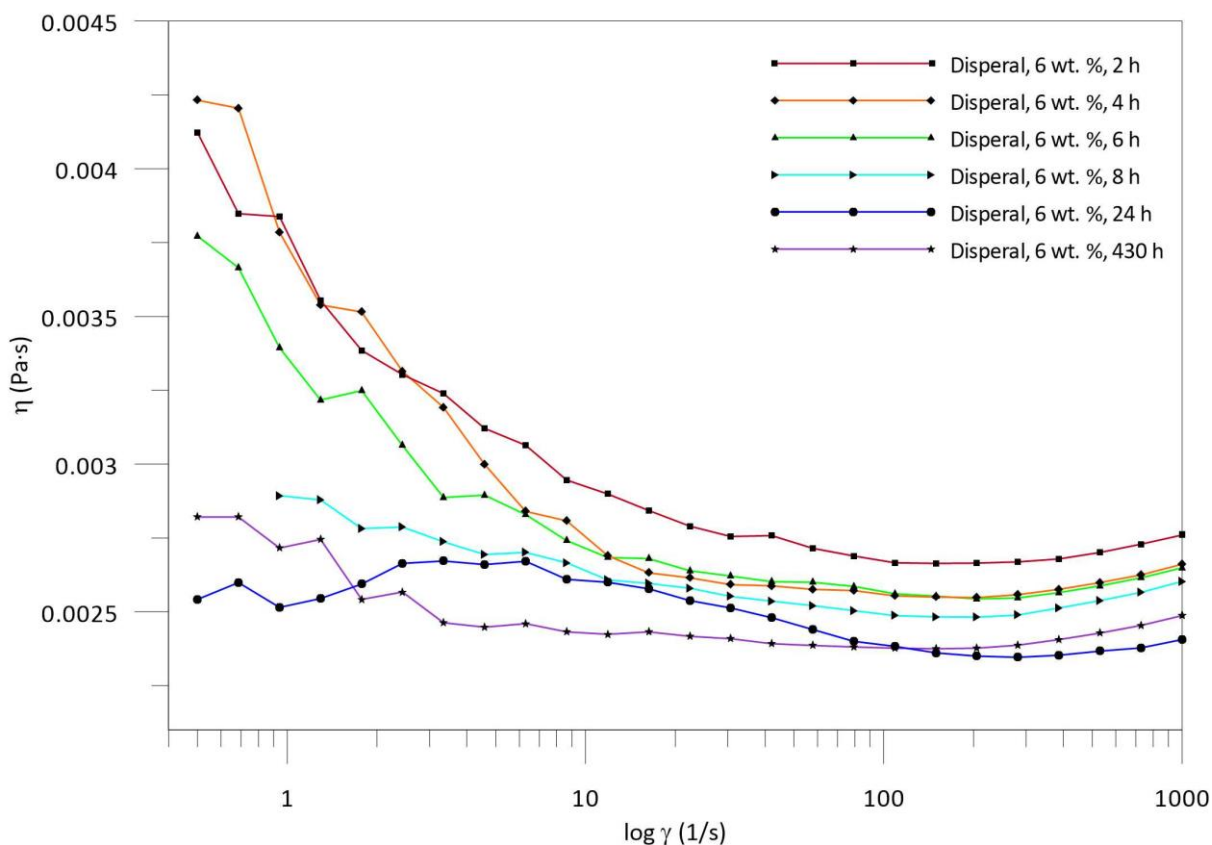


**Fig. 25** Rheological behaviour of 6 wt. % dispersal sol

In order to optimize replica method, 24 h aged Disperal sol was filled with different amount of alumina. Fused and milled alumina powder was chosen for core layer to prevent unfavourable shrinkage during sintering. As shown in Fig. 26, the suspensions with various alumina content (from 71 to 73 wt. %) exhibited shear-thinning behaviour; viscosity increased with increasing alumina content. A thixotropic behaviour of all alumina suspensions was observed in lower shear stresses. Shear thinning behaviour was in accordance with previously published works [99, 118]. Coating behaviour was further important parameter for

determination of optimal composition of suspension. Suspension with 72.5 wt. % of alumina revealed an optimal adhesion to PU foam with low degree of sealed struts of foam.

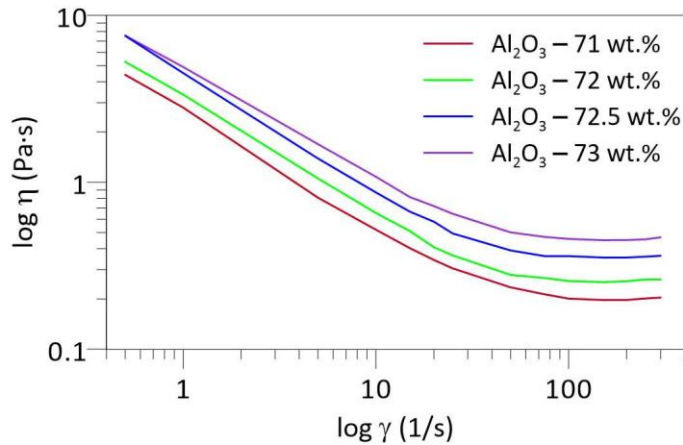


**Fig. 26** Concentration dependence vs. rheological behaviour of fused alumina suspensions

### 5.1.2 Foam characterisation

The macrostructure morphology of prepared foams, after taking into account the shrinkage, was almost the same as one of PU template that was replicated. As is evident from Fig. 27 prepared foams were highly porous without sealed walls of scaffold cells (pores). The average scaffold cell size was  $3539 \pm 218 \mu\text{m}$ . The average size of pores that connected cells, sometimes referred as “cell windows” was about  $1200 \mu\text{m}$ . Detail dimensions for various compositions are summarized in Table 13. Thickness of hollow struts varies between 260 and  $370 \mu\text{m}$ . The triangular void in the centre of strut (see Fig. 29a) is a main drawback of replica method, because it negatively influences the mechanical properties of foam [89].

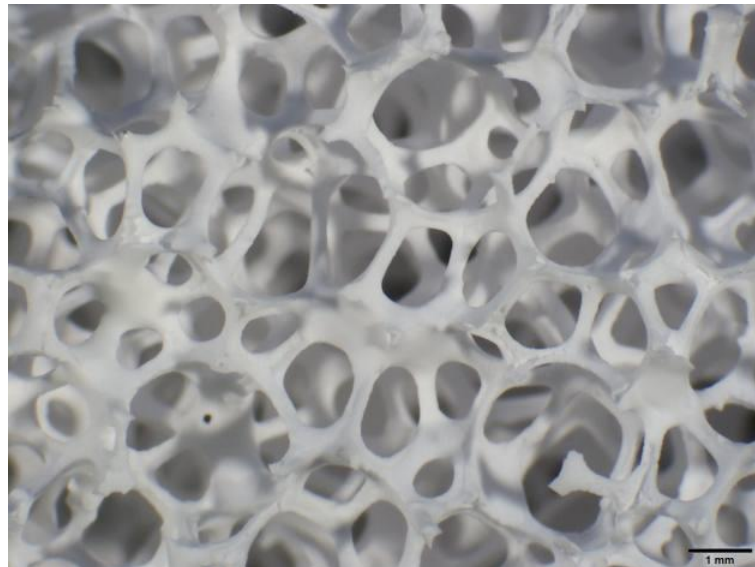


**Fig. 27** Macrostructure of alumina foam (A7250)

Two methods of filling of the struts were tested: (1) soaking in 8 wt. % Dispersal sol for different time periods and (2) coating by shell layer composed of Dispersal sol and chemically synthesized alumina powder with smaller particles than the fused and milled alumina particles. Particle size distribution of used powders is given in Fig. 28. Combination of three

different alumina powders with particle size varied from nano to micro had a crucial influence on final properties of foams such as density, porosity and mechanical properties [119].

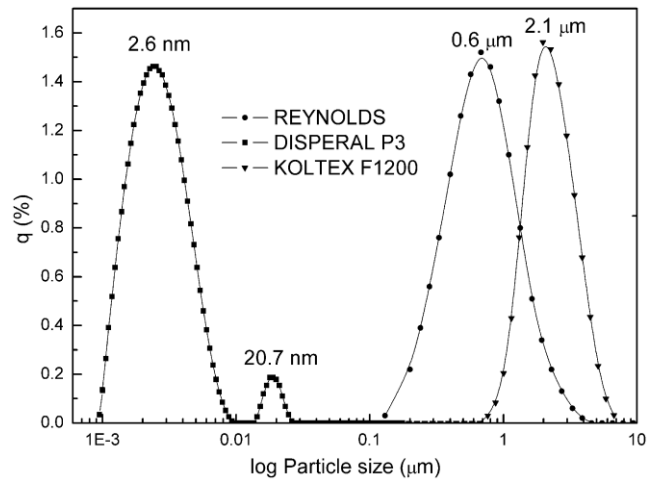


**Fig. 28** Particle size distribution of alumina powders

Pore size, porosity and density of alumina foams before and after infiltration of Dispersal sol are summarized in Table 13. The density of strut material slightly increased with increasing alumina content. However, this trend was not confirmed by image analysis, where, taking into account standard deviation, the porosities were almost the same. Results indicate that long soaking time had a positive influence on density of strut material.

**Table 13** Summary of obtained porosities and densitis of foam composites

sample	Wt. %	Time of infiltr. (h)	Total porosity (%)	Pore size („cell window“) (μm)			Porosity of strut mat. (%)	Archimedes density (% $\rho_{theor.}$ )
				min	max	mean		
A7100	71	0	95.1	314	2350	1134	46.03	51.97 ± 0.63
A7107	71	168	93.1	234	2603	1168	39.64	—
A710X	71	5x5	93.2	290	2401	1265	43.22	—
A7200	72	0	95.3	190	2127	1021	48.21	53.22 ± 0.14
A7207	72	168	93.4	276	2687	1112	33.84	—
A720X	72	5x5	92.3	234	2537	1105	37.99	—
A7250	72.5	0	95.5	262	2453	1199	46.97	53.15 ± 0.31
A7257	72.5	168	94.9	205	2329	1108	29.95	—
A725X	72.5	5x5	93.4	294	2635	1361	43.88	—
A7300	73	0	93.3	208	2370	1158	49.28	54.44 ± 0.64
A7307	73	168	92.9	414	2952	1431	31.66	—
A730X	73	5x5	91.7	280	3088	1498	47.89	—

Influence of infiltration of Dispersal sol on struts morphology is illustrated in Fig. 29. The figure on the left illustrates the cross-section of foam based on fused alumina, the middle cross-section was obtain after 168 h infiltration and on the right side, there is the cross section of foam which was soaked 5 times for 5 hours. It is evident that the hollow voids inside the struts were not completely filled with nanosized alumina, nevertheless, the repeating drying after 5 hours cycles had positive effect on the strut morphology. It was the interesting result because density evaluated by means of image analysis showed that density increased more significantly in the case of very long soaking time – after 168 h as is illustrated in Fig. 30. Small

alumina particles are visible inside the pores but is evident that neither pores were filled completely.

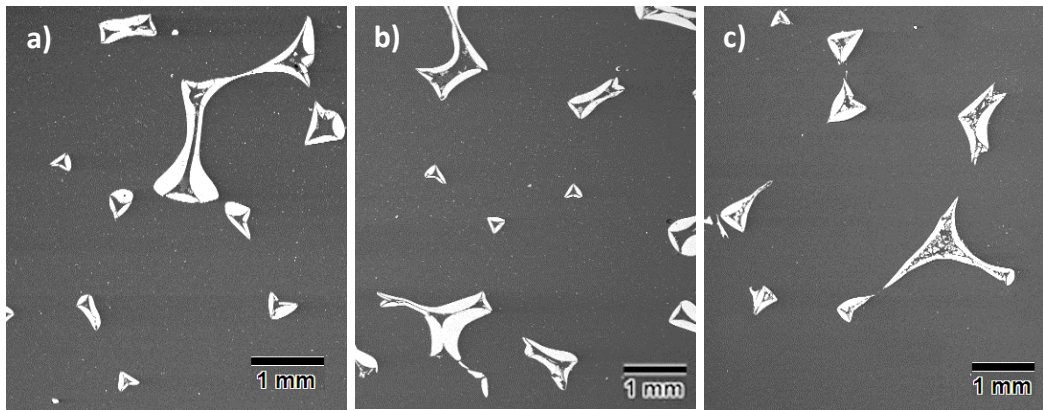


**Fig. 29** Cross-section of alumina core (a) before soaking in Disperal sol and (b) after soaking in Disperal sol 168 h and (c) after 5x soaking in Disperal sol for 5 hours – newly formed small alumina particles are visible in pores

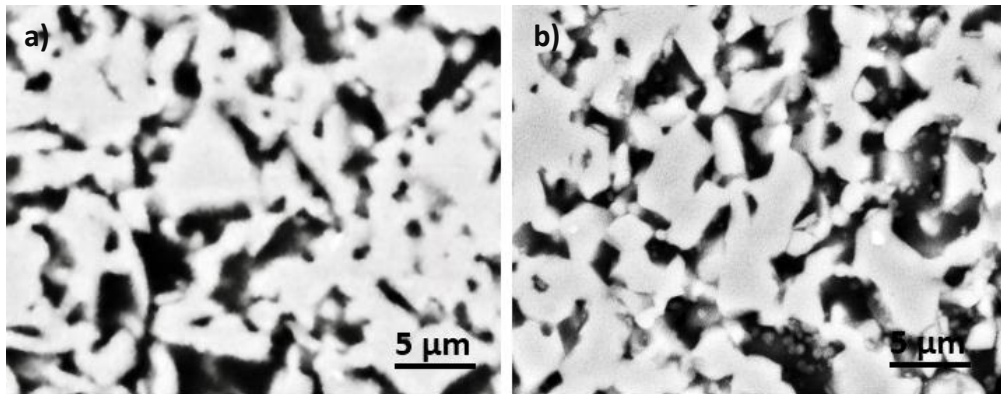


**Fig. 30** Microstructure of alumina strut A725 (a) before soaking in Disperal sol; (b) after soaking in Disperal sol – newly formed small rounded alumina particles are visible in pores

On the contrary, the strut was completely filled by second approach, by coating by microsized synthesized alumina (Fig. 31). To improve the bioactive behaviour, the bioactive calcium phosphate surface layer was applied on cores reinforced by this approach—by synthesized alumina, as can be seen in Fig. 32. As is evident, the layers are strongly bound to each other. The thickness of each layer (synthesized alumina and hydroxyapatite) was about 20 μm.

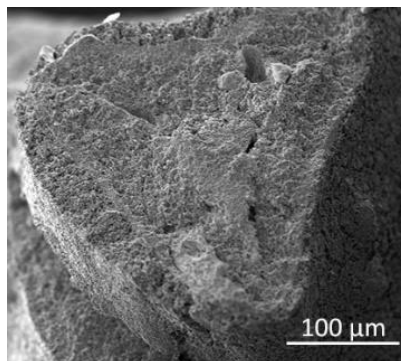


**Fig. 31** Detail of core strut filled by synthetic alumina

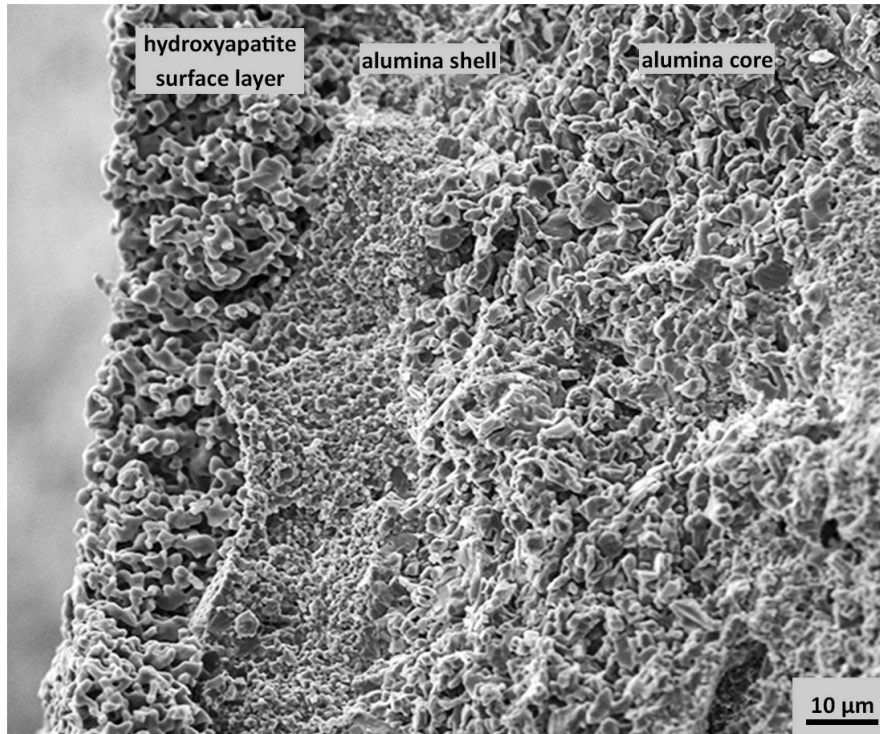


**Fig. 32** Microstructure of composite (from right to left: alumina core, alumina shell and hydroxyapatite layer)

### 5.1.3 Biological properties – bioactivity testing in simulated body fluid

Biological properties were evaluated by means of bioactivity testing in simulated body fluid. After 14 days of soaking in SBF, the surface of the scaffold was partially covered by newly formed apatite layer in typical cauliflower morphology consisted of thin lamellae as is illustrated in Fig. 33. The formation of bone-like apatite on the surface of alumina / alumina / hydroxyapatite scaffold after soaking in SBF was attributed to the ion exchange between HA compacts and the SBF solution.

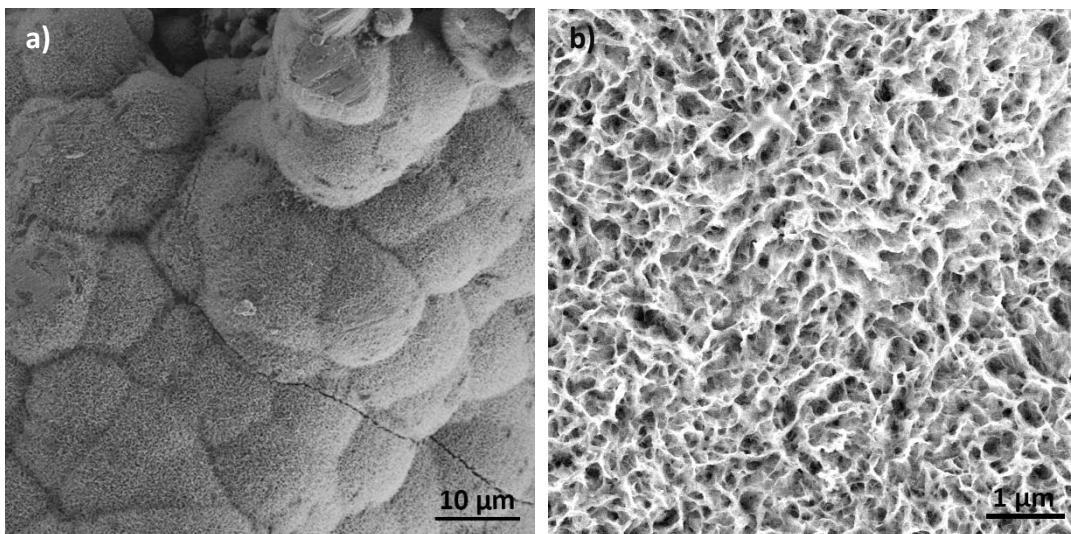


**Fig. 33** Surface of alumina / alumina / hydroxyapatite scaffold after 14 days immersion in SBF: (a) typical cauliflower like structure of newly formed apatite; (b) detail of thin lamellae.

### 5.1.4 Mechanical properties

Resistance of prepared foams to the mechanical loading were characterised by compressive strength. The overview of the compressive strength values on the used preparation parameters is plotted in Fig. 34.

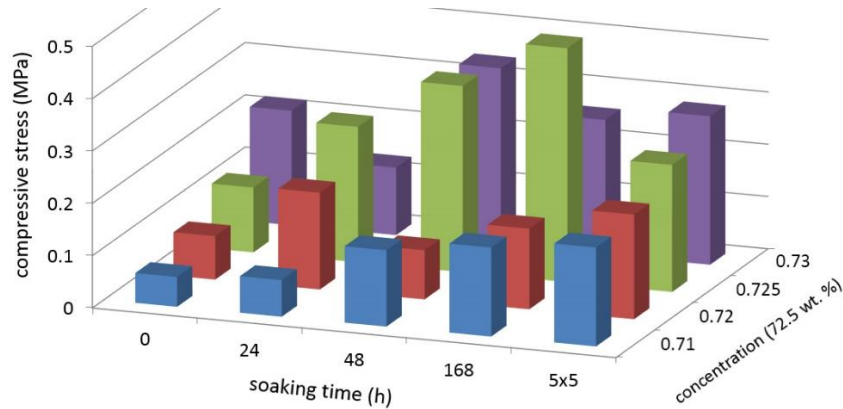


**Fig. 34** Compressive strength of alumina foams reinforced by boehmite sol in dependence of various soaking times.

From this dependence a change of mechanical resistance with both the soaking time and the concentration of suspension used for the infiltration is visible. The short soaking time and/or suspensions with low powder content exhibited low compressive strength due to non-homogenous and insufficient infiltration of the core layer. On the other hand, suspensions having higher powder content exhibited enhancement of compressive strength. Therefore, the optimal processing conditions were chosen for the powder content of 72.5 wt. % and the soaking time 168 h or 5 × 5 h.

Nevertheless, the compressive strength values seemed to be quite low. It was caused by very high porosity of testing samples which exceeded 92 %. The strength is exponentially proportional to the porosity, hence 5% reduction of porosity by coating of shell layer had positive effect on mechanical stability of the prepared foams. The compressive strength of core-shell type specimens are displayed in Fig. 35. The maximum strength increased to 1.2 MPa.

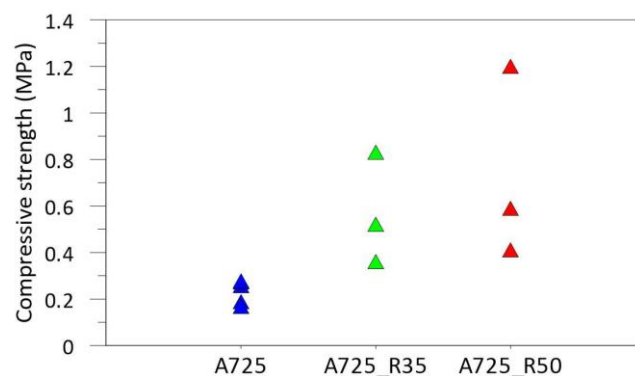


**Fig. 35** Compressive strength core-shell alumina composites. A725 – alumina core; A725\_R35 – alumina core / alumina shell (35 wt. %); A725\_R50 – alumina core / alumina shell (50 wt. %);

Basically two fracture mechanisms were observed. The first one exhibited separate fracture of individual struts in the area of contact between sample and compressive platens.



This fracture behaviour was observed in samples with lower compressive strength and typical example of loading curve is displayed in Fig. 36a and corresponding images before and after the test are below the loading curve in the same figure. The different fracture mechanism was observed during loading of samples having higher compressive strength where the damage occurred in the whole specimen volume. Usually the final fracture was comparable with typical fracture behaviour of bulk and loading trace exhibits sudden drop of load. The example of loading trace is displayed in Fig. 36b and corresponding images before and after the tests can be found below the curve.

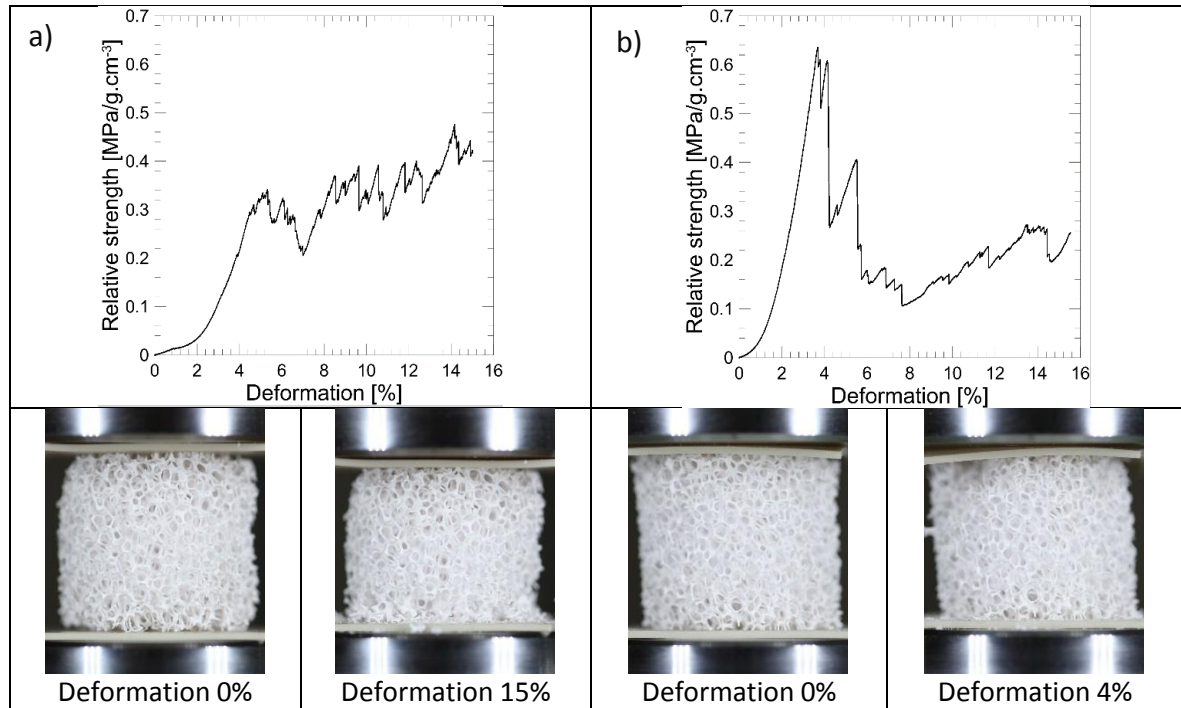


**Fig. 36** Fracture behaviour under applied stress: (a) separate fracture of individual struts; (b) fracture in the whole specimen volume

### 5.1.5 Summary of Chapter 5.1

Open-cell alumina foams were prepared by replica technique from fused alumina powder bonded by boehmite sol. Porous cores exhibited low compressive strength (<0.3 MPa) due to high total porosity (93–96%), low microstructure density (~ 50%) and because of triangular voids inside the strut which could act as stress concentrators. The strength of ceramic cores was doubled as a consequence of soaking in boehmite sol. The density of strut material after soaking was slightly higher than before, even though the struts remained partially unfilled. The second approach, soaking in suspension composed of boehmite and synthesized alumina powder, lead to completely filled struts. The compressive strength increased about fourfold. The reinforced alumina / alumina composite foams were coated by hydroxyapatite suspension to shift bioinert behaviour to bioactive one. All layers seemed to firmly adhere to each other. After 14-day-long incubation in SBF, the newly formed layer of apatite was precipitated on the surface of composite scaffold. For potential application in tissue engineering it would be necessary to reduce pore sizes to maximally 500  $\mu\text{m}$  and simultaneously enhances the compressive strength, e.g. by decreasing porosity below 85 %.

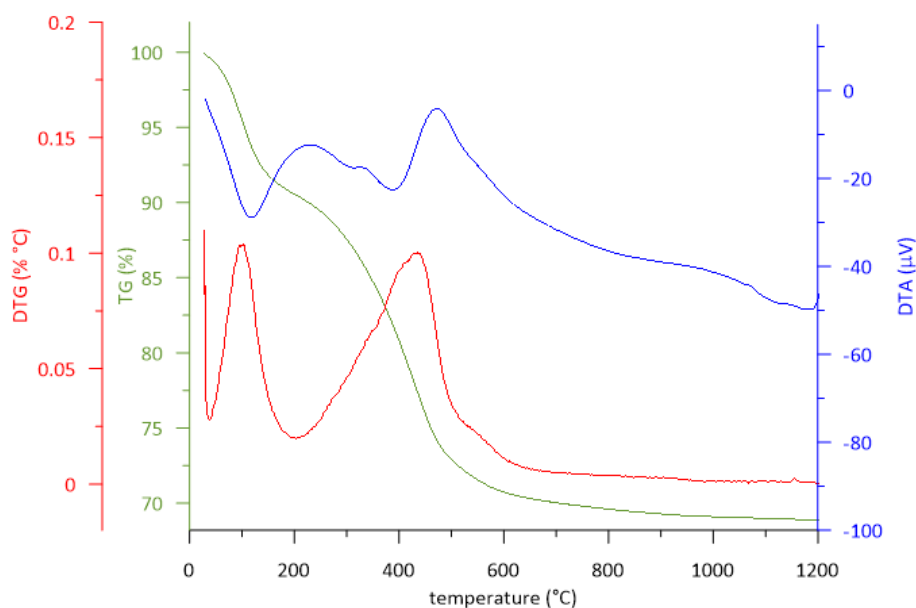
## 5.2 Bioactive ceramics based on alumina toughened zirconia

Bioactive ceramics described in this chapter were composed of zirconia inorganically bonded by boehmite (AlOOH). The amount of alumina in the structure after sintering varied between 2.5 and 10 wt. %. Alumina was not added to increase fracture toughness because zirconia powder was toughened by stabilisation of tetragonal phase by 3 mol % of yttria. The alumina was added because it was reported that it prevents zirconia from unfavourable low temperature degradation in body environment [120] and to improve properties of interface between zirconia and bioactive calcium phosphate based layer.

### 5.2.1 Characterization of suspensions and sintered scaffolds

#### *Thermal analysis*

Thermal analysis was carried out to determine the amount of Al<sub>2</sub>O<sub>3</sub> generated by decomposition of commercial boehmite powder. The TG curve (Fig. 37) indicated a total mass loss of 30.5 %. This value was slightly higher than 28% mass loss reported by the manufacturer. The higher measured loss was probably caused by physically adsorbed water. Boehmite was decomposed to alumina and water according to the following equation:

$$2\text{AlOOH} \rightarrow \text{Al}_2\text{O}_3 + \text{H}_2\text{O} \quad (6)$$


**Fig. 37** Thermal analysis of commercial boehmite sol Disperal P3

#### *Zeta potential*

Zeta potential, a key indicator of the stability of colloidal dispersions was measured in aqueous dispersion of Disperal P3. Colloids with low absolute value of zeta potential (-30 mV to +30 mV) are not efficiently electrically stabilized and tend to coagulate. As is evident from Fig. 38, the dispersions in acidic range behave stably, the highest  $\zeta$ -potential equalled to +60 mV was measured at pH 4, and therefore the pH of prepared sols was adjusted by acetic acid to this value in the following experiments.

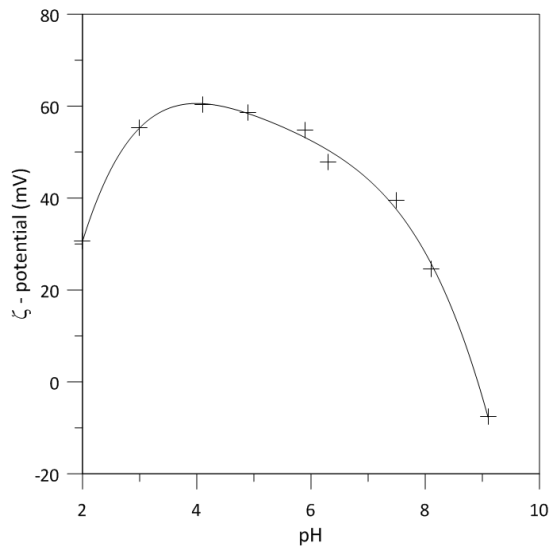


**Fig. 38** ζ-potential as a function of pH for the dispersion Disperal P3.

**Viscosity of suspensions**

Suspensions were prepared from 24 h aged boehmite sol which rheological properties were described in Chapter 5.1.1.

The viscosity dependence on the shear rate is illustrated in Fig. 39. Viscosity of suspensions increased with increasing content of solid phase almost 20 folds. The prepared suspensions moreover exhibited slightly thixotropic behaviour, therefore it was necessary to stir the suspension at a constant speed of 240 rpm during a template coating.

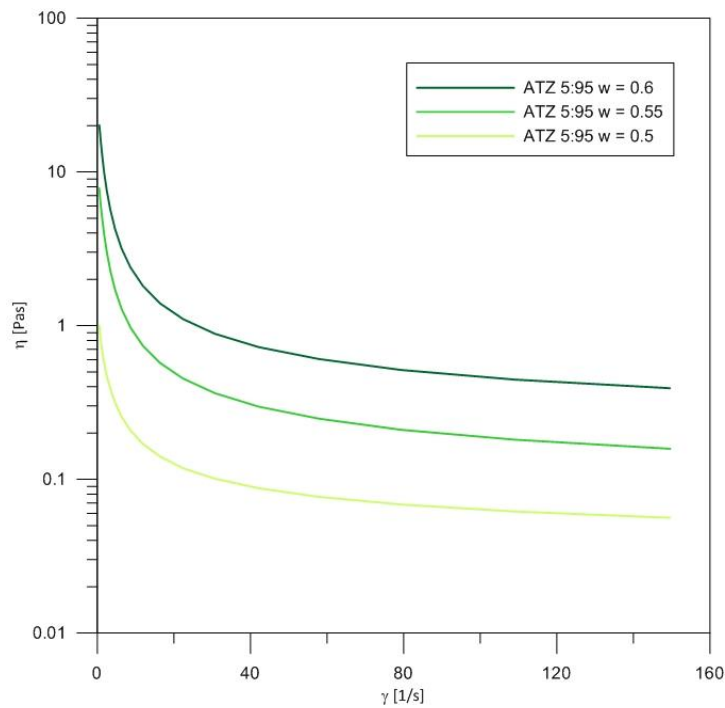


**Fig. 39** Effect of shear rate and suspension concentration on viscosity

From a technological point of view, the best results for the scaffolds with pore sizes equal to 45 ppi were achieved when suspension contained 60 wt. % of solid phase.

However, this suspension was too viscous for coating of scaffolds with smaller pores. To avoid undesirable blocking of open scaffold cells (“macropores”), the scaffolds with 60 ppi and 75 ppi porosity were coated by suspension containing 50 wt. % of solid phase.

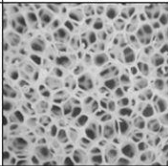
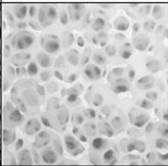
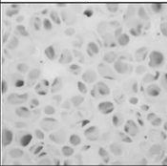
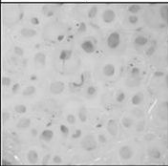
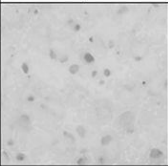
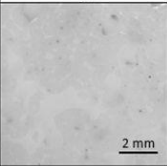
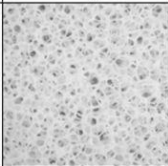
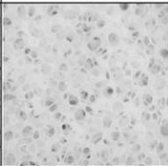
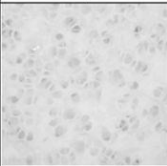
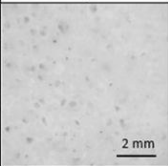
### **Morphology of sintered scaffolds**

Ceramic foams of different total porosity and pore size were prepared by coating of various templates several times. Morphology parameters of sintered scaffolds such as total porosity, strut thickness, cell size and size of windows between adjacent macrocells (pore size) of prepared scaffolds are summarized in Table 14.

**Table 14** Porosity, strut thickness, cell size and pore size of ATZ scaffolds

PU porosity	n layers	Porosity	Strut thickness ( $\mu\text{m}$ )	Scaffold cell size ( $\mu\text{m}$ )	Pore sizes ( $\mu\text{m}$ )
45 ppi	1 layer	98.3 $\pm$ 0.7	100 $\pm$ 18	1260 $\pm$ 423	496 $\pm$ 334
45 ppi	2 layers	93.3 $\pm$ 0.6	146 $\pm$ 35	1258 $\pm$ 390	476 $\pm$ 328
45 ppi	3 layers	88.7 $\pm$ 1.7	169 $\pm$ 40	1166 $\pm$ 379	442 $\pm$ 284
45 ppi	4 layers	78.6 $\pm$ 1.9	274 $\pm$ 71	990 $\pm$ 336	336 $\pm$ 243
45 ppi	5 layers	63.5 $\pm$ 1.5	395 $\pm$ 131	—	—
45 ppi	6 layers	52.1 $\pm$ 2.3	—	—	—
60 ppi	1 layer	96.8 $\pm$ 0.5	73 $\pm$ 17	745 $\pm$ 316	375 $\pm$ 226
60 ppi	2 layers	91.6 $\pm$ 0.9	98 $\pm$ 27	721 $\pm$ 244	320 $\pm$ 166
60 ppi	3 layers	80.3 $\pm$ 2.6	ca 296 $\pm$ 159	—	—
60 ppi	4 layers	61.5 $\pm$ 2.3	ca 340 $\pm$ 165	—	—

It is evident, that the initial porosity of the polymeric template had a crucial influence on the final scaffold cell size after sintering. Scaffold cell size corresponded to the cell size of polyurethane foam reduced by shrinkage. With an increasing number of layers, the average thickness of struts grew from 73  $\mu\text{m}$  to 395 nm. The typical reticulated morphology was lost as porosity decreased below 70 % (in the case of larger pores – 45 ppi) and below 80% (for 60 ppi). Overview of macrostructures of prepared scaffolds is shown in the Fig. 40.

	1 layer	2 layers	3 layers	4 layers	5 layers	6 layers
45 ppi						
Porosity:	98.5 %	94 %	88 %	72 %	61 %	51 %
	1 layer	2 layers	3 layers	4 layers		
60 ppi						
Porosity:	97 %	91 %	77 %	60 %		

**Fig. 40** Dependence of porosity on the number of layers.

Alumina toughened zirconia substrates with desirable porosity were coated by calcium phosphates in order to improve the biological properties of scaffolds. Scaffolds consisted of 2 layers of ATZ (5% Al<sub>2</sub>O<sub>3</sub>) and CaP coating are shown in Fig. 41. The thickness of bioactive layer achieved 20 to 60 μm. The struts of ATZ cores were not filled by HA due to closed porosity.

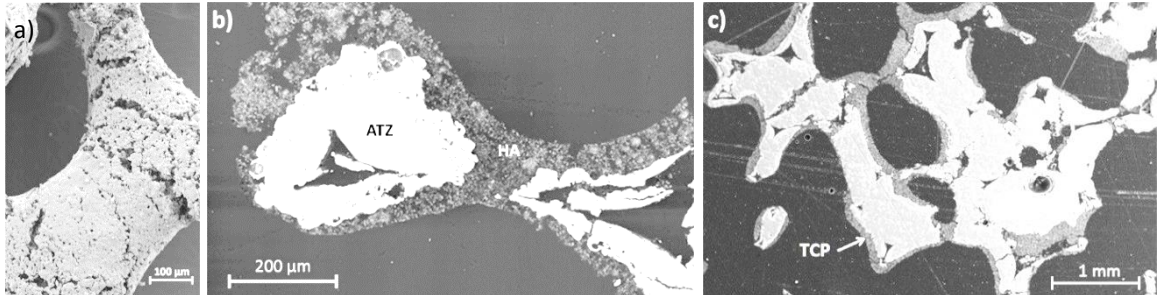


**Fig. 41** Structure of the bioactive coatings: (a) a strut with HA coating; (b) cross section of ATZ scaffold coated by HA; (c) cross section of ATZ scaffold coated by β-TCP.

### 5.2.2 Mechanical tests

Resistance of some ATZ scaffolds to the mechanical loading was characterised by compressive strength. The overview of compressive strength values of ATZ scaffolds containing 2.5 to 10 wt. % of alumina is plotted in Fig. 42. It was experimentally confirmed that strength decreases with increasing porosity. Material containing 5 % of alumina exhibited highest strength, so this composition was chosen for subsequent biological testing. All tested samples exhibited strength above 0.2 MPa, the minimal value reported for highly porous cancellous bone [121]. Scaffolds for potential load bearing applications in bone tissue engineering should have higher density than at least 2 MPa to ensure sufficient strength to withstand forces generated in the body.

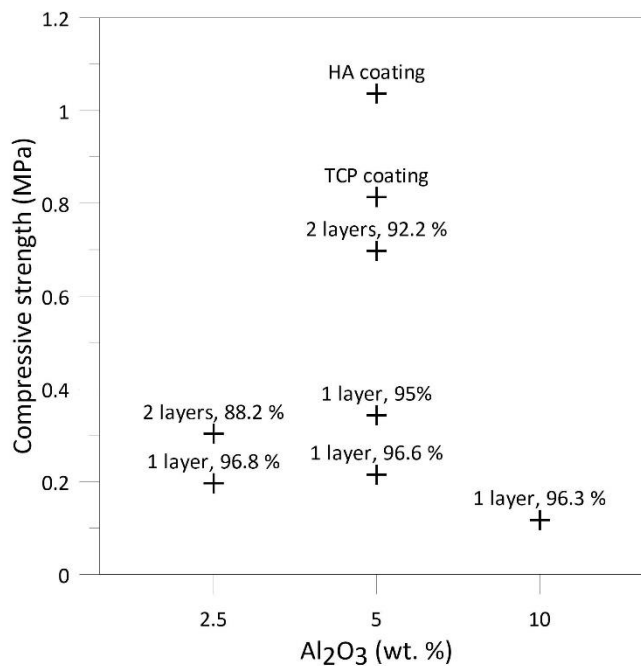


**Fig. 42** Compressive strength of ATZ scaffolds

## 5.2.3 Biological properties

### *Interaction with SBF*

The typical globular morphology of newly formed apatites were locally observable on bioactive coatings after 7 days of soaking in SBF. After 14 days, the areas containing apatite widespread. After 28 days of soaking, the surface was completely covered by a self-grown apatite layer. The top view of ATZ substrate and Ca-phosphates coatings before and after 28 days of soaking in SBF is reported in Fig. 43. No change was observed on uncoated ATZ samples.

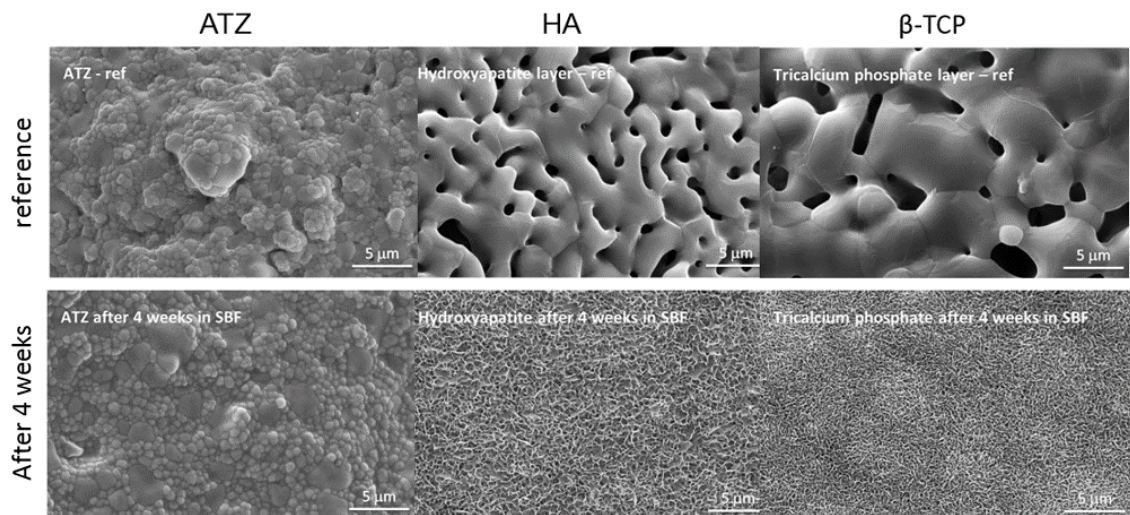


**Fig. 43** Microstructure of the substrates and coatings before and after soaking in SBF.

### *Cytotoxicity test*

Although both zirconia and alumina are considered being bioinert in contact with host tissue, the cytotoxicity of the composite was for sure evaluated by direct contact assay. Direct contact between MG-63 cells and all tested materials did not induce any adverse effect, cells retained characteristic morphology of MG-63 cells (see Fig. 44.).

SEM was used to study the adhesion and spreading of MG63 cells on the ATZ / Ca-P 3D scaffolds. Micrographs revealed that cells were attached to the pore walls both inside (Fig. 44a) and outside (Fig. 44b) of the 3D structure. These results indicate that cells were able to migrate through 3D structure of composite having the 1200 μm large pores.

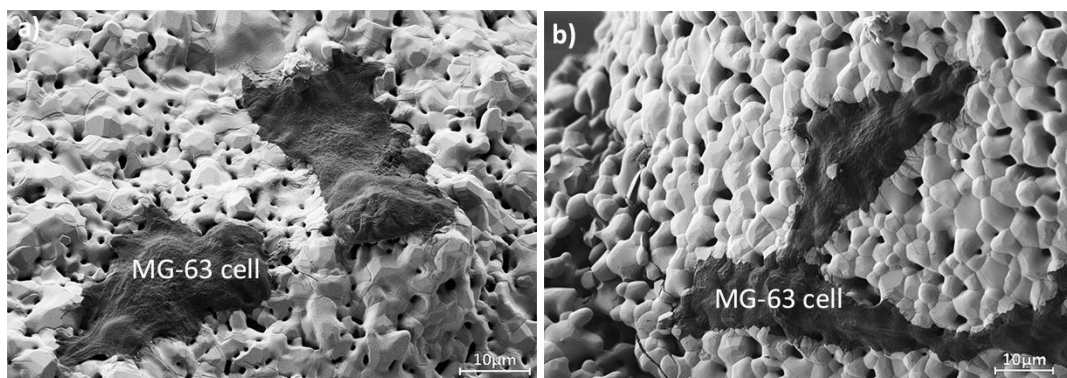


**Fig. 44** Cell line MG-63 adhered to the scaffold: (a) on inner struts; (b) on outer struts.

A large number of filopodia stretched out from the cells (Fig. 44b) indicated a good adhesion to the calcium phosphate surface [122]. The cell density and shape did not differ significantly from that observed for the negative control. The smallest amount of cells (1850 cells / cm<sup>2</sup>) adhered to the uncoated ATZ, the largest number of cells (3050 cells / cm<sup>2</sup>) was observed on the surface of  $\beta$ -TCP ceramic (see Fig. 45). This result confirmed that all tested materials (ATZ, HA,  $\beta$ -TCP) were cytocompatible and could be used in tissue engineering applications.

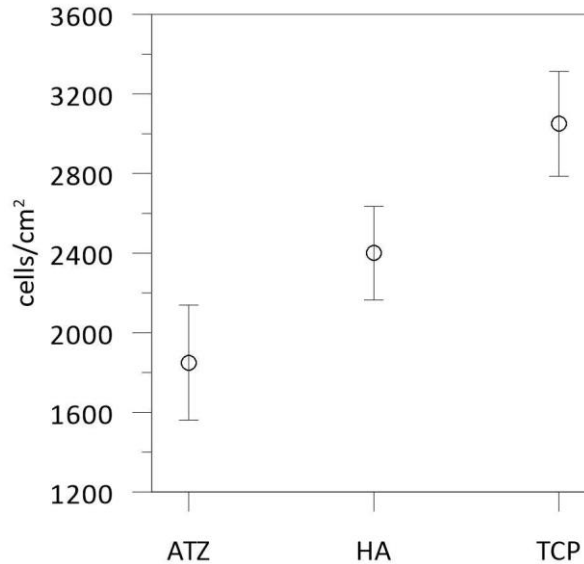


**Fig. 45** Cell density adhered on ATZ

#### 5.2.4 Summary of chapter 5.2

Alumina toughened zirconia scaffolds were prepared from 3 mol% yttria stabilised zirconia and colloidal boehmite. Pore sizes of interconnected macroporous scaffolds varied between 350 and 1200  $\mu$ m. Based on results of the mechanical testing, 5 wt. % content of alumina was chosen as optimum for further experiments. Scaffolds of various total porosity (57–98%) were fabricated by multiple coating process (up to 6 repeating). The bioactivity of the composite scaffold was improved by coating of calcium phosphate based suspension. Two powders were used – hydroxyapatite and  $\beta$ -TCP. After 28 days in SBF, newly precipitated apatite was observed on both calcium phosphates coatings. Besides bioactivity and cytotoxicity tests, the cell colonization of 3D scaffold was evaluated. It was shown, that after three days long cultivation MG-63 cells migrated through the scaffold with 1000  $\mu$ m large pores, the same amount of cells was found both adhered to the outer and inner struts of scaffold.

### 5.3 Calcium phosphate scaffolds

Several types of polymer binders were tested in order to achieve a reticulated calcium phosphate foams. However prepared scaffolds had mostly insufficient strength due to high porosity (> 90%). Scaffolds prepared from alcohol suspensions had many defects in the structure, probably as a consequence of fast evaporation of alcohol. The best scaffolds were obtained with water suspension bonded by 5 wt. % of PVA. These results are summarized and compared with silica reinforced scaffolds in the Chapter 5.4.

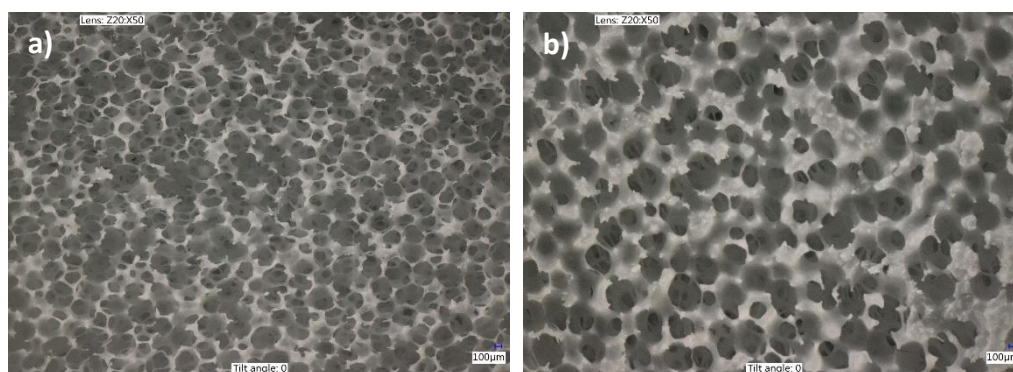


**Fig. 46** Structure of calcium phosphate scaffolds sintered at 1200 °C/3 h: (a) template 90 ppi, (b) template 75 ppi

### 5.4 Calcium phosphate scaffolds reinforced by silica

Even though the gold standard for restoring bone defects is still considered to be autologous bone grafting, there is a strong need for synthetic graft development [123-127]. Greatest similarity with bone mineral have ceramic materials based on calcium phosphates. Their wide expansion into clinical practice is, however, limited by insufficient mechanical properties. The objective of this chapter was to develop a material with higher strength and at least similar biological characteristics as hydroxyapatite. The idea was to prepare ceramic composite material containing calcium phosphate and some reinforcing phase. The choice fell on silica because silicon (as  $\text{Si}^{4+}$  ion) is considered to be one of the essential trace elements required for development of healthy bones. It acts as a biological cross-linking agent in extracellular matrix (ECM). On top of that, it enhances osteoblast proliferation, differentiation and collagen production [57]. It is claimed that silicon substituted calcium phosphate ceramics provide superior biological performance to their stoichiometric counterparts [128].

The effect of silica as a binder and reinforcing phase was studied in this part of the thesis. The morphology, mechanical and biological properties were evaluated and compared with literature and with characteristics of unreinforced Ca-P scaffolds.

#### 5.4.1 Characterisation of scaffolds – processing parameters

Since polymer replica technique was used, ceramic foams were obtained by burning the polyurethane templates. The thermal analysis was carried out to understand the decomposition process and to determine the temperature at which the complete burnout



of the commercial polyurethane occurred in the composite system containing PU (10 wt. %), HA (81 wt. %) and SiO<sub>2</sub> (9 wt. %).

TA curves of the studied foam are given in Fig. 47. The little weight loss at the beginning of the TA plot, i.e. from 40 to 200 °C was mainly due to moisture evaporation. Afterwards, the two stage thermal decomposition process of polyurethane was observed between 200 °C and 550 °C. Shape of exothermic DTA curve in the temperature range 200 to 550 °C indicates that the degradation processes of polyurethane occur by oxidation mechanism.

The typical two-stage decomposition behaviour was described in various studies [129–132]. Cakic explained the thermal degradation of PU as primarily a depolycondensation process, which started at about 200 °C [133]. At this temperature hard segments (related to urethane links) had started to decompose [134], while the second step of degradation (350–550 °C) had been caused by degradation of soft segments (related to the ether group) [134].

Experimental data suggest that the weight loss of the sample continued even above the temperature of 550 °C at which the polyurethane should have been already burned. This was likely caused by thermal degradation of hydroxyapatite which is described in detail in the chapter 5.5.1. The endothermic drop on DTA curve around 800 °C also corresponded to the thermal decomposition of HA as can be seen in thermogram which is depicted in Fig. 61.

The total 15% weight loss corresponded to the initial amount of polyurethane in the composite (10 %), amount of adsorbed water (1 %) and to 5% weight loss of commercial hydroxyapatite after its calcination (4 % relative to the composite).

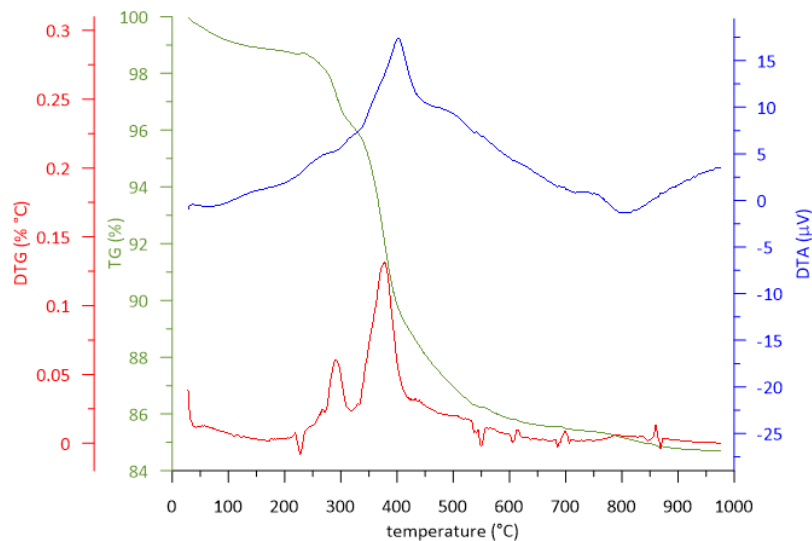
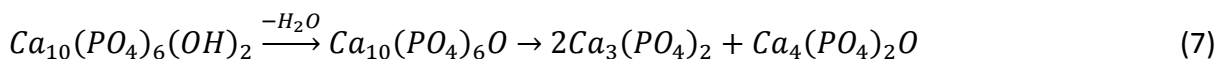


**Fig. 47** TA curves of commercial reticulated PU foam coated by HA-10SiO<sub>2</sub> suspension

## 5.4.2 Phase composition

X-ray diffraction patterns in Fig. 48 indicates that all products of thermal reaction were crystalline. The XRD spectra illustrated that the hydroxyapatite was totally decomposed into  $\alpha$  and  $\beta$ -TCP even at 1200 °C. Traces of tetracalcium phosphate identified in the structure were a result of HA decomposition, according to the following equation [135, 136]:



If the concentration of silica in the tested sample was low (5 wt. %), walstromite ( $\text{CaSiO}_3$ ), an isomorph of wollastonite, was distinguishable in the pattern. With increasing concentration of silica in the sample, one strong peak at about  $21.7^\circ$  increased. That suggests that silica was transformed to the cristobalite crystalline phase (of  $P4_12_12$  space group). An approximate weight percentage of phases is listed in Table 15.

**Table 15** Phases present in the scaffolds after heat treatment at  $1200^\circ\text{C}$  (HA) and  $1250^\circ\text{C}$  (HA- $\text{SiO}_2$ )

	$\alpha$ -TCP (wt. %)	$\beta$ -TCP (wt. %)	Cristobalite (wt. %)	Other phases (wt. %) / type	$\alpha$ : $\beta$ -TCP
HA	50.6	49.4	–	–	1.02
HA_5% $\text{SiO}_2$	60.8	34	2.3	2.9 (walstromite)	1.79
HA_10% $\text{SiO}_2$	62	25.3	12.7	–	2.45
HA_15% $\text{SiO}_2$	59.3	21.1	17.4	2.2 ( $\text{Ca}_4(\text{PO}_4)_2\text{O}$ )	2.81
HA_20% $\text{SiO}_2$	65.2	12.5	20.3	2 ( $\text{Ca}_4(\text{PO}_4)_2\text{O}$ )	5.22

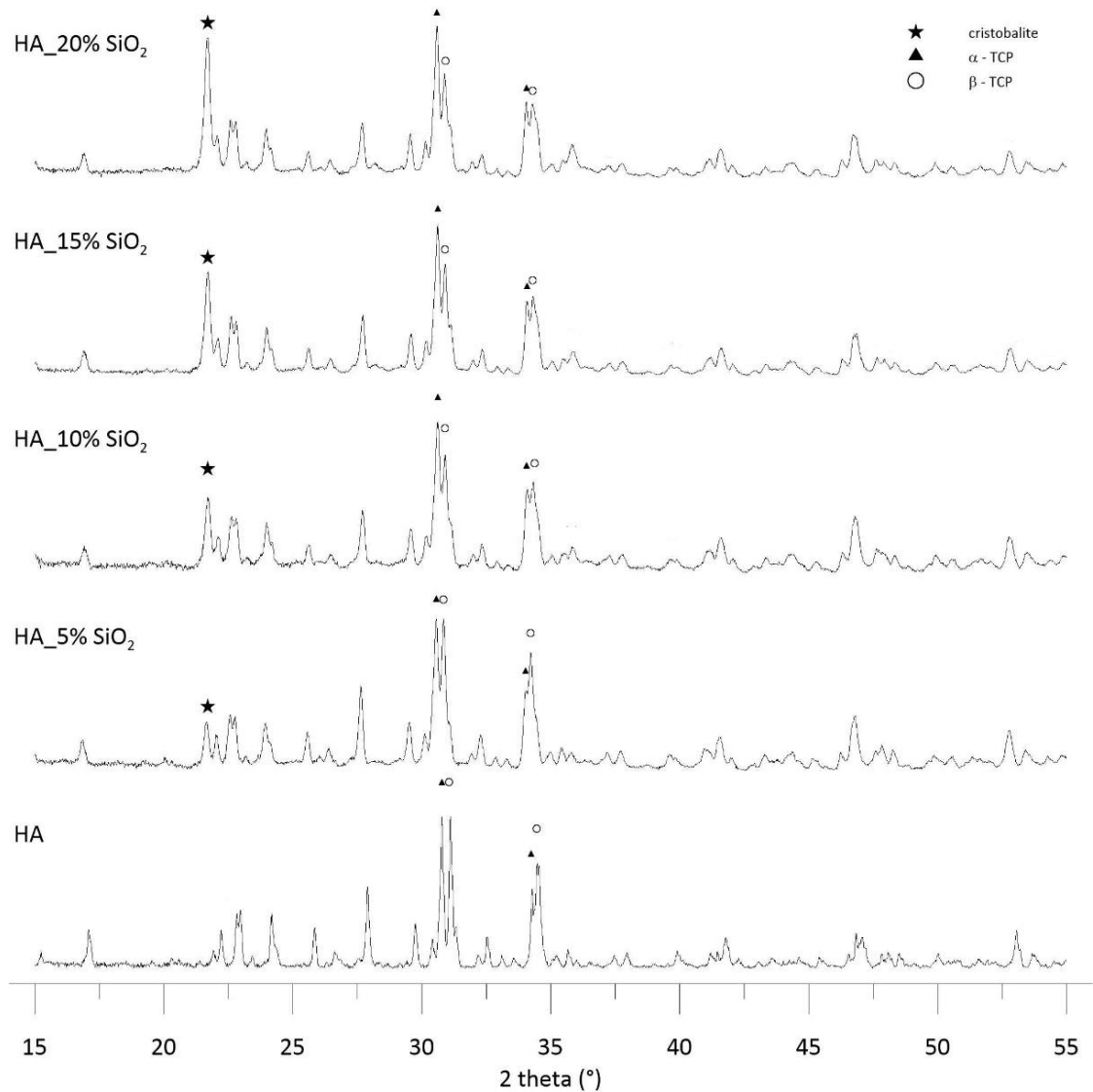


**Fig. 48** X-ray diffraction patterns of scaffolds containing 5–20 wt. %  $\text{SiO}_2$ , sintered at  $1250^\circ\text{C}$  for 3h and HA sintered at  $1200^\circ\text{C}$  for 3h

Results indicated that the ratio between  $\alpha$ -TCP and  $\beta$ -TCP increased with increasing amount of silica. Various researchers [78, 128, 137, 138] confirmed that addition of silica shifted the temperature of HA  $\rightarrow$   $\alpha$ -TCP transformation to lower value. The stable  $\alpha$ -TCP polymorph could be even formed during sintering above 700 °C [137-140] [128]. It was further reported that hydroxyapatite sintered in the presence of silica tended to transform to silica substituted tricalcium phosphate (Si- $\alpha$ -TCP) of formula  $\text{Ca}_3(\text{P}_{1-x}\text{Si}_x\text{O}_{4-x/2})_2$  [128, 140]. Having the same space group, the Si substituted  $\alpha$ -TCP can be distinguished from its stoichiometric counterpart via different lattice parameters [128, 140]. Measured and theoretical ( $\alpha$ -TCP, Si- $\alpha$ -TCP) lattice parameters are compared in Table 16.

**Table 16** Crystallographic parameters of pure and silicon substituted calcium phosphate phases

Phase	Lattice parameters	Space group	Ref.
Measured $\alpha$ -TCP	a = 12.880 Å; b = 27.291 Å; c = 12.878 Å; $\beta$ = 107.36°	P2 <sub>1</sub> /c	–
Measured Si- $\alpha$ -TCP	a = 12.843 Å; b = 27.337 Å; c = 12.856 Å; $\beta$ = 107.38°	P2 <sub>1</sub> /c	–
Calculated $\alpha$ -TCP	a = 12.878 Å; b = 27.291 Å; c = 15.257 Å; $\beta$ = 126.32°	P2 <sub>1</sub> /a	–
Calculated Si- $\alpha$ -TCP	a = 12.856 Å; b = 27.337 Å; c = 15.218 Å; $\beta$ = 126.35°	P2 <sub>1</sub> /a	–
$\alpha$ -TCP	a = 12.887 Å; b = 27.280 Å; c = 15.219 Å; $\beta$ = 126.20°	P2 <sub>1</sub> /a	[141]
Si- $\alpha$ -TCP (0.87 wt% Si)	a = 12.875 Å; b = 27.372 Å; c = 15.225 Å; $\beta$ = 126.30°	P2 <sub>1</sub> /a	[140]
Si-TCP	a = 12.863 Å; b = 27.357 Å; c = 15.232 Å; $\beta$ = 126.38°	P2 <sub>1</sub> /a	[78]

The obtained data of the lattice parameters indicated that  $\alpha$ -TCP was presumably substituted. This assumption would, however, require confirmation by further experiments, in which the content of silica would be reduced until total disappearing of cristobalite phase. Afterwards, the lattice parameters of tricalcium phosphates will be measured and the quantity of silicon in TCP will be evaluated by EDS analysis.

Silica substitution has a positive influence mainly on biological properties as was mentioned earlier. Nevertheless, the high total amount of cristobalite in structure suggested, that if sintered calcium phosphate scaffolds were substituted by silica, only small fraction of silica was incorporated into the lattice. The question was how the crystallized silica affected the biological and mechanical properties. A great deal of material research was focused on bioceramics containing amorphous silica such as Bioglass [42, 55, 67-69], (pseudo) wollastonite [142] and Si doped CaP [128, 143, 144]. On the other hand little is known about materials composed of crystalline silica in form of quartz or cristobalite. Cristobalite was in some studies consider being carcinogenic to human [145-147]. It is undeniable, however this feature was connected with inhalation of silica dust of mineral origin which can cause silicosis or lung cancer. Fubini [146] conducted several experiments and reported also problems related to cytotoxicity of cristobalite dust during cultivation *in vitro*. Nonetheless, the cytotoxicity disappeared upon heating to 1300 °C due to the loss of surface radicals, which play a crucial role in silica pathogenicity. The polished surface of quartz behaved unreactive even in aqueous medium. These indicates, that sintered cristobalite should not cause any adverse reaction. That was confirmed by Zocca [58] who studied ceramic scaffolds containing wollastonite with traces of cristobalite in the structure. He did not observe any cytotoxic behaviour. The safety of bioceramics containing Si was confirmed by Lai [148] who measured excretion of Si from biodegradable glass. He discovered that Si is secreted by urine. No increase of Si was found in kidney, liver, lung and lymph nodes.

The theoretical density of various composites, necessary to calculate the porosity, was calculated based on results of XRD analysis (see Table 17).

**Table 17** Theoretical density of scaffold components

Phase	Theoretical density (g·cm <sup>-3</sup> ) - XRD
α-TCP	2.832
β-TCP	3.485
Cristobalite	2.253
Ca <sub>4</sub> (PO <sub>4</sub> ) <sub>2</sub> O	3.077
walstromite	3.1827

### 5.4.3 Characterisation of structure and morphology of scaffolds

#### *Characterisation of scaffold cell size and its distribution*

Fig. 49 and Fig. 50 give an overview of scaffolds with various cell size. Structure of HA scaffold and HA–SiO<sub>2</sub> scaffold is very similar. As obvious from Table 18, pores (defined by cell size) were slightly larger in case of hydroxyapatite. Pores in HA scaffolds were larger although the linear shrinkage was decreasing with increasing silica content (Table 19). This discrepancy in result was caused by lower sintering temperature of hydroxyapatite (1200 °C instead of 1250 °C).

**Table 18** Pore sizes of HA-SiO<sub>2</sub> and HA

	Cell size (μm)	Size of cell windows (μm)
HA 60ppi	873 ± 55	262 ± 80
HA 75ppi	532 ± 67	204 ± 78
HA 90ppi	385 ± 60	116 ± 45
HA-SiO <sub>2</sub> 45ppi	1150 ± 198	536 ± 113
HA-SiO <sub>2</sub> 60ppi	736 ± 85	287 ± 92
HA-SiO <sub>2</sub> 75ppi	498 ± 58	168 ± 45
HA-SiO <sub>2</sub> 90ppi	375 ± 37	118 ± 35

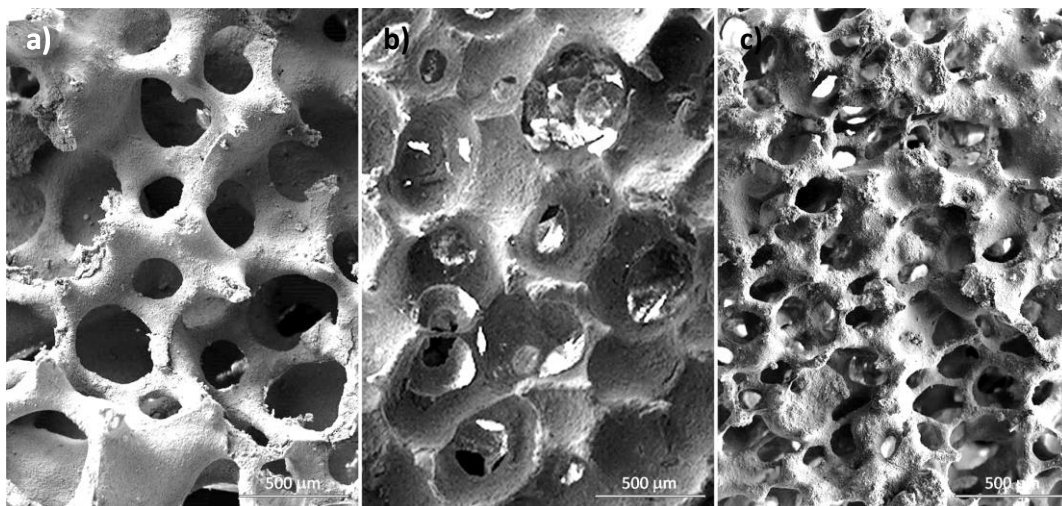


**Fig. 49** HA scaffolds sintered at 1200 °C/3h; porosity of the PU template: (a) 60 ppi, (b) 75 ppi, (c) 90 ppi

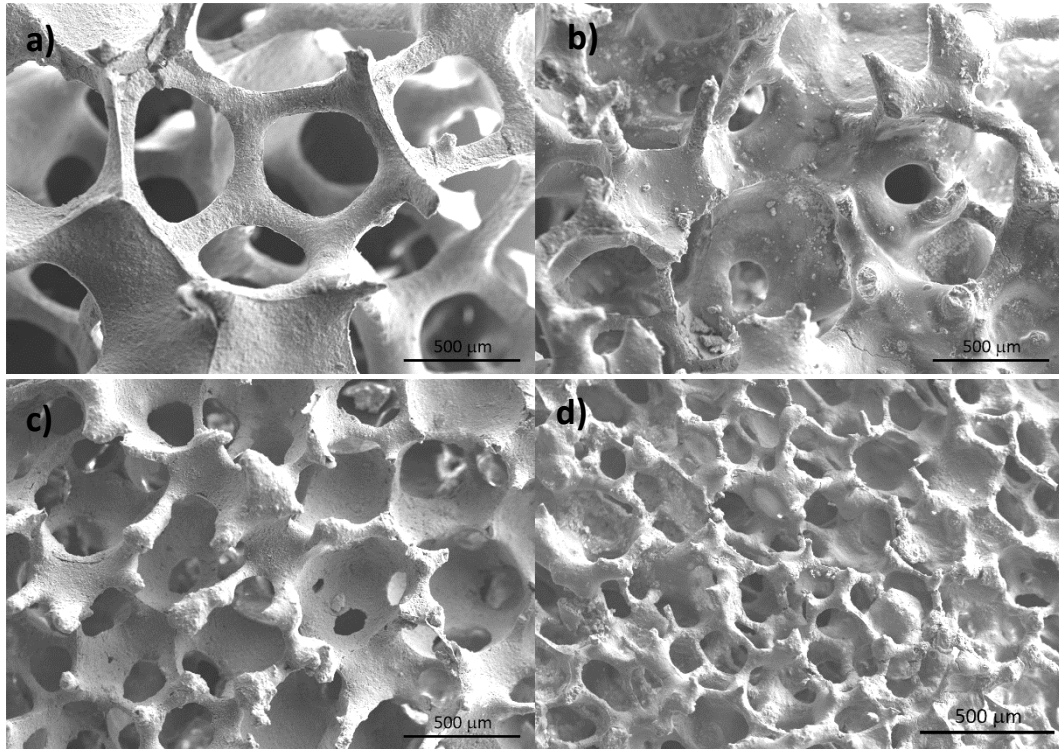


**Fig. 50** HA-10SiO<sub>2</sub> scaffolds sintered at 1250 °C/3h; porosity of the PU template: (a) 45 ppi, (b) 60 ppi, (c) 75 ppi, (d) 90 ppi

Distribution of scaffold cell sizes after sintering was narrow and unimodal. The pore size corresponded to the initial pore size of reticulated PU foam reduced by shrinkage. In terms of bone tissue engineering, the ideal starting template was that with porosity of 90 ppi. Both cell size and size of windows between cells were adequate for cell colonization and migration.

**Table 19** Linear shrinkage of scaffolds after sintering at 1250 °C/3h

sample	60 ppi	75 ppi	90 ppi	average linear shrinkage
HA				23.5 ± 3.1 %
HA-5SiO <sub>2</sub>	28.1 ± 1.4 %	25.8 ± 3.6 %	26.1 ± 2.9 %	26.6 ± 2.9 %
HA-10SiO <sub>2</sub>	25.6 ± 1.7 %	24.7 ± 4.2 %	25.1 ± 1.0 %	25.2 ± 2.3 %
HA-15SiO <sub>2</sub>	24.8 ± 1.0 %	23.2 ± 3.3 %	23.4 ± 1.2 %	23.8 ± 2.0 %
HA-20SiO <sub>2</sub>	23.3 ± 1.3 %	21.4 ± 2.9 %	22.3 ± 1.7 %	22.4 ± 2.1 %

Table 19 summarizes the linear shrinkage of scaffolds containing different amount of silica in structure. It shows that shrinkage is inversely proportional to silica content. The lower than expected shrinkage of pure hydroxyapatite was caused by lower sintering temperature (1200 °C instead of 1250 °C).

#### 5.4.4 Characterisation of pore structure of scaffolds

Strut thickness and porosity was affected by properties of slurry and by processing parameters. The lower pore size of template, the lower concentration of powder was necessary to use. Fig. 51 illustrates a hollow strut as a consequence of replication of reticulated PU foam.

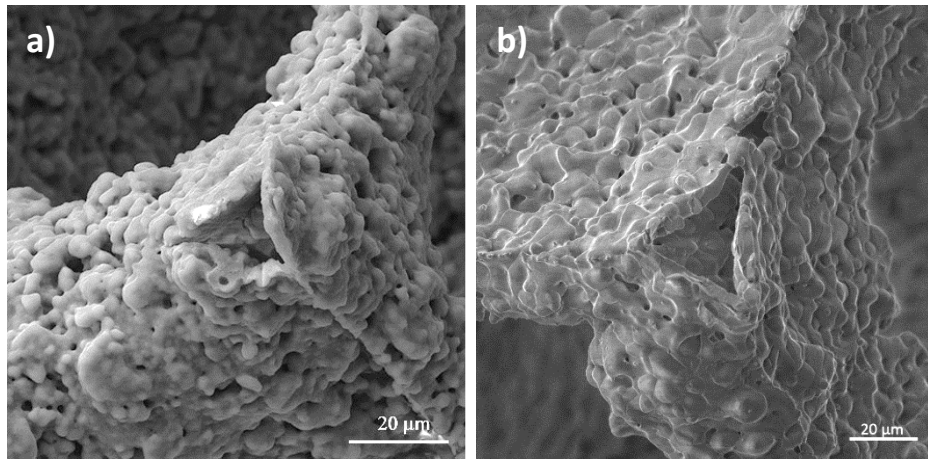


**Fig. 51** Strut morphology (a) hollow strut HA5SiO<sub>2</sub>, 75 ppi; (b) hollow strut HA, 75 ppi

Porosity was easily tuneable by viscosity of the slurry, by repeating the coating process and finally by efficiency of removing the extra slurry by compress air. Samples with huge range of porosity (45–98%) were prepared. If the porosity was lower than 50%, the macropores were almost closed and remaining pores were too small for cell colonization. Scaffolds with 60–80% porosity exhibited interconnected pores with seldom closed walls – it seemed to be ideal porosity due to scaffold morphology and strength. If the porosity exceeded 92%, the struts were very thin causing the brittle behaviour of sintered scaffold.

#### 5.4.5 Biological properties - bioactivity

Bioactivity of prepared scaffolds was tested in Eagle medium instead of in simulated body fluid. The ionic composition of MEM (minimum essential medium Eagle) was comparable to SBF solution. Fig. 52 presents the overview of surface morphology of prepared scaffolds before and after immersion in medium. After 3day cultivation in direct contact assay, the surface of scaffolds was covered by newly formed apatite layer. Samples containing silica were fully covered whereas layer of apatite precipitated on pure CaP were not continuous. It could have been caused by high porosity of the sample. Newly formed apatite layer, nucleated under the conditions simulated in vivo indicates a good bioactivity of scaffolds containing cristobalite. According to Pietak [128] the bioactivity could have been influenced by presented osteoblast cells. He reported that Si- $\alpha$ -TCP showed only little reactivity in SBF environment. If SBF contained serum proteins, the precipitation of HCA like phase would have been significantly faster. He reported the complete transformation to plate like HA in the presence of osteoblast cells. On the other hand Tuck [149] observed biomimetic precipitation at the surface of Si- $\alpha$ -TCP scaffold incubated in SBF. It shows that Si promotes biomimetic precipitation on Si- $\alpha$ -TCP by higher solubility of the material due to creation of defects in the lattice [78, 128, 150]. Pietac studied the influence of surface charge, which is electronegative due to substitution of SiO<sub>4</sub><sup>4-</sup> for PO<sub>4</sub><sup>3-</sup>, this can facilitate surface adhesion, rapid biomimetic precipitation and can lead to higher biological activity [128, 151].

Also wollastonite (CaSiO<sub>3</sub>) based ceramic is considered being bioactive and can be used in tissue engineering [59, 152]. Ionic products of pseudowollastonite enhanced osteoblast activities [128, 142].

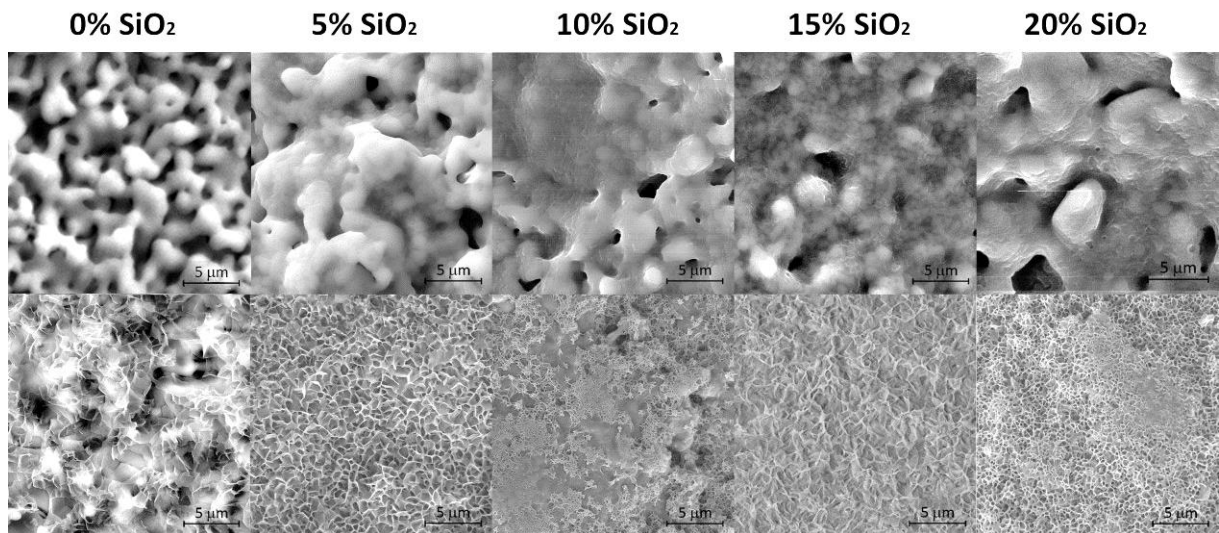


**Fig. 52** Surfaces of HA-SiO<sub>2</sub> scaffolds before and after 3 day incubation in Eagle Medium.

### ***Cell colonization***

Cell colonization was tested in direct contact assay with human osteosarcoma cells. The percentage of occupied surface corresponded to the amount of seeded cells (3500 cells/cm<sup>2</sup> after 3 days; see Fig. 53). Results summarized in Fig. 54 indicates that silica slightly improved cell adhesion.

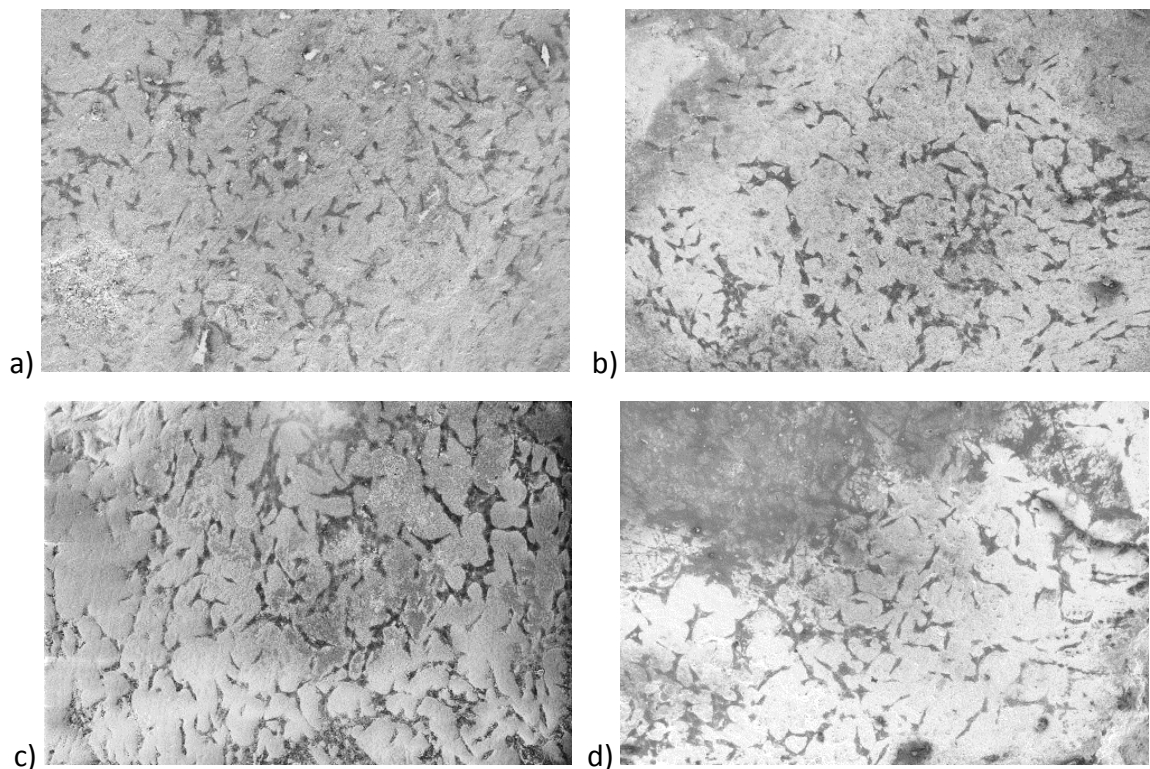


**Fig. 53** MG 63 cells adhered to the surface of CaP / silica scaffolds: (a) 5% SiO<sub>2</sub>, (b) 10% SiO<sub>2</sub>, (c) 15% SiO<sub>2</sub>, (d) 20% SiO<sub>2</sub>

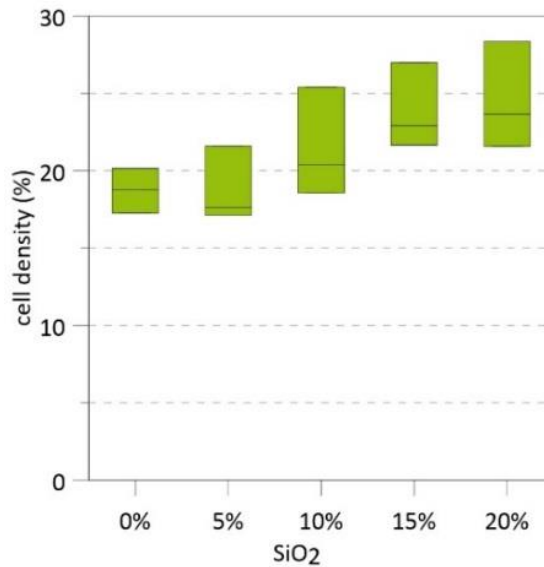


**Fig. 54** Percentage of adhered cells on the surface after 3D cultivation

The cell morphology of MG 63 cells is detailed in Fig. 55. Please note, that the scale bar is different for the first figure, HA scaffold. The cell morphology was the typical for MG63 cell line in the case of cells adhered to Si-TCP surface – independent on silica concentration. The cells were smaller on unsubstituted TC

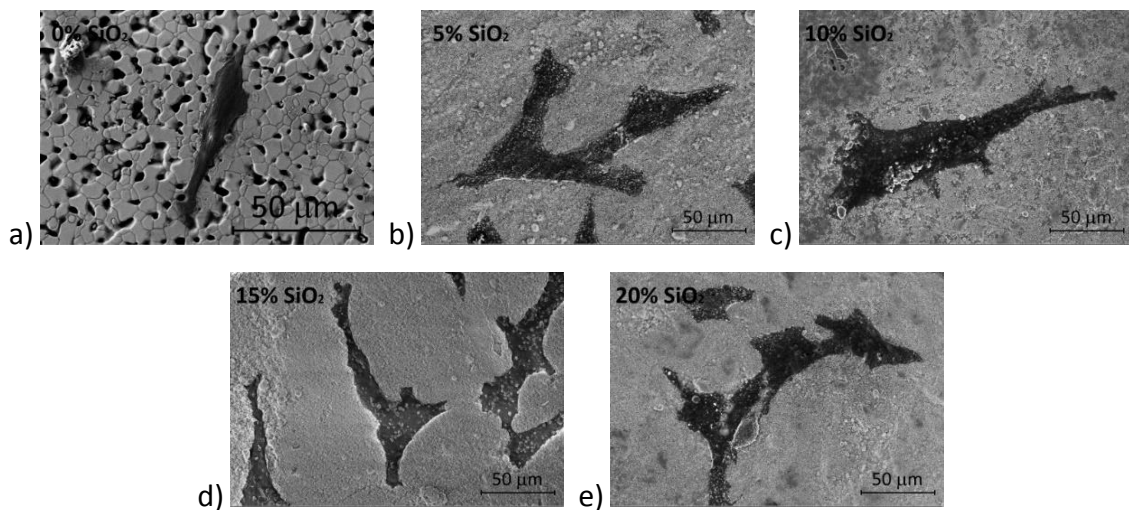
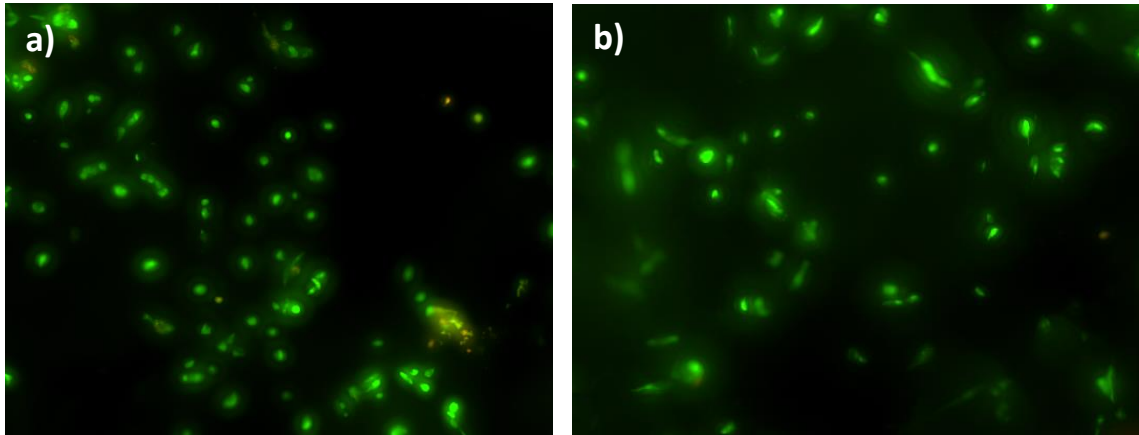


**Fig. 55** Morphology of cells adhered to HA and HA – SiO<sub>2</sub> scaffolds. Please note the different scale bar in the first image.

#### 5.4.6 Biocompatibility of calcium phosphate scaffolds with human cells

Calcium phosphate scaffolds were seeded with human adipose-derived stem cells (ADSC) to assess material cytotoxicity. It was performed by determination of cell viability after 24 hours of cell cultivation with lower concentration (50.000/100 μl). Live cells exhibit green fluorescence after acridine orange staining and dead cells exhibit red fluorescence after ethidium bromide staining. Cells on all samples exhibited green fluorescence and a few of them exhibited red (less than 1%), which is physiological state, indicating that cells were viable on materials. All the materials were found biocompatible and nontoxic (see Fig. 56).

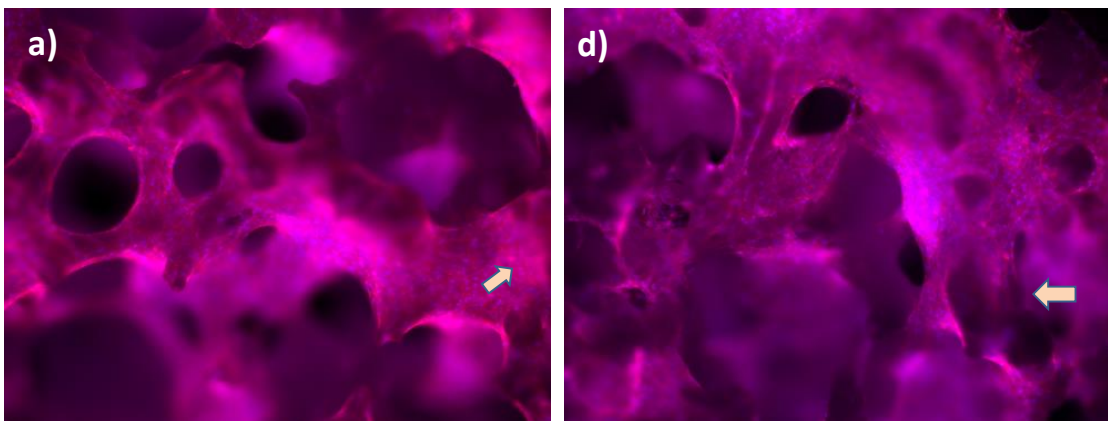


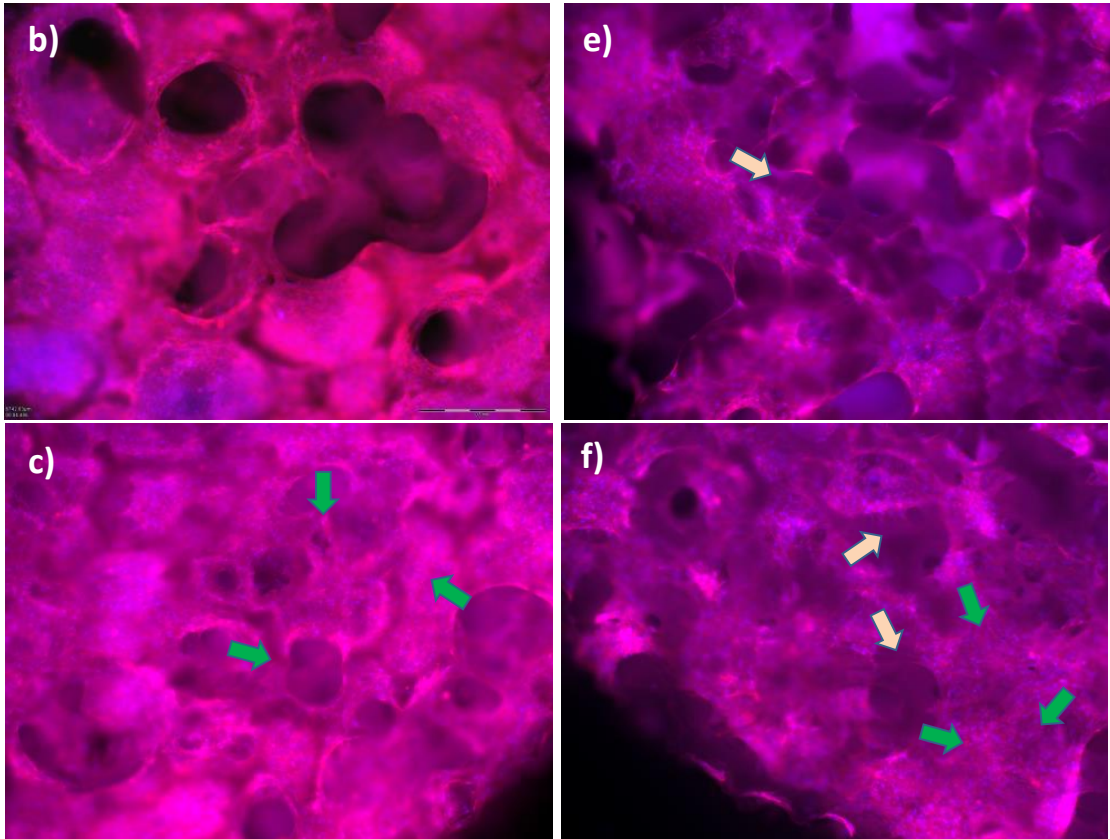


**Fig. 56** Cell viability assessment after 24 hours of cultivation. Cells seeded on scaffolds exhibited green fluorescence indicating viable cells (Merged images of red and green fluorescence) for both materials: (a) CaP, (b) Si-CaP

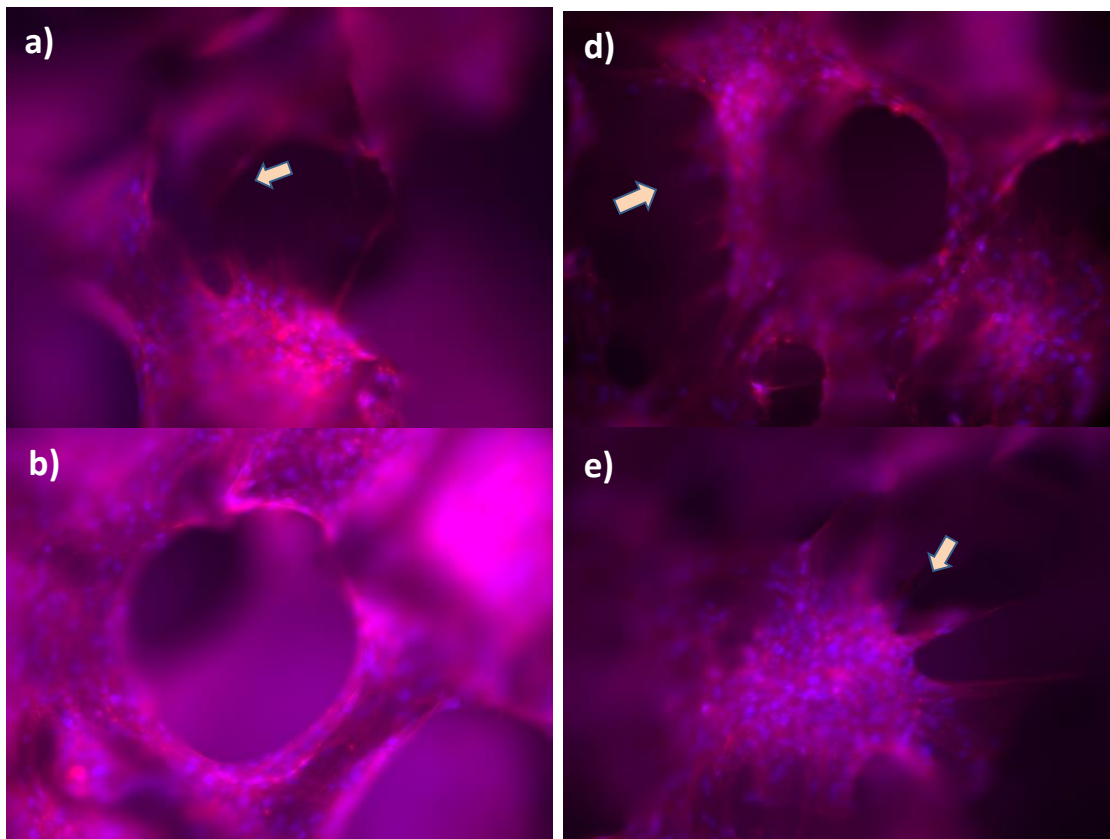
Further biological analyses of materials were investigated to assess the cell adhesion and morphology. Nuclei and cytoskeleton were visualised to evaluate their shape and distribution, respectively, and observed detailed morphological features. Overall, the cells growing in contact with materials adhered and covered its surfaces. Morphology of cells seeded on scaffolds was comparable to standard cell appearance on Petri dishes, in high concentration cultivation. Cells grew in monolayers and ADSCs formed protrusions in some parts of scaffolds indicating active interaction and adhesion to materials. This was mainly detected on materials with larger pores (60 and 75 ppi) and that was marked in figures by white arrows (Fig. 58). Even more filopodia (protrusion) formation was observed on hydroxyapatite-silicium materials, still further analysis of cell behaviour (e.g. proliferation, focal adhesion formation) should be assessed for more detailed characterization and difference evaluation.

There was observed also significant phenomenon of overgrowing pores and connecting cells in sheets (Fig. 57) on scaffolds with small pores (porosity 90), both materials, documenting natural character of cell behaviour and nontoxic character of materials. Taken together, no signs of blabbing of cytoplasmic membrane, regularly shaped nuclei, well developed network of actin and firm contacts with the supporting materials was observed and materials have been found to be biocompatible and suitable for cell culture applications.





**Fig. 57** Morphological features of the cells growing in calcium phosphate: (a) 60 ppi, (b) 75 ppi, (c) 90 ppi and Silica/calcium phosphate (d) 60 ppi, (e) 75 ppi, (f) 90 ppi) scaffolds. Red color stains actin and the blue visualizes chromatin. White arrows indicate formation of filopodias, green arrows cells forming sheets over the pores of scaffolds.



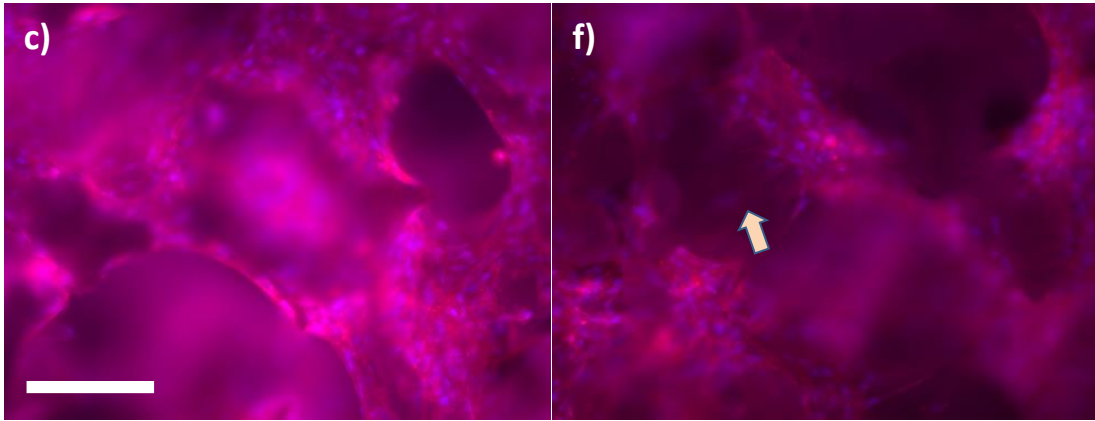


**Fig. 58** Detail representation of cellular adhesion and spreading of adipose-derived stem cells on hydroxyapatite scaffold (porosity A-60, B-75, C-90) and hydroxyapatite-silicium (D-60, E-75, F-90). White arrows indicate formation of filopodias. Scale bar 200  $\mu\text{m}$ .

### 5.4.7 Mechanical properties

Compressive strength of samples with initial pore size 60, 75 and 90 ppi was used for evaluation of the influence of silica content on mechanical properties of scaffolds.

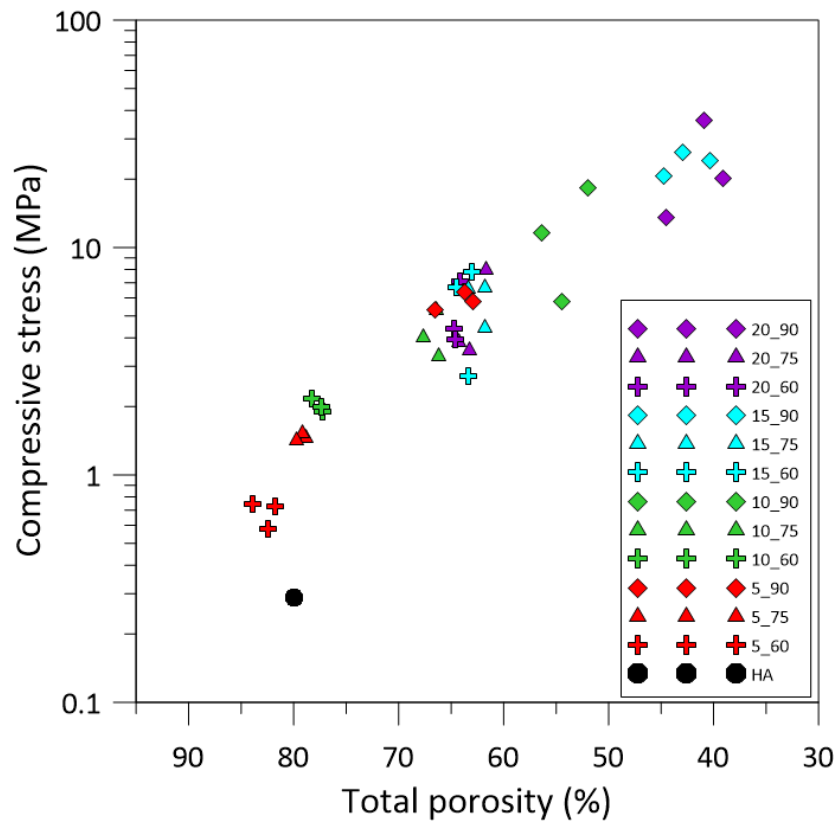


**Fig. 59** Dependence of compressive strength on total porosity

Fig. 59 presents dependence of compressive strength on porosity of HA/SiO<sub>2</sub> scaffolds. Results indicated that strength exponentially increased with increasing density of scaffolds according to the Ryshkewitch-Duckworth [153, 154] equation (eq. Xx).

$$\sigma = \sigma_0 \cdot e^{-cp} \quad (8)$$

Where the  $\sigma_0$  is strength at zero porosity,  $c$  is constant (4–7 according to porosity) and  $p$  is porosity.

It is evident that silica had a positive influence on the strength, no matter if there were 5 or 20 percent of  $\text{SiO}_2$  in HA/ $\text{SiO}_2$  scaffolds. Moreover, it seemed that pore sizes also had negligible effect on final strength. One of the requirements imposed on the materials used in tissue engineering are properties similar to those of replaced tissues. In the case of cancellous bone, the compressive strength values were reported between 1.5 to 38 MPa [155], usually 2–20 MPa [19]. Strength-porosity dependence indicated that optimal strength for bone tissue replacement was achieved on the samples with lower porosity than 80%. Therefore compressive strength of the samples reinforced by silica are similar with those of bone and this type of composite material can be potentially used in bone tissue engineering.

#### **5.4.8 Summary of Chapter 5.4**

Calcium phosphate 3D interconnected scaffolds with different pore sizes were fabricated with and without silica addition. Pore dimensions ranging between 375 and 1150  $\mu\text{m}$  were depended on the pore size of four templates which were replicated. The average window size between two interconnected pores was from 118 to 536  $\mu\text{m}$ , ideal for cell penetration. Addition of silica (5 – 20 wt. %) strongly influenced the phase transformation of hydroxyapatite to  $\beta$ -TCP and  $\alpha$ -TCP, respectively. The ratio of  $\alpha$ -TCP to  $\beta$ -TCP increased fivefold with increasing silica content. Lattice parameters indicated that TCP was substituted by Si. However, almost all amorphous silica was transformed to the cristobalite crystalline phase. Addition of cristobalite did not negatively influence the biological properties as was confirmed by two methods – by direct contact assay with osteosarcoma cell line MG63. After three days of cultivation, the surfaces were totally covered by newly formed apatite layer which indicates excellent bioactive behaviour. Influence of 10% addition of silica on cell viability of adipose derived stem cells was also studied. The cell viability increased with addition of silica; it seemed that silica supported cell adhesion. This trend was followed for the three pore sizes, with the maximum effect noted for the scaffolds using 90 ppi polymer pore size. The main enhancement was, nevertheless, observed on mechanical properties. The compressive strength of calcium phosphate scaffold bonded by polyvinylalcohol was only 0.3 MPa at 80% porosity. The strength of scaffolds composed of silica reinforced calcium phosphates on the contrary exceeded 20 MPa at 50% porosity.

### **5.5 Calcium phosphate scaffolds produced from CaP / PU composite foam**

#### **5.5.1 Thermal decomposition of CaP / PU scaffold**

As was mentioned in Chapter 4.3.2, ceramic foams were obtained by burning out the polymer from the CaP / PU composites. To determine the temperature at which the thermal decomposition of polyurethanes is finished, the thermal analysis was carried out.

In general, the thermal degradation of polyurethanes in air atmosphere is a complex process involving oxidation of the initial polyol and isocyanate components, which is followed

by the thermal decomposition that leads namely to the formation of amines, water and carbon dioxide [156, 157].

TA curves (performed on the sample HA100\_2\_105) are shown in Fig. 60. The total weight loss as a consequence of decomposition was 50 wt. %, which corresponded to the weight content of polyurethane in the input composition. The first endothermic drop on DTA curve below 100 °C was due to water evaporation. Increasing the temperature above 200 °C, the polyurethane started to decompose by a typical two stage process as is evident from the DTG and DTA curves. The weight loss, around 350 °C was caused by the degradation (oxidation) of hydroxyl and amino groups whereas the second stage, around 600 °C was mainly associated with the oxidation of the residual carbon.

Even though the decomposition of organic compounds was completely finished around 750 °C, the CaP / PU composites were heat treated at 800 °C/2 h to ensure the sufficient handling strength of presintered ceramic bodies.

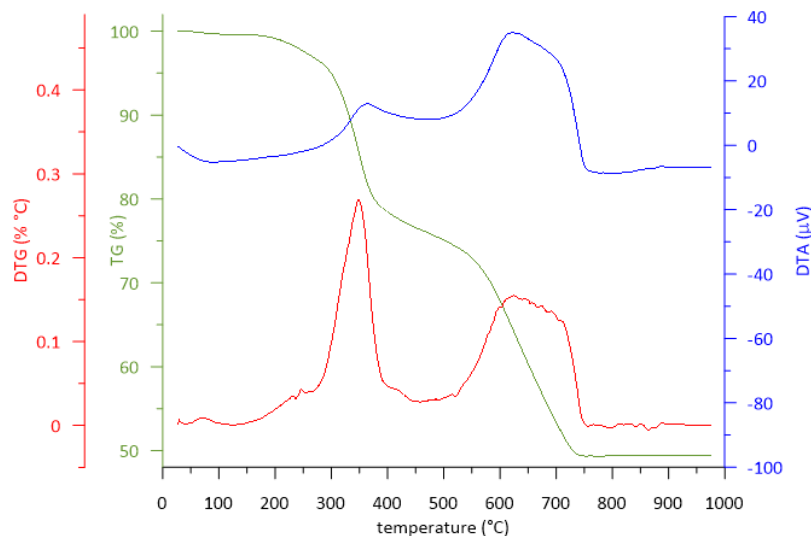


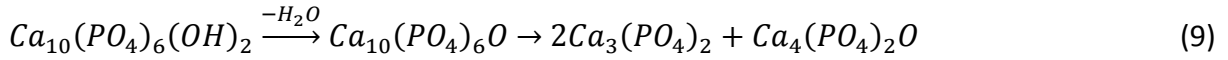
**Fig. 60** TA analysis of polyurethane composite (HA100\_2\_105)

### 5.5.2 Phase composition

Hydroxyapatite was chosen as a starting powder to fill the polyurethane. Two powders were used – untreated commercial one (Fluka) and the same one calcined at 800 °C/1 h ( $\uparrow 3$  °C/min). The calcination of the powder had several benefits, such as elimination of organic impurities or coarsening the grains which facilitates processing of ceramics [158].

According to the results of thermal analysis of hydroxyapatite, which are shown in Fig. 61, approximately 5 wt. % of impurities were fired below the calcination temperature. After the evaporation of physically adsorbed water, the organic residues (mainly acetates) were oxidized between 200 and 500 °C. Above 600 °C, hydroxyapatite was gradually dehydroxylated, having released of OH<sup>-</sup> ions (H<sub>2</sub>O) and progressively transformed through oxyhydroxyapatite (Ca<sub>10</sub>(PO<sub>4</sub>)<sub>6</sub>(OH)<sub>2-2x</sub>Ox□x) to oxyapatite (Ca<sub>10</sub>(PO<sub>4</sub>)<sub>6</sub>O) [159]. With further increasing of temperature (above 1100 °C), the oxyapatite has been decomposed into other

calcium phosphates such as  $\alpha$ ,  $\beta$ -TCP ( $\text{Ca}_3(\text{PO}_4)_2$ ) and tetracalcium phosphates ( $\text{Ca}_4(\text{PO}_4)_2\text{O}$ ), according to the following reactions [135, 136, 160]:



or

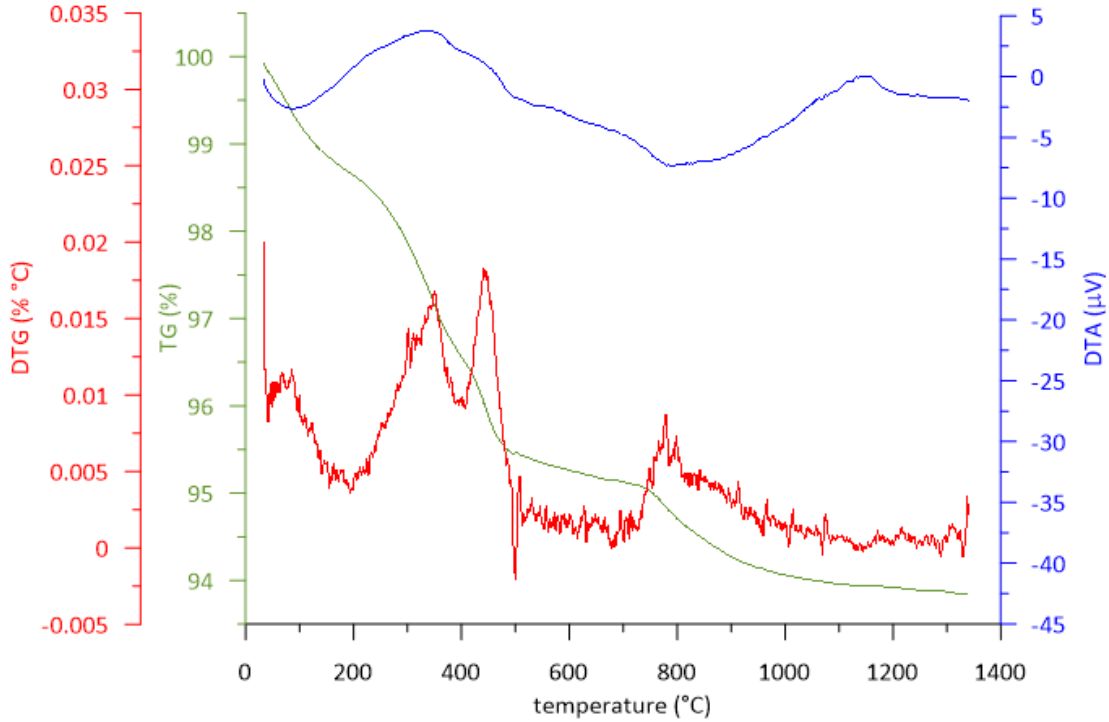
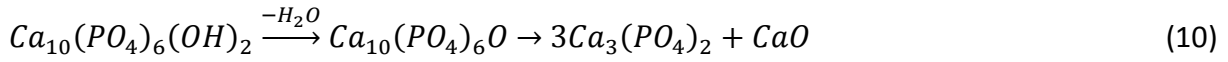


**Fig. 61** TA analysis of commercial hydroxyapatite (Fluka)

The thermal analysis cannot distinguish the specific phases of decomposition process of hydroxyapatite and therefore the phase composition of two started powders and ceramic scaffolds sintered at three different temperatures were determined by means of XRD analysis. All measured data are summarized in Fig. 62. XRD peaks of diffraction patterns of uncalcined starting powder (see Fig. 62 (a)) almost corresponded to the standard in powder diffraction file of hydroxyapatite 22059-ICSD, the rest (less than 10%) was identified as monetite ( $\text{CaP}_3\text{OH}$ ). After the calcination at 800 °C (see Fig. 62 (b)), the quantity of hydroxyapatite in composition decreased to 80 wt. %. Despite the expectation, no oxyapatite was identified, possibly due to rehydroxylation. However, already at this temperature, hydroxyapatite was partially decomposed into beta tricalcium phosphate  $\beta$ -TCP (20 wt. %). Scaffold sintered at 1050 °C contained about 55 wt. % of hydroxyapatite and 45 wt. % of  $\beta$ -TCP. With an increasing sintering temperature, the quantity of hydroxyapatite decreased to 4 wt. %, the rest was decomposed into calcium phosphates (48 wt. %  $\alpha$ -TCP and 48 wt. %  $\beta$ -TCP). This is an interesting result because according to some other authors [136], hydroxyapatite should remain stable until at least 1200 °C. Regard to tissue engineering, the decomposition of HA is not undesirable process because the degradable calcium phosphates follow the current trend in medicine supporting regeneration instead of permanently replacements [161].

Furthermore, patterns show that the mass fraction of more soluble  $\alpha$ -TCP increased with the temperature (from 48 wt. % at 1200 °C to 75% at 1350 °C). This indicates that structures obtained at high sintering temperature would be at the same time more soluble in body environment, i.e. would degrade faster than their less dense counterparts [27] and moreover it seems that the degradation rate could be controlled by the sintering temperature. At samples sintered at 1350 °C, 1.5 wt% of tetracalcium phosphate was found in the xrd pattern, it suggest that degradation occurs according to the equation Eq. 10.

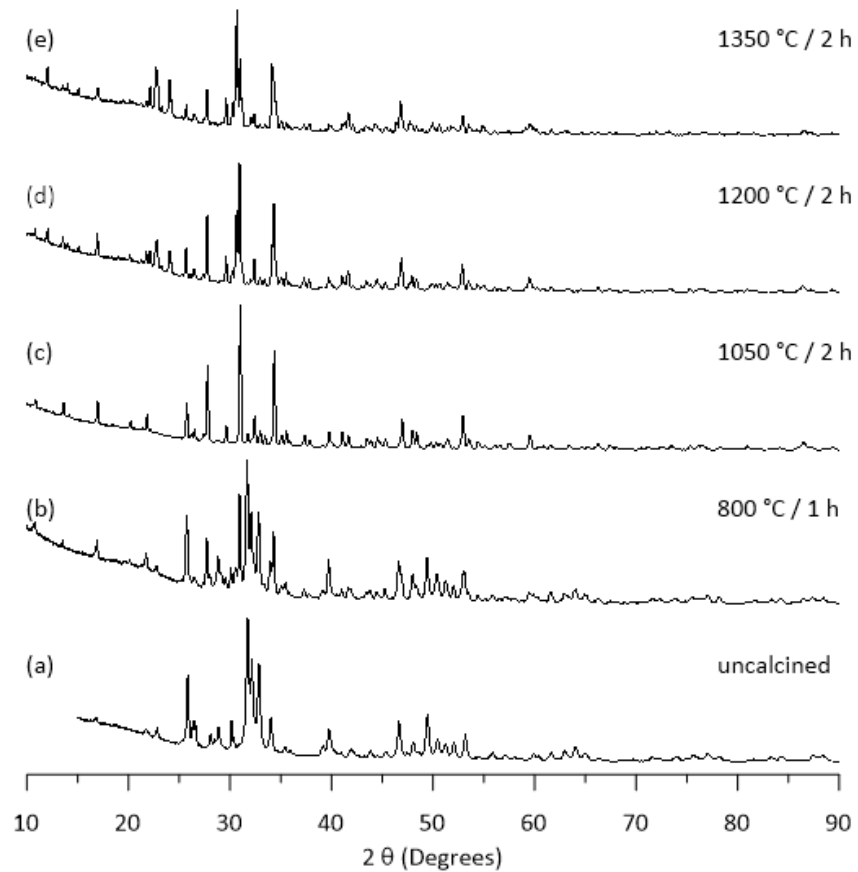


**Fig. 62** XRD patterns of (a) commercial HA powder; (b) HA powder calcined at 800 °C; (c) HA sintered at 1050 °C/2 h; (d) at 1200 °C/2 h and (e) at 1350°C/2 h.

### 5.5.3 Foam characterisation - influence of chemical composition

Influence of the amount of added water, isocyanate index, ratio between calcium phosphate and polyurethane referred as CaP/PU ratio and sintering temperature on the final morphology was evaluated. Calculated values of total porosity are summarized in Table 20. and in Fig. 63. Individual effects will be discussed in detail in the following chapters.

**Table 20** Scaffold composition and total porosity at different temperatures

sample	Total porosity (%) calculated	Total porosity (%) 1050 °C/2 h	Total porosity (%) 1200 °C/2 h	Total porosity (%) 1350 °C/2 h
HA100_0_105	91.0 ± 1.8	87.0 ± 0.9	75.3	78.1
HA100_1_105	92.1 ± 0.7	86.9	83.6	83.6
HA100_2_105	92.3 ± 1.3	90.5	79.0	81.0

HA100_3_105	91.4 ± 0.7	85.2	79.5	82.2
HA100_4_105	92.2 ± 1.0	87.5	81.6	84.8
HA100_5_105	92.0 ± 0.5	87.4	81.3	80.4
HAu100_0_105	91.3 ± 0.6	83.0 ± 1.9	79.3	81.3
HAu100_2_105	93.9 ± 0.9	87.9	87.8	85.8
HAu100_4_105	90.7 ± 1.0	77.9	75.1	78.5
HA62_0_105	96.2 ± 0.1	90.9	88.4	88.2
HA56_1_105	97.0 ± 0.1	91.0	89.4	89.0
HA51_2_105	97.5 ± 0.6	91.7	91.3	90.7
HA47_3_105	97.3 ± 0.3	93.6	92.6	×
HA43_4_105	97.9 ± 0.2	×	×	×
HA40_5_105	98.0 ± 0.2	×	×	×
HA100_2_75	94.8 ± 0.4	90.7 ± 0.1	87.6	88.0
HA100_2_85	91.3 ± 0.5	85.3 ± 1.8	79.0	76.9
HA100_2_95	93.0 ± 0.6	89.7 ± 0.6	81.8	82.7
HA100_2_115	93.0 ± 1.0	89.4	81.1	81.5
HA100_2_125	92.9 ± 0.8	86.7	84.5	84.1
HA40_2_105	97.8 ± 0.1	91.4	89.9	90.3
HA60_2_105	95.5 ± 0.1	91.7 ± 0.3	88.7	90.2
HA80_2_105	93.6 ± 0.4	86.8 ± 0.6	84.4	83.6
HA120_2_105	92.4	77.3	76.5	75.9
HA40_4_105	97.2 ± 0.2	×	×	×
HA60_4_105	96.4 ± 0.4	×	×	90.6
HA80_4_105	96.9 ± 0.7	90.0	87.5	88.7
HAu61_0_107	97.4 ± 0.5	91.2	89.7 ± 0.4	89.3
TCP74_0.5_95	96.8 ± 0.1	91.1	89.5 ± 0.3	76.1 ± 4.4

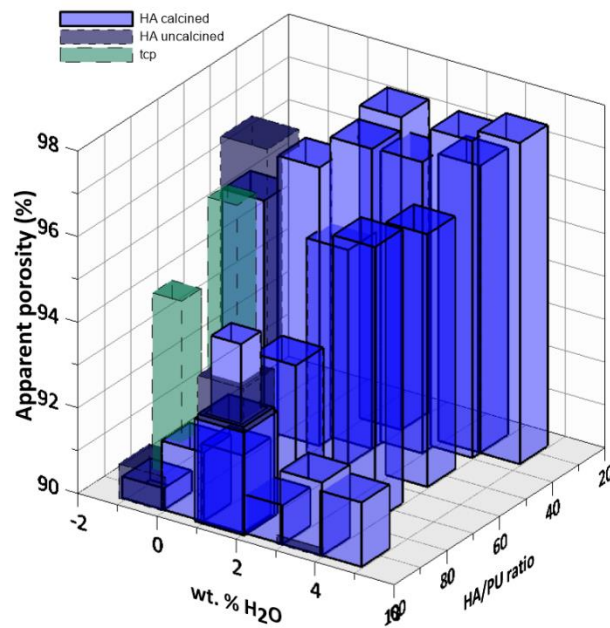


**Fig. 63** Influence of water and powder content on total porosity after burning the polyurethane. Width of columns is growing in dependence on  $I_{NCO}$  from 75 to 105.



### ***Influence of the powder composition***

Effect of two hydroxyapatite powders and one  $\beta$ -TCP powder on processability and properties of CaP / PU composites were studied. The specific surface area of  $\beta$ -TCP powder was  $12.4 \text{ m}^2/\text{g}$ . The processability of the foams was quite good, resulting in a regular porous structure with narrow distribution of pore sizes (see detail in Fig. 64). Total porosity of  $\beta$ -TCP / PU before sintering was slightly higher than HA / PU. If the content of the powder was lower than the content of the polyurethane and the  $I_{\text{NCO}}$  was below 100, the prepared foams were soft and could have been easily formed into complex shapes (Fig. 64) without damaging the macrostructure. Despite these promising results,  $\beta$ -TCP had been abandoned, because it behaved thermally unstable and even at  $1200 \text{ }^\circ\text{C}$  it adversely reacted with alumina substrate during sintering in air. After the sintering at  $1350 \text{ }^\circ\text{C}/2\text{h}$ , the final volume approximately eight times shrunk and macroporous structure was totally lost.

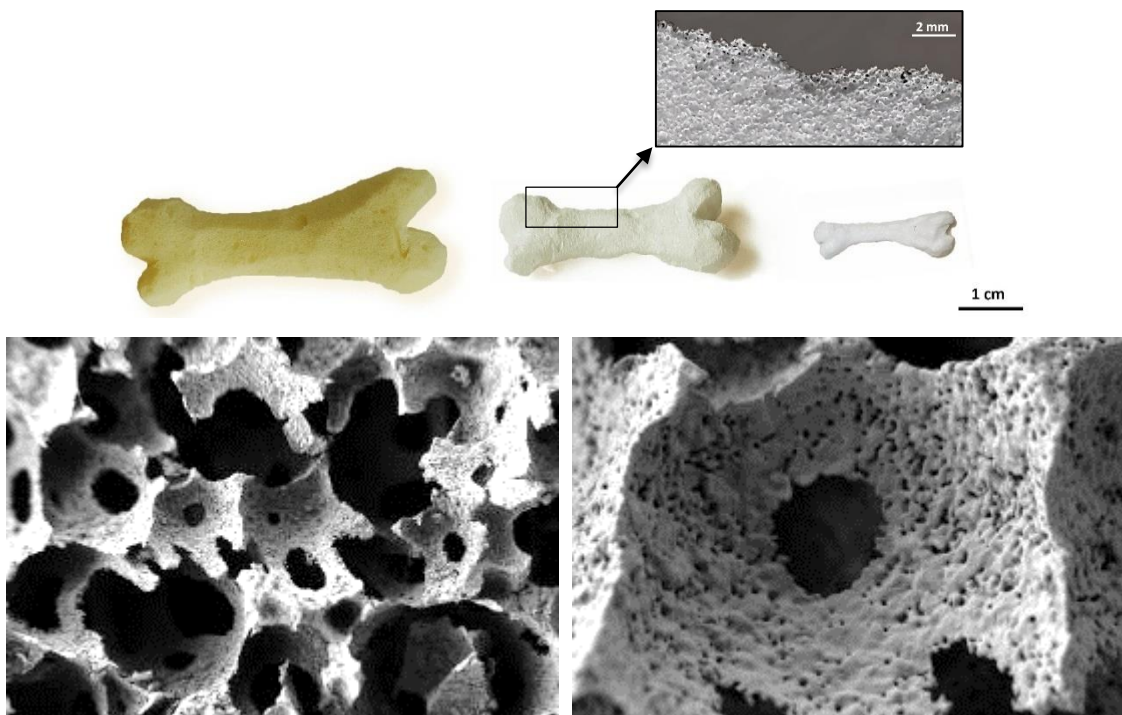


**Fig. 64** Processing of  $\beta$ -TCP scaffold (TCP74\_0.5\_95). From left to right: shaped  $\beta$ -TCP/PU composite, heat treated at  $800 \text{ }^\circ\text{C}$  and sintered at  $1350^\circ\text{C}/2\text{h}$ ; (b) scaffold sintered at  $1200 \text{ }^\circ\text{C}/2 \text{ h}$ .

The second studied system was based on hydroxyapatite powder and polyurethane. As was mentioned and explained in chapter 5.5.2, some of the powder was calcined, resulting in decrease of the specific surface area from  $33.8 \text{ m}^2/\text{g}$  to  $8.1 \text{ m}^2/\text{g}$ . Powder calcination influenced the behaviour of powder/polyol/MDI mixture and final properties of prepared foams. Since uncalcined powder exhibited high specific surface area, it was difficult to mix all powder with the polyol. It was necessary to mix the part of the powder (especially in the sample with 4 pphp  $\text{H}_2\text{O}$ ) with diisocyanate before the final mixing of all components. The very high viscosity of resulted mixture negatively influenced the microstructure of prepared foams. It seemed that components containing uncalcined powder had worse foaming ability, which was confirmed by lower apparent porosity. Microstructure of the sintered foam is shown in Fig. 65c. Next drawback of using too viscous mixtures was incorporation of irregular pores

into the structure as a result of not homogeneously filled mould (it is demonstrated in Fig. 65a). The prepared foams were moreover more rigid in comparison with their counterparts prepared from calcined powder. The rigidity complicated the ability to cut and shape them after the hardening.

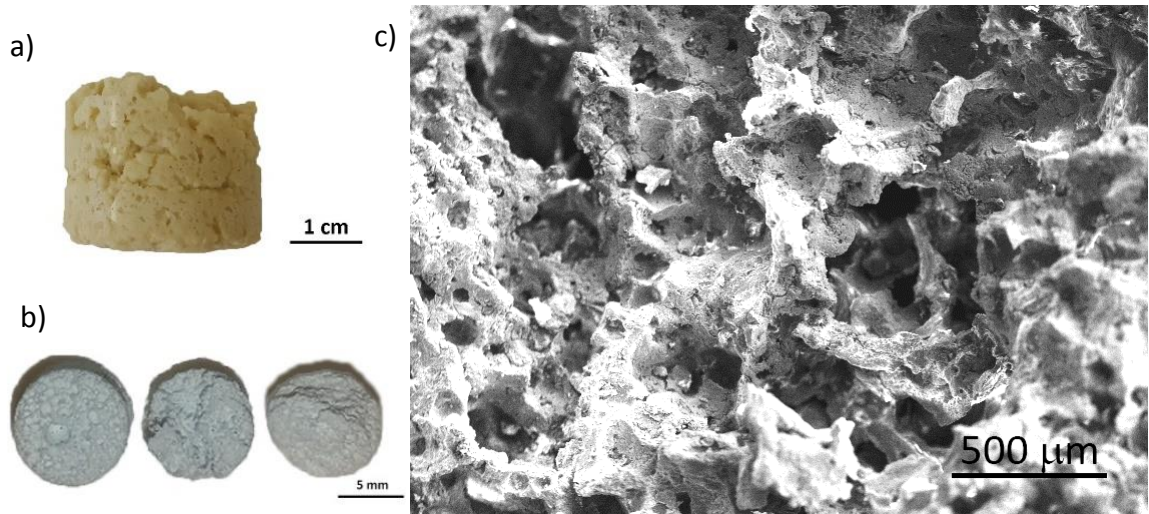


**Fig. 65** Scaffold prepared from uncalcined powder: (a) CaP/PU composite after hardening (HAu 100\_4\_105), (b) samples containing 0, 2, 4 pphp sintered at 1050 °C, (c) SEM micrograph of HAU 100\_2\_105\_1200.

#### ***Effect of added water***

Two sets of samples with an increasing amount of added water were evaluated (see Fig. 66 and Fig. 67). Pictures indicated that water addition (from 0 to 5 pphp) had a significant impact on the structure of the composites, mainly on pore size. During the processing water as blowing agent reacted with the NCO-functional groups of diisocyanate and formed unstable carbamic acid which immediately decomposed into an amine and carbon dioxide which caused generation of pores in the structure [162]. Reaction ran according to the following scheme:

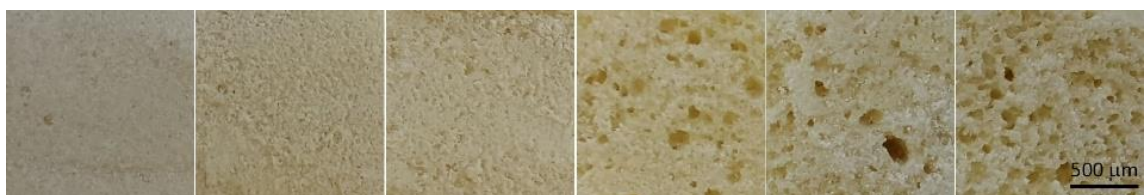
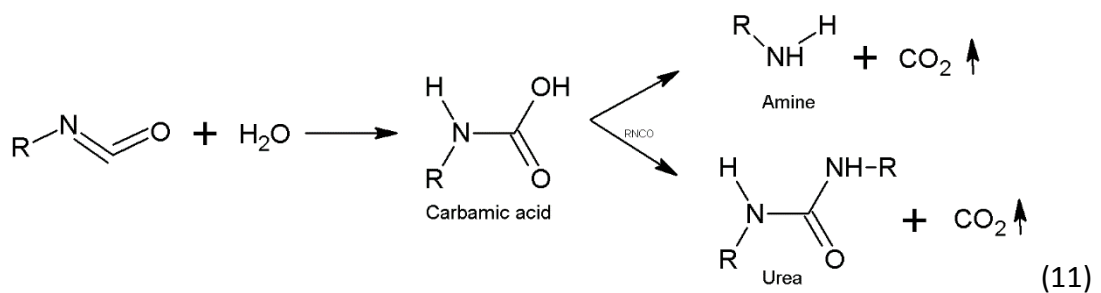


**Fig. 66** CaP/PU foams having  $\frac{\text{ha}}{\text{pu}} \text{ ratio} = 1$  and  $I_{\text{NCO}} = 105$  (water content increasing from 0 wt.% (left) to 5 wt% (right) of polyol)



**Fig. 67** CaP/PU foams having  $\frac{ha}{polyol} \text{ ratio} = 1$  and  $I_{NCO} = 105$  (water content increasing from 0 wt.% (left) to 5 wt% /(right) of polyol)

Theoretically, 1 mol of  $H_2O$  would create  $22.4 \text{ dm}^3$  of  $CO_2$ . If all the created bubbles were stable and remained in the foam, the total volume (and apparent porosity) of the foam would rise with the increasing amount of water. However, this was not experimentally confirmed; the results summarized in Fig. 68 indicated that apparent porosity was more or less independent on the water content. A slight increase of porosity of samples containing equal amount of powder as polyol was probably caused by different powder to polyurethane ratio, not by water.

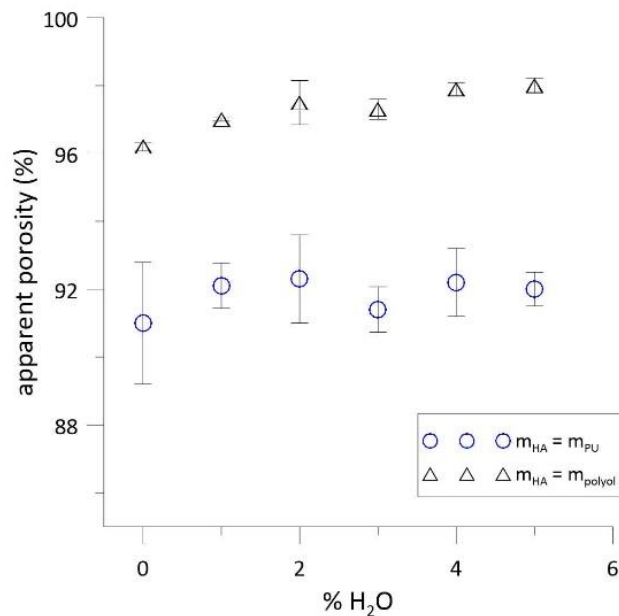


**Fig. 68** Influence of water and powder content on porosity calculated from weight, dimensions and theoretical density of hydroxyapatite

Although the total volume of pores was almost the same, the additive water influenced individual pore sizes and their distribution (see Fig. 69 and Fig. 70). Pore sizes were determined by image analysis of polished cross sections cut 3 mm below the top of PU / HA foam, sintered at  $1050 \text{ }^\circ\text{C}/2\text{h}$ . All pores having diameter larger than  $5 \text{ }\mu\text{m}$  were measured on the area  $25 \text{ mm}^2$  per one sample. Results are summarized in Table 21. Since the pores were measured in 2D, the real (3D) diameters are larger [109]. Assuming that the pores are ideal spheres and according to the probability of cutting a sphere in different distances far from the largest diameter, the average pore diameters can be simply multiplied by a constant 1.57. This approach is not statistically completely right, detailed explanation of sphere unfolding and particle size distribution in 3D from 2D data can be found elsewhere [163-165].

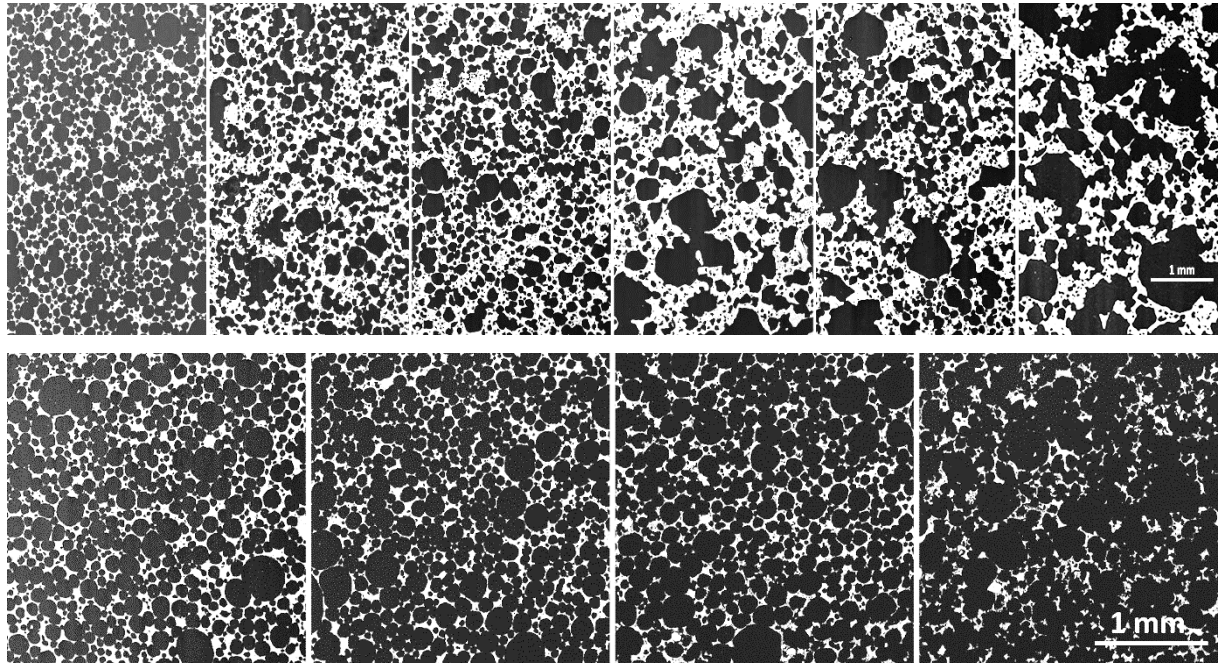


**Fig. 69** Overview of cross sections of ceramic scaffolds sintered at 1050 °C: top row:  $m_{HA} = m_{polyurethane}$ , from 0 (left) to 5 pphp (right); bottom row:  $m_{HA} = m_{polyol}$ , from 0 (left) to 3 pphp (right)

As is obvious from Fig. 70, the pore size distribution (in 2D) was skewed right, the number of small pores was several times higher than the large ones. For differentiation of the influence of large and small pores which highly probably were not all slices of larger ones, an average size of 10% of the highest measured values was also calculated (see Table 21). It appeared that all of these large pores were interconnected and they formed the greater part of the surface area and they could be suitable for cell colonization.

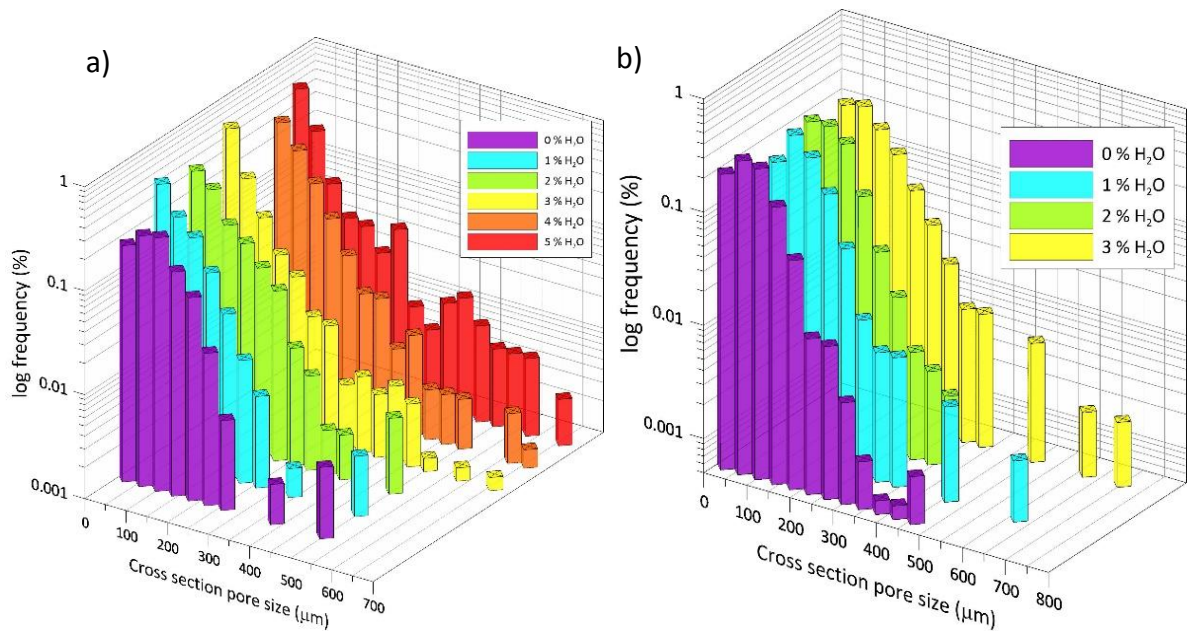


**Fig. 70** Histograms of measured pore sizes: (a)  $m_{HA} = m_{polyurethane}$ ; (b)  $m_{HA} = m_{polyol}$

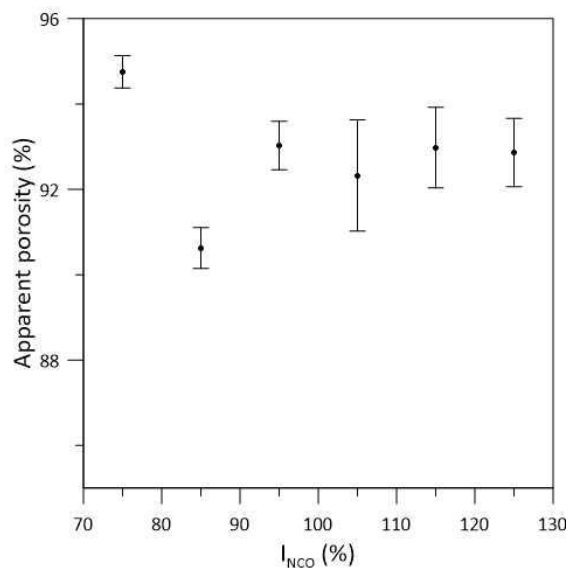
**Table 21** Pore sizes estimated from cross section of scaffolds sintered at 1050 °C/2 h

HA/PU H <sub>2</sub> O (wt. % of polyol)	1 0	1 1	1 2	1 3	1 4	1 5	0.62 0	0.56 1	0.51 2	0.47 3
Porosity (image analysis)	78.8	61.0	64.8	59.7	60.6	67.2	81.7	84.7	85.9	88.4
Standard deviation (%)	0.5	2.3	2.6	1.2	2.9	2.9	0.6	0.7	0.3	1.3
Average pore size (μm)	94	65	79	65	86	93	86	125	109	124
Standard deviation (μm)	59	57	71	89	107	134	54	59	59	82
Avg pore size · 1.27 (μm)	120	83	100	83	110	118	110	159	139	158
10% largest pores (μm)	209	184	223	271	326	423	200	245	228	301
St. deviation 10% (μm)	59	61	79	144	157	169	57	77	47	99
Avg pores 10% · 1.27 (μm)	266	234	284	345	415	539	255	312	290	383

### ***Effect of isocyanate index***

According to the literature search [166-168], the isocyanate index  $I_{NCO}$  of rigid polyurethane foams should varied between 105 and 125. To ensure the complete reaction of all the OH groups, the isocyanate index  $I_{NCO}$  was preferentially set to 105. If  $I_{NCO}$  was below 100 some of OH groups did not react and excess of polyol made a final foam soft and easily cut. And vice versa, higher  $I_{NCO}$  led to more rigid foams because the excess of diisocyanate caused the cross-linking of the polymer chains [168].

Fig. 71 demonstrated that apparent porosity was not significantly influenced by an isocyanate index except of the lowest value of  $I_{NCO} = 75$ . Volume of this blown polyurethane foam sample was almost doubled against the others. However, what was strongly influenced by  $I_{NCO}$  was the ease of manufacturing and shaping after the curing. Composites having high  $I_{NCO}$  exhibited higher viscosity of mixture during processing due to low polyol / powder ratio. In Fig. 72, there is a demonstration how easily foam can be cut into required shapes. The idea was to prepare 1.2cm high cylinders. It was achieved only with the lowest indexes ( $I_{NCO} = 75$  and 85); whereas the rigid composites behave very brittle and shaping after the curing was almost impossible.

**Fig. 71** The dependence of isocyanate index on apparent porosity

The easiness of shaping after the foam hardening (or isocyanate index) had a crucial influence on structure and behaviour of foams after the sintering. Examples of foams sintered at 1050 °C/ 2 h are in Fig. 73. Foams with a regular shape and low  $I_{NCO}$  were strong even while maintaining high porosity (above 90%). The foam with the highest  $I_{NCO} = 125$  sintered at 1050 °C did not exhibited even the handling strength. This might have been due to the defects created during shaping or because of inhomogeneous internal structure caused by difficult mixing of reactants. As is evident from micrographs in Fig. 74, microstructure was influenced by isocyanate index; lower index led to smooth defect-free surface.

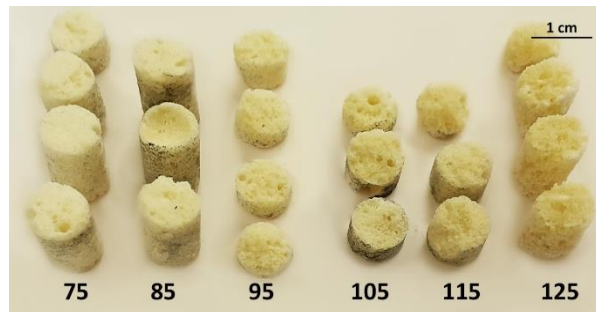


**Fig. 72** An overview of prepared composites with different isocyanate index



**Fig. 73** Ceramic foams with different isocyanate index after heat treatment at 1050 °C/2h

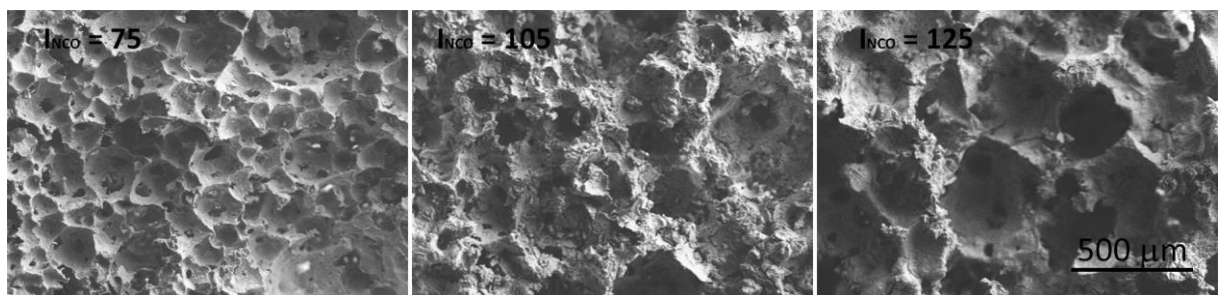


**Fig. 74** Microstructures of scaffolds with different isocyanate indexes ( $I_{NCO} = 75, 105, 125$ )

HA/PU = 100 %, 2 % H<sub>2</sub>O, sintered at 1350 °C/2 h

#### ***Effect of CaP / polyurethane ratio***

The capability of the composite to blow and achieve a specific volume was mainly influenced by the properties of the polyurethane binder. The higher powder / polymer ratio, the worse processability of the composite and the lower final volume were observed. Nonetheless, the significant difference in structure and porosity was apparent after the burning out of organic components. Fig. 63 and Fig. 75 indicated that the CaP / PU ratio had the highest influence on apparent porosity and because strength is proportional to it, HA / PU ratio was probably the most important parameters of all tested ones.

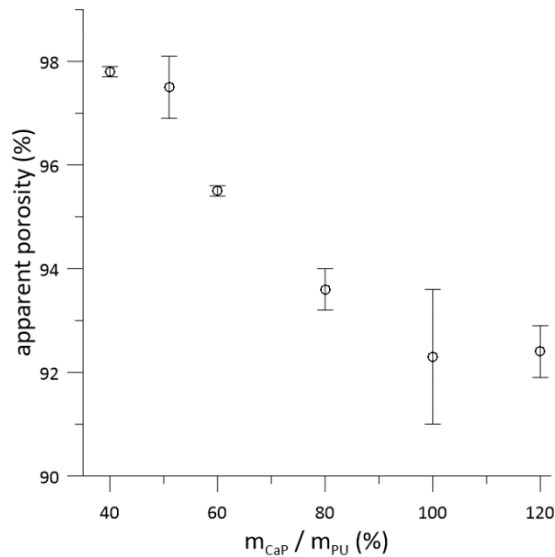


**Fig. 75** Effect of HA / PU ratio on apparent porosity ( $I_{NCO} = 105$ ; 2%  $H_2O$ )

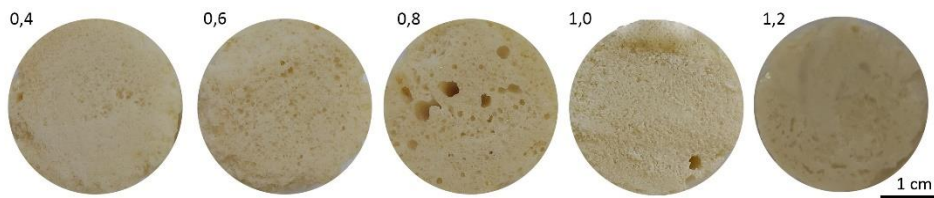


**Fig. 76** Structure of prepared composites with different HA / PU ratio (2%  $H_2O$ ,  $I_{NCO} = 105$ )

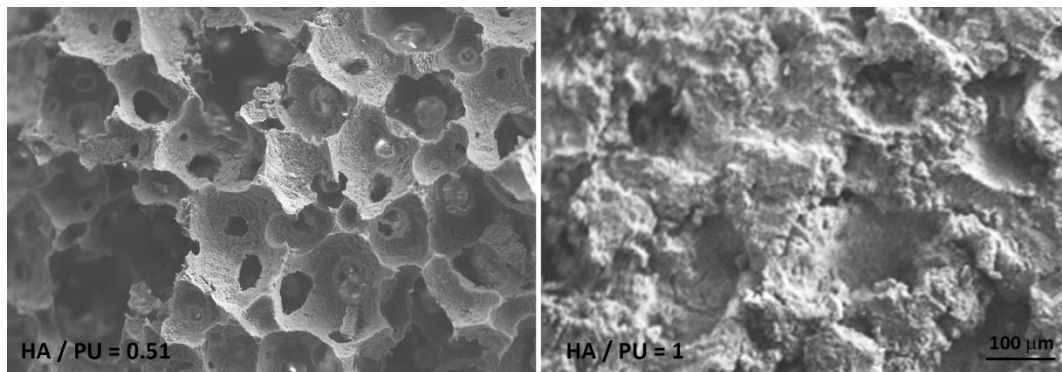


**Fig. 77** Microstructure of ceramic scaffolds at different HA/PU ratio: 0.51 on the left and 1 on the right (2%  $H_2O$ ,  $I_{NCO} = 105$ , 1200 °C/2h)

Ceramic foams having constant HA/polyol ratio exhibited very high porosity resulted in poor mechanical properties (even insufficient handling strength). All samples which had ha/pu ratio below 0.6 and simultaneously contained 4 or 5 pphp of water were destroyed in the furnace during the burnout of the polymer (see Fig. 78). This could have been due to the fact that the proportion of powder (calculated porosity exceeding 97.5 %) was so small that the individual ceramic particles have not been in contact to each other and adjacent polymer layer was too thick to enable compacting of green ceramic body by diffusion.



**Fig. 78** Overview of scaffolds containing 4% H<sub>2</sub>O: (a) ha/pu = 0.4, (b) ha/pu = 0.6, (c) ha/pu = 0.8

It seems that the ideal defect-free scaffolds with interconnected pores suitable for application in bone tissue engineering should have ha / pu ratio lower than 1 (see Fig. 77).

#### ***Effect of sintering temperature***

As already indicated in Table 20, the apparent porosity and pore sizes decreased with an increasing sintering temperature. The linear shrinkage of ceramics having HA / PU ratio = 1 was  $15 \pm 1 \%$  at 1050 °C,  $22.7 \pm 1.3 \%$  at 1200 °C and  $24.2 \pm 1.3 \%$  at 1350 °C. For ceramics having HA / polyol ratio = 1, the linear shrinkage was depended on HA / PU ratio. Generally, the shrinkage increased with the increasing porosity. For scaffolds with HA / PU < 1, it reached almost 20 % at 1050 °C and about 30 % at 1200 and 1350 °C. The differences in macrostructure (see Fig. 79) are negligible due to wide distribution of pore sizes.

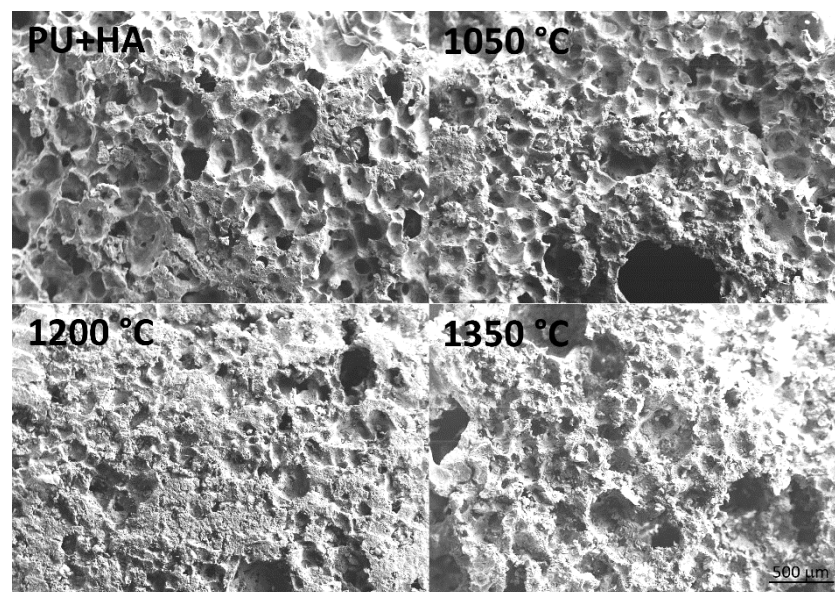


**Fig. 79** Micrographs of HA100\_2\_105 scaffold sintered at different temperatures: (a) HA/PU composite before calcination; (b) scaffold sintered at 1050 °C; (c) 1200 °C; (d) 1350 °C (the magnification is the same for all 4 photos).

Besides changes of phase composition which were described thoroughly in chapters 5.5.1 and 5.5.2, the microstructure was dramatically changed by the sintering temperature. PU/HA composite had very smooth surface as is evident from left quarter of Fig. 80 (PU+HA), the rough middle part of the same photo is a fracture area where the relief was caused by pulling out of ceramic particles. With an increasing temperature, the grains significantly coarsened and microporosity was reduced.



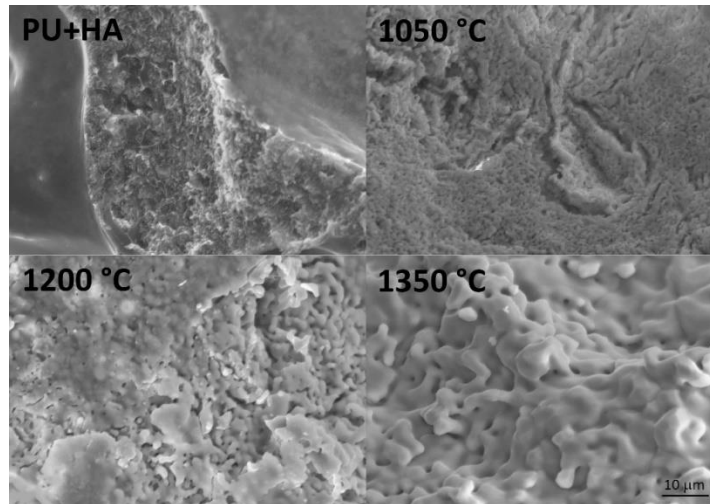


**Fig. 80** Microstructures of HA100\_2\_105 scaffold sintered at different temperatures: (a) HA/PU composite before calcination; (b) scaffold sintered at 1050 °C; (c) 1200 °C; (d) 1350 °C (the magnification is the same for all 4 photos).

### 5.5.4 Mechanical properties

The compressive strength of tested samples varied between 0.2 and 0.3 MPa. Hence, the strength was similar to strength of hydroxyapatite foams prepared by polymer replica technique. This value was not so bad for samples reaching almost 90% porosity. Scaffolds with the same porosity did not exhibit neither handling strength in the case of replica method. The preparation process of the tested specimens however was not ideal. Cylinders were shaped after the hardening of the composite. This could lead to generation of defects in the macrostructure which could consequently negatively influenced the measured values. The compressive strength could be enhanced by direct casting of mixture to the form of optimal geometry, such as cylinders with height to diameter ratio equal to 1.5.

Concerning fracture mechanism, the shapes of loading curves (in Fig. 81) show almost the same stress during loading – it indicates that struts were destroyed one by one. Two samples, represented by blue and red loading curves, were loaded until they were completely crushed to powder. This mechanism is called densification.

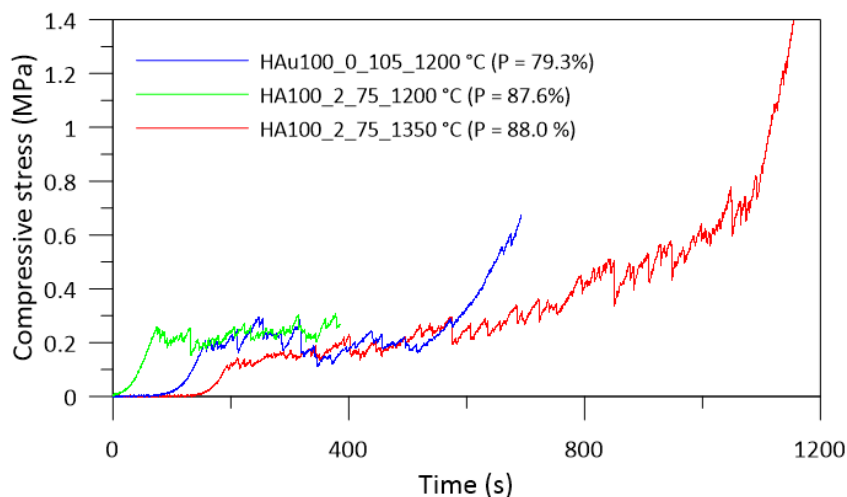


**Fig. 81** Compressive stress dependence on time of loading

### 5.5.5 Summary of Chapter 5.5

Porous calcium phosphate scaffolds were successfully prepared by polymerization in situ using diisocyanate, polyol and water. Generation of carbon dioxide led to formation of large interconnected pores. The total porosity of scaffolds decreased from 99 to 76% as the powder content increased, leading to denser and thicker pore walls between interconnected pores. On the other hand, the total porosity was almost independent on percentage of added water (up to 5 pphp, parts per hundred parts of polyol). However, water influenced pore size. Average pore size increased from 65  $\mu\text{m}$  (1 pphp) to 93  $\mu\text{m}$  (5 pphp). Sizes of 10 % of largest pores suitable for cell colonization were enlarged from 234  $\mu\text{m}$  to 539  $\mu\text{m}$  just due to water addition. Because the scaffolds are formed by in situ polymerization, the shape of scaffold can be easily controlled by the shape of mould. The porosity and pore size is tuneable just by powder / polyol / diisocyanate / water ratio.

## 6 CONCLUSIONS

Open three-dimensional ceramic scaffolds with interconnected macropores were prepared by polymer replica technique or by polymerization in situ. Ceramic scaffolds were obtained in both cases after burning out the polyurethane and other binders from the structure. Regarding the replica technique, the morphology of scaffolds mimicked the morphology of commercial reticulated polyurethane templates. Cell size and its distribution was controlled by used template. The total porosity was tailored by viscosity of suspension and by number of applied layers.

The first studied system was based on alumina. Open-cell alumina foams were prepared by replica method from nanosized boehmite powder and fused microsized alumina. Highly porous reticulated alumina foams exhibited low compressive strength ( $< 0.25$  MPa) because of high total porosity ( $> 95\%$ ), low microstructure density ( $\sim 50\%$ ) and because of voids inside the struts generated during polyurethane burnout. The strength was at least doubled due to scaffold infiltration by nanosized boehmite, although the struts remained partially unfilled. The successful approach was strut filling by suspension composed of finer alumina particles having allowed about fourfold increase of strength. Mechanical properties were improved, however, material was biologically inert. To shift biological properties to bioactive behaviour, the foams were coated by hydroxyapatite suspension. All components, namely porous core, reinforcing phase (/layer) and bioactive coating, seemed to firmly adhere to each other. For application in bone tissue engineering it would be necessary to reduce pore sizes to maximally  $500\ \mu\text{m}$  and simultaneously improved the compressive strength, e.g. by decreasing total porosity below  $85\%$ .

The second research area dealt with alumina toughened zirconia scaffolds. Macroporous scaffolds with interconnected pores of size ranging from  $350$  to  $1200\ \mu\text{m}$  were prepared by similar way as previously described foams. The difference was that yttria stabilized zirconia was used instead of fused alumina. Based on results of the mechanical testing,  $5$  wt. % content of alumina was chosen as optimum for further experiments. Scaffolds of various total porosity ( $57\text{--}98\%$ ) were fabricated by multiple coating process (up to  $6$  cycles). The bioactive behaviour of the composite was achieved by coating of calcium phosphates. Besides bioactivity and cytotoxicity tests, the cell colonization in 3D scaffold was evaluated. It was shown that MG-63 cells grew through the scaffold with  $1000\ \mu\text{m}$  large pores after three-day cultivation, the same amount of cells was found both adhered to the outer and inner struts of scaffold.

The main disadvantage of these two types of scaffolds was the bioinert core. The current trend of tissue engineering are resorbable materials that help bones to regenerate instead of formerly used permanent replacements, so the attention was focused on calcium phosphate scaffolds.

Calcium phosphate 3D interconnected scaffolds with different pore sizes were fabricated with and without silica addition. Pore dimensions ranging between  $375$  and  $1150\ \mu\text{m}$  were depended on the pore size of four templates which were replicated. The average window size between two interconnected pores was from  $118$  to  $536\ \mu\text{m}$ , ideal for cell penetration.

Addition of silica (5– 20 wt. %) strongly influenced the phase transformation of hydroxyapatite to  $\beta$ -TCP and  $\alpha$ -TCP, respectively. The ratio of  $\alpha$ -TCP to  $\beta$ -TCP increased fivefold with increasing silica content. Lattice parameters indicated that TCP was substituted by silicate ions. However, almost all amorphous silica was transformed to the cristobalite crystalline phase. Addition of cristobalite did not negatively influenced the biological properties. Testing in direct contact assay with MG63 cells showed that percentage of covered surface slightly increased with increasing silica content. After three days of cultivation, the surfaces were totally covered by newly formed apatite layer which indicates excellent bioactive behaviour. The cell viability increased with addition of silica; it seemed that silica supported cell adhesion. This trend was followed for the three pore sizes, with the maximum effect noted for the scaffolds using 90 ppi polymer pore size. The main enhancement was, nevertheless, observed on mechanical properties. The compressive strength of calcium phosphate scaffold bonded by polyvinylalcohol was 0.3 MPa at 80% porosity. The strength of silica reinforced calcium phosphates scaffolds exceeded 20 MPa.

From previous paragraph is obvious that preparation of calcium phosphate scaffolds by replica technique was from mechanical point of view less successful. For this reason a novel processing technique was developed to overcome the low strength caused by internal defects and hollow struts. Porous calcium phosphate scaffolds were successfully prepared by polymerization in situ using diisocyanate, polyol and water. Generation of carbon dioxide led to formation of large interconnected pores. Pores smaller than 5  $\mu\text{m}$  were created by polymeric binder burnout during sintering. This small interconnected pores can be convenient for supply of nutrients and oxygen. The total porosity of scaffolds decreased from 99 to 76% as the powder content increased, leading to denser and thicker pore walls between interconnected pores. On the other hand, the total porosity was almost independent on amount of added water (up to 5 pphp, parts per hundred parts of polyol). However, water influenced pore size. Average pore size increased from 65  $\mu\text{m}$  (1 pphp) to 93  $\mu\text{m}$  (5 pphp). Sizes of 10 % of larges pores suitable for cell colonization were enlarged from 234  $\mu\text{m}$  to 539  $\mu\text{m}$  just due to water addition. Because the scaffolds are formed by in situ polymerization, the shape of scaffold can be easily controlled by the shape of mould. The porosity and pore size is tuneable just by powder / polyol / diisocanate / water ratio. On the basis of morphological observations, the calcium phosphate scaffolds could be promising adepts for synthetic bone grafts.

The aim of this thesis, to fabricate three-dimensional scaffolds that can be potentially used in bone tissue engineering, was achieved. Neither of the studied materials was cytotoxic and moreover all prepared composites behave bioactive in simulated body fluid. The most promising adept for application in bone tissue engineering seems to be composite material containing calcium phosphates reinforced by silica.

## 7 REFERENCES

- [1] LUNENFELD, B., STRATTON, P. The clinical consequences of an ageing world and preventive strategies, *Best Practice & Research Clinical Obstetrics & Gynaecology*, 2013, vol. 27, pp. 643.
- [2] LICHTER, P., PAPE, H. C., PUFER, T., KOBBE, P., FISCHER, H. Scaffolds for bone healing: Concepts, materials and evidence, *Injury*, 2011, vol. 42, pp. 569.
- [3] BOHNER, M. Resorbable biomaterials as bone graft substitutes, *Materials Today*, 2010, vol. 13, pp. 24.
- [4] DE LONGJR, W. G., EINHORN, T. A., KOVAL, K., MCKEE, M., SMITH, W., SANDERS, R., WATSON, T. Bone Grafts and Bone Graft Substitutes in Orthopaedic Trauma Surgery A Critical Analysis, *The Journal of Bone & Joint Surgery*, 2007, vol. 89, pp. 649.
- [5] WOJNAR, R. Bone and Cartilage – its Structure and Physical Properties In *Biomechanics of Hard Tissues*; Wiley-VCH Verlag GmbH & Co. KGaA: 2010, pp 75.
- [6] SHARIR, A., BARAK, M. M., SHAHAR, R. Whole bone mechanics and mechanical testing, *The Veterinary Journal*, 2008, vol. 177, pp. 8.
- [7] VAUGHAN, T. J., MCCARTHY, C. T., MCNAMARA, L. M. A three-scale finite element investigation into the effects of tissue mineralisation and lamellar organisation in human cortical and trabecular bone, *Journal of the Mechanical Behavior of Biomedical Materials*, 2012, vol. 12, pp. 50.
- [8] CLARKE, B. Normal Bone Anatomy and Physiology, *Clinical Journal of the American Society of Nephrology*, 2008, vol. 3, pp. S131.
- [9] RUBIN, M. A., JASIUK, I. The TEM characterization of the lamellar structure of osteoporotic human trabecular bone, *Micron*, 2005, vol. 36, pp. 653.
- [10] RHO, J.-Y., KUHN-SPEARING, L., ZIOUPOS, P. Mechanical properties and the hierarchical structure of bone, *Medical Engineering & Physics*, 1998, vol. 20, pp. 92.
- [11] WEINER, S., WAGNER, H. D. The material bone: Structure-Mechanical Function Relations, *Annual Review of Materials Science*, 1998, vol. 28, pp. 271.
- [12] RITCHIE, R. O. The conflicts between strength and toughness, *Nature Materials*, 2011, vol. 10, pp. 817.
- [13] BBML *General Introduction to Bone: Collagen and Mineral* <http://www.iupui.edu/~bbml/boneintro.shtml>.
- [14] REY, C., COMBES, C., DROUET, C., GLIMCHER, M. J. Bone mineral: update on chemical composition and structure, *Osteoporosis International*, 2009, vol. 20, pp. 1013.
- [15] MA, P. X., ELISSEEFF, J. *Scaffolding In Tissue Engineering*; Taylor & Francis, 2005.
- [16] UDDIN, M. H., MATSUMOTO, T., OKAZAKI, M., NAKAHIRA, A., SOHMURA, T. Biomimetic Fabrication of Apatite Related Biomaterials, *Biomimetics Learning from Nature 2010.*, pp. 63.
- [17] WOPENKA, B., PASTERIS, J. D. A mineralogical perspective on the apatite in bone, *Materials Science and Engineering: C*, 2005, vol. 25, pp. 131.
- [18] YOSHIKAWA, H., MYOUI, A. Bone tissue engineering with porous hydroxyapatite ceramics, *Journal of Artificial Organs*, 2005, vol. 8, pp. 131.
- [19] OLSZTA, M. J., CHENG, X., JEE, S. S., KUMAR, R., KIM, Y.-Y., KAUFMAN, M. J., DOUGLAS, E. P., GOWER, L. B. Bone structure and formation: A new perspective, *Materials Science and Engineering: R: Reports*, 2007, vol. 58, pp. 77.
- [20] HASSENKAM, T., FANTNER, G. E., CUTRONI, J. A., WEAVER, J. C., MORSE, D. E., HANSMA, P. K. High-resolution AFM imaging of intact and fractured trabecular bone, *Bone*, 2004, vol. 35, pp. 4.

- [21] FRATZL, P., WEINKAMER, R. Nature's hierarchical materials, *Progress in Materials Science*, 2007, vol. 52, pp. 1263.
- [22] WEINER, S., TRAUB, W. Bone structure: from angstroms to microns, *The FASEB Journal*, 1992, vol. 6, pp. 879.
- [23] WEINER, S., TRAUB, W., WAGNER, H. D. Lamellar Bone: Structure–Function Relations, *Journal of Structural Biology*, 1999, vol. 126, pp. 241.
- [24] VANPUTTE, C., REGAN, J., RUSSO, A. *Seeley's Essentials of Anatomy and Physiology*; McGraw-Hill Education, 2012, p. 164.
- [25] HAWKINS, D. In *Biomechanics of Musculoskeletal Tissues*; University of California: Davis, 2001, p 13.
- [26] CAMBRIDGE, U. O. *TLP Library Structure of bone and implant materials - Mechanical properties of bone* 2014  
[http://www.doitpoms.ac.uk/tlplib/bones/bone\\_mechanical.php](http://www.doitpoms.ac.uk/tlplib/bones/bone_mechanical.php).
- [27] RAVAGLIOLI, A., KRAJEWSKI, A. *Bioceramics*; Springer Netherlands, 1992, p.78.
- [28] MARCUS, R., FELDMAN, D., DEMPSTER, D. W., LUCKEY, M., CAULEY, J. A. *Osteoporosis: Two-Volume Set*; Elsevier Science, 2013, p. 261.
- [29] REZWAN, K., CHEN, Q. Z., BLAKER, J. J., BOCCACCINI, A. R. Biodegradable and bioactive porous polymer/inorganic composite scaffolds for bone tissue engineering, *Biomaterials*, 2006, vol. 27, pp. 3413.
- [30] RITCHIE, R. O., BUEHLER, M. J., HANSMA, P. Plasticity and toughness in bone, *Physics Today*, 2009, vol. 62, pp. 41.
- [31] BRANDI, M. L. Microarchitecture, the key to bone quality, *Rheumatology*, 2009, vol. 48, pp. iv3.
- [32] RIGGS, B. L., PARFITT, A. M. Drugs Used to Treat Osteoporosis: The Critical Need for a Uniform Nomenclature Based on Their Action on Bone Remodeling, *Journal of Bone and Mineral Research*, 2004, vol. 20, pp. 177.
- [33] BURG, K. J. L., PORTER, S., KELLAM, J. F. Biomaterial developments for bone tissue engineering, *Biomaterials*, 2000, vol. 21, pp. 2347.
- [34] BRANEMARK, R., BRANEMARK, P., RYDEVIK, B., MYERS, R. R. Osseointegration in skeletal reconstruction and rehabilitation: a review, *Journal of rehabilitation research and development*, 2001, vol. 38, pp. 175.
- [35] PNEUMATICOS, S. G., TRIANTAFYLLOPOULOS, G. K., CHATZIOANNOU, S., BASDRA, E. K., PAPAVALASSILOU, A. G. Biomolecular strategies of bone augmentation in spinal surgery, *Trends in Molecular Medicine*, 2011, vol. 17, pp. 215.
- [36] CAO, W., HENCH, L. L. Bioactive materials, *Ceramics International*, 1996, vol. 22, pp. 493.
- [37] WANG, H., LI, Y., ZUO, Y., LI, J., MA, S., CHENG, L. Biocompatibility and osteogenesis of biomimetic nano-hydroxyapatite/polyamide composite scaffolds for bone tissue engineering, *Biomaterials*, 2007, vol. 28, pp. 3338.
- [38] JONES, J. R., HENCH, L. L. Regeneration of trabecular bone using porous ceramics, *Current Opinion in Solid State and Materials Science*, 2003, vol. 7, pp. 301.
- [39] JONES, J. R., BOCCACCINI, A. R. In *Cellular Ceramics*; Wiley-VCH Verlag GmbH & Co. KGaA: 2006, p 547.
- [40] LU, J., FLAUTRE, B., ANSELME, K., HARDOUIN, P., GALLUR, A., DESCAMPS, M., THIERRY, B. Role of interconnections in porous bioceramics on bone recolonization in vitro and in vivo, *Journal of Materials Science: Materials in Medicine*, 1999, vol. 10, pp. 111.

- [41] LIU, Y., LIM, J.,TEOH, S. H. Review: development of clinically relevant scaffolds for vascularised bone tissue engineering, *Biotechnology Advances*, 2013, vol. 31, pp. 688.
- [42] HENCH, L. L. Sol-gel materials for bioceramic applications, *Current Opinion in Solid State and Materials Science*, 1997, vol. 2, pp. 604.
- [43] HUTMACHER, D. W. Scaffolds in tissue engineering bone and cartilage, *Biomaterials*, 2000, vol. 21, pp. 2529.
- [44] BOSE, S., ROY, M.,BANDYOPADHYAY, A. Recent advances in bone tissue engineering scaffolds, *Trends Biotechnol*, 2012, vol. 30, pp. 546.
- [45] KARAGEORGIU, V.,KAPLAN, D. Porosity of 3D biomaterial scaffolds and osteogenesis, *Biomaterials*, 2005, vol. 26, pp. 5474.
- [46] BARRÈRE, F., MAHMOOD, T. A., DE GROOT, K.,VAN BLITTERSWIJK, C. A. Advanced biomaterials for skeletal tissue regeneration: Instructive and smart functions, *Materials Science and Engineering: R: Reports*, 2008, vol. 59, pp. 38.
- [47] STEVENS, M. M. Biomaterials for bone tissue engineering, *Materials Today*, 2008, vol. 11, pp. 18.
- [48] LIU, X.,MA, P. Polymeric Scaffolds for Bone Tissue Engineering, *Annals of Biomedical Engineering*, 2004, vol. 32, pp. 477.
- [49] GUNATILLAKE, P. A.,ADHIKARI, R. Biodegradable synthetic polymers for tissue engineering, *Eur Cell Mater*, 2003, vol. 5, pp. 1.
- [50] DHANDAYUTHAPANI, B., YOSHIDA, Y., MAEKAWA, T.,KUMAR, D. S. Polymeric Scaffolds in Tissue Engineering Application: A Review, *International Journal of Polymer Science*, 2011, vol. 2011, pp. 1.
- [51] CHEN, Q., ZHU, C.,THOUAS, G. Progress and challenges in biomaterials used for bone tissue engineering: bioactive glasses and elastomeric composites, *Progress in Biomaterials*, 2012, vol. 1, pp. 1.
- [52] CARTER, C. B.,NORTON, G. *Ceramic Materials: Science and Engineering*; Springer, 2007.
- [53] PICONI, C.,MACCAURO, G. Zirconia as a ceramic biomaterial, *Biomaterials*, 1999, vol. 20, pp. 1.
- [54] HENCH, L. L., SPLINTER, R. J., ALLEN, W. C.,GREENLEE, T. K. Bonding mechanisms at the interface of ceramic prosthetic materials, *Journal of Biomedical Materials Research*, 1971, vol. 5, pp. 117.
- [55] JONES, J. R. Review of bioactive glass: from Hench to hybrids, *Acta Biomater*, 2013, vol. 9, pp. 4457.
- [56] TRECCANI, L., KLEIN, T. Y., MEDER, F., PARDUN, K.,REZWAN, K. Functionalized ceramics for biomedical, biotechnological and environmental applications, *Acta biomaterialia*, 2013, vol. 9, pp. 7115.
- [57] NIKOM, J., CHAROONPATRAPONG-PANYAYONG, K., KEDJARUNE-LEGGAT, U., STEVENS, R., KOSACHAN, N.,JAROENWORALUCK, A. 3D interconnected porous HA scaffolds with SiO<sub>2</sub> additions: effect of SiO<sub>2</sub> content and macropore size on the viability of human osteoblast cells, *J Biomed Mater Res A*, 2013, vol. 101, pp. 2295.
- [58] ZOCCA, A., ELSAYED, H., BERNARDO, E., GOMES, C. M., LOPEZ-HEREDIA, M. A., KNABE, C., COLOMBO, P.,GUNSTER, J. 3D-printed silicate porous bioceramics using a non-sacrificial preceramic polymer binder, *Biofabrication*, 2015, vol. 7, pp. 025008.
- [59] ZHANG, F., CHANG, J., LIN, K.,LU, J. Preparation, mechanical properties and in vitro degradability of wollastonite/tricalcium phosphate macroporous scaffolds from nanocomposite powders, *Journal of Material Science Materials in Medicine*, 2008, vol. 19, pp. 167.

- [60] MESEGUER-OLMO, L., BERNABEU-ESCAPLEZ, A., VALLET-REGÍ, M., AZNAR-CERVANTES, S., VICENTE-ORTEGA, V., ALCARAZ-BAÑOS, M., CLAVEL-SAINZ, M., HERRERA-RODRÍGUEZ, A., LOPEZ-PRATS, F., MORALEDA-JIMÉNEZ, J. M., MESEGUER-ORTIZ, C. L. Bone tissue engineering. Design and development of biologically active vitroc ceramic-based hybrid materials to be used as bone substitutes, *Revista Española de Cirugía Ortopédica y Traumatología (English Edition)*, 2010, vol. 54, pp. 59.
- [61] PIMENTA, L., PESÁNTEZ, C. F. A., OLIVEIRA, L. Silicon matrix calcium phosphate as a bone substitute: early clinical and radiological results in a prospective study with 12-month follow-up, *SAS journal*, 2008, vol. 2, pp. 62.
- [62] RADIN, S., EL-BASSYOUNI, G., VRESILOVIC, E. J., SCHEPERS, E., DUCHEYNE, P. In vivo tissue response to resorbable silica xerogels as controlled-release materials, *Biomaterials*, 2005, vol. 26, pp. 1043.
- [63] LU, J., LIONG, M., LI, Z., ZINK, J. I., TAMANOI, F. Biocompatibility, Biodistribution, and Drug-Delivery Efficiency of Mesoporous Silica Nanoparticles for Cancer Therapy in Animals, *Small*, 2010, vol. 6, pp. 1794.
- [64] PEER, D., KARP, J. M., HONG, S., FAROKHZAD, O. C., MARGALIT, R., LANGER, R. Nanocarriers as an emerging platform for cancer therapy, *Nature nanotechnology*, 2007, vol. 2, pp. 751.
- [65] GARY-BOBO, M., HOCINE, O., BREVET, D., MAYNADIER, M., RAEHM, L., RICHETER, S., CHARASSON, V., LOOCK, B., MORÈRE, A., MAILLARD, P. Cancer therapy improvement with mesoporous silica nanoparticles combining targeting, drug delivery and PDT, *International journal of pharmaceutics*, 2012, vol. 423, pp. 509.
- [66] THERON, C., GALLUD, A., GIRET, S., MAYNADIER, M., GREGOIRE, D., PUCHE, P., JACQUET, E., POP, G., SGARBURA, O., BELLET, V., HIBNER, U., ZINK, J. I., GARCIA, M., WONG CHI MAN, M., CARCEL, C., GARY-BOBO, M. pH-operated hybrid silica nanoparticles with multiple H-bond stoppers for colon cancer therapy, *RSC Advances*, 2015, vol. 5, pp. 64932.
- [67] HENCH, L. Bioactive ceramics: theory and clinical applications, *Bioceramics*, 1994, vol. 7, pp. 3.
- [68] HENCH, L. The story of Bioglass®, *Journal of Materials Science: Materials in Medicine*, 2006, vol. 17, pp. 967.
- [69] HENCH, L. L. Chronology of Bioactive Glass Development and Clinical Applications, *New Journal of Glass and Ceramics*, 2013, vol. 03, pp. 67.
- [70] TILOCCA, A. Models of structure, dynamics and reactivity of bioglasses: a review, *Journal of Materials Chemistry*, 2010, vol. 20, pp. 6848.
- [71] GERHARDT, L.-C., BOCCACCINI, A. R. Bioactive glass and glass-ceramic scaffolds for bone tissue engineering, *Materials*, 2010, vol. 3, pp. 3867.
- [72] MOYA, A., AZA, P. N. D., PENA CASTRO, M. D. P., AZA PENDAS, S. D. Bioactive glasses and glass-ceramics, *Boletín de la Sociedad Española de Cerámica y Vidrio*, 2007, vol. 46, pp. 45.
- [73] PARK, J. *Bioceramics: Properties, Characterizations, and Applications*; Springer, 2009.
- [74] CHEVALIER, J., GREMILLARD, L. Ceramics for medical applications: A picture for the next 20 years, *Journal of the European Ceramic Society*, 2009, vol. 29, pp. 1245.
- [75] WILL, J., MELCHER, R., TREUL, C., TRAVITZKY, N., KNESER, U., POLYKANDRIOTIS, E., HORCH, R., GREIL, P. Porous ceramic bone scaffolds for vascularized bone tissue regeneration, *Journal of Materials Science: Materials in Medicine*, 2008, vol. 19, pp. 2781.



- [76] CARRODEGUAS, R. G., DE AZA, S.  $\alpha$ -Tricalcium phosphate: Synthesis, properties and biomedical applications, *Acta Biomaterialia*, 2011, vol. 7, pp. 3536.
- [77] ALLISON, D. C., LINDBERG, A. W., SAMIMI, B., MIRZAYAN, R., MENENDEZ, L. R. A comparison of mineral bone graft substitutes for bone defects, 2011, vol.7, pp 38.
- [78] SAYER, M., STRATILATOV, A. D., REID, J., CALDERIN, L., STOTT, M. J., YIN, X., MACKENZIE, M., SMITH, T. J. N., HENDRY, J. A., LANGSTAFF, S. D. Structure and composition of silicon-stabilized tricalcium phosphate, *Biomaterials*, 2003, vol. 24, pp. 369.
- [79] JOHNSON, J. R., TAVAKLEY, A. Composite scaffold structure, Google Patents: 2009.
- [80] ZAIDMAN, N., BOSNAKOVSKI, D. Advancing with Ceramic Biocomposites for Bone Graft Implants, *Recent Patents on Regenerative Medicine*, 2012, vol. 2, pp 23.
- [81] ZHANG, R., MA, P. X. Porous poly (L-lactic acid)/apatite composites created by biomimetic process, 1999, vol.4, pp. 78.
- [82] ZHANG, Y., REGEROS, R., KIM, J. Bioactive graded zirconia-based structures; Google Patents: 2009.
- [83] KIM, H.-W., LEE, S.-Y., BAE, C.-J., NOH, Y.-J., KIM, H.-E., KIM, H.-M., KO, J. S. Porous ZrO<sub>2</sub> bone scaffold coated with hydroxyapatite with fluorapatite intermediate layer, *Biomaterials*, 2003, vol. 24, pp. 3277.
- [84] KIM, H.-W., KIM, H.-E., KNOWLES, J. C. Hard-tissue-engineered zirconia porous scaffolds with hydroxyapatite sol-gel and slurry coatings, *Journal of Biomedical Materials Research Part B: Applied Biomaterials*, 2004, vol. 70B, pp. 270.
- [85] MIAO, X., HU, Y., LIU, J., HUANG, X. Hydroxyapatite coating on porous zirconia, *Materials Science and Engineering: C*, 2007, vol. 27, pp. 257.
- [86] COLOMBO, P. Conventional and novel processing methods for cellular ceramics, *Philosophical Transactions of the Royal Society A: Mathematical, Physical and Engineering Sciences*, 2006, vol. 364, pp. 109.
- [87] SCHEFFLER, M., COLOMBO, P. *Cellular ceramics: structure, manufacturing, properties and applications*; John Wiley & Sons, 2006.
- [88] OHJI, T., FUKUSHIMA, M. Macro-porous ceramics: processing and properties, *International Materials Reviews*, 2012, vol. 57, pp. 115.
- [89] STUART, A. R., GONZENBACH, U. T., TERVOORT, E., GAUCKLER, L. J. Processing Routes to Macroporous Ceramics: A Review, *Journal of the American Ceramic Society*, 2006, vol. 89, pp. 1771.
- [90] JEAN, G., SCIAMANNA, V., DEMUYNCK, M., CAMBIER, F., GONON, M. Macroporous ceramics: Novel route using partial sintering of alumina-powder agglomerates obtained by spray-drying, *Ceramics International*, 2014, vol.4, pp. 63.
- [91] ANDRADE, J., CAMILLI, J., KAWACHI, E., BERTRAN, C. Behavior of dense and porous hydroxyapatite implants and tissue response in rat femoral defects, *Journal of biomedical materials research*, 2002, vol. 62, pp. 30.
- [92] RITZOULIS, C., SCOUTARIS, N., PAPADEMETRIOU, K., STAVROULIAS, S., PANAYIOTOU, C. Milk protein-based emulsion gels for bone tissue engineering, *Food Hydrocolloids*, 2005, vol. 19, pp. 575.
- [93] DESCAMPS, M., DUHOO, T., MONCHAU, F., LU, J., HARDOUIN, P., HORNEZ, J. C., LERICHE, A. Manufacture of macroporous  $\beta$ -tricalcium phosphate bioceramics, *Journal of the European Ceramic Society*, 2008, vol. 28, pp. 149.

- [94] DESCAMPS, M., RICHART, O., HARDOUIN, P., HORNEZ, J. C., LERICHE, A. Synthesis of macroporous  $\beta$ -tricalcium phosphate with controlled porous architectural, *Ceramics International*, 2008, vol. 34, pp. 1131.
- [95] DEVILLE, S., SAIZ, E., TOMSIA, A. P. Freeze casting of hydroxyapatite scaffolds for bone tissue engineering, *Biomaterials*, 2006, vol. 27, pp. 5480.
- [96] MACCHETTA, A., TURNER, I. G., BOWEN, C. R. Fabrication of HA/TCP scaffolds with a graded and porous structure using a camphene-based freeze-casting method, *Acta Biomaterialia*, 2009, vol. 5, pp. 1319.
- [97] DEVILLE, S. Freeze-Casting of Porous Biomaterials: Structure, Properties and Opportunities, *Materials*, 2010, vol. 3, pp. 1913.
- [98] PU, X., LIU, X., QIU, F., HUANG, L. Novel Method To Optimize the Structure of Reticulated Porous Ceramics, *Journal of the American Ceramic Society*, 2004, vol. 87, pp. 1392.
- [99] VOGT, U. F., GORBAR, M., DIMOPOULOS-EGGENSCHWILER, P., BROENSTRUP, A., WAGNER, G., COLOMBO, P. Improving the properties of ceramic foams by a vacuum infiltration process, *Journal of the European Ceramic Society*, 2010, vol. 30, pp. 3005.
- [100] VITALE-BROVARONE, C., VERNÉ, E., ROBIGLIO, L., APPENDINO, P., BASSI, F., MARTINASSO, G., MUZIO, G., CANUTO, R. Development of glass–ceramic scaffolds for bone tissue engineering: Characterisation, proliferation of human osteoblasts and nodule formation, *Acta Biomaterialia*, 2007, vol. 3, pp. 199.
- [101] CAO, J., RAMBO, C. R., SIEBER, H. Preparation of Porous Al<sub>2</sub>O<sub>3</sub>-Ceramics by Biotemplating of Wood, *Journal of Porous Materials*, 2004, vol. 11, pp. 163.
- [102] OTA, T., EITSUKA, T., YOSHIDA, H., ADACHI, N. Porous Apatite Ceramics Derived from Woods, *Advanced Materials Research*, 2006, vol. 11-12, pp. 247.
- [103] BARG, S., SOLTSMANN, C., ANDRADE, M., KOCH, D., GRATHWOHL, G. Cellular Ceramics by Direct Foaming of Emulsified Ceramic Powder Suspensions, *Journal of the American Ceramic Society*, 2008, vol. 91, pp. 2823.
- [104] SALVINI, V. R., SANDURKOV, B. A., GUNNEWIEK, F., ROSA, D. S., PANDOLFELLI, V. C. Porous ceramics with tailored properties, *American Ceramic Society Bulletin*, 2007, vol. 86, pp.
- [105] TRUNEC, M., MACA, K. In *Advanced Ceramics for Dentistry*; SHEN, J. Z., KOSMAČ, T., Eds.; Butterworth-Heinemann: Oxford, 2014, p 123.
- [106] THAVORNYUTIKARN, B., CHANTARAPANICH, N., SITTHISERIPRATIP, K., THOUAS, G. A., CHEN, Q. Bone tissue engineering scaffolding: computer-aided scaffolding techniques, *Progress in Biomaterials*, 2014, vol. 3, pp. 61.
- [107] FIELDING, G. A., BANDYOPADHYAY, A., BOSE, S. Effects of silica and zinc oxide doping on mechanical and biological properties of 3D printed tricalcium phosphate tissue engineering scaffolds, *Dental Materials*, 2012, vol. 28, pp. 113.
- [108] STAFF, B. S. I. *Advanced Technical Ceramics. Monolithic Ceramics. General and Textural Properties. Determination of Density and Porosity*; B S I Standards, 1993, p 65.
- [109] LOCK, P. A., JING, X. D., ZIMMERMAN, R. W., SCHLUETER, E. M. Predicting the permeability of sandstone from image analysis of pore structure, *Journal of applied physics*, 2002, vol. 92, pp. 6311.
- [110] KOKUBO, T., TAKADAMA, H. How useful is SBF in predicting in vivo bone bioactivity?, *Biomaterials*, 2006, vol. 27, pp. 2907.
- [111] BOHNER, M., LEMAITRE, J. Can bioactivity be tested in vitro with SBF solution?, *Biomaterials*, 2009, vol. 30, pp. 2175.

- [112] FRANCO, R., NGUYEN, T., LEE, B.-T. Preparation and characterization of electrospun PCL/PLGA membranes and chitosan/gelatin hydrogels for skin bioengineering applications, *Journal of Materials Science: Materials in Medicine*, 2011, vol. 22, pp. 2207.
- [113] HOMOLKOVA, M., CISAR, P., SOUKUP, J., V., B. Innovative test of non transparent material cytotoxicity, *23rd International Conference on Metallurgy and Materials METAL 2014, Brno, Czech Republic, 21-23 May 2014*, 2014, vol., pp. 1109.
- [114] LEE, J. T., LENG, Y., CHOW, K. L., REN, F., GE, X., WANG, K., LU, X. Cell culture medium as an alternative to conventional simulated body fluid, *Acta Biomaterialia*, 2011, vol. 7, pp. 2615.
- [115] ROHANOVA, D., BOCCACCINI, A. R., HORKAVCOVA, D., BOZDECHOVA, P., BEZDICKA, P., ČASTORÁLOVÁ, M. Is non-buffered DMEM solution a suitable medium for in vitro bioactivity tests?, *Journal of Materials Chemistry B*, 2014, vol. 2, pp. 5068.
- [116] TAS, A. C. The use of physiological solutions or media in calcium phosphate synthesis and processing, *Acta Biomaterialia*, 2014, vol. 10, pp. 1771.
- [117] GOLUNOVA, A., JAROŠ, J., JURTIKOVÁ, V., KOTELNIKOV, I., KOTEK, J., HLÍDKOVÁ, H., STREIT, L., HAMPL, A., RYPÁČEK, F., PROKS, V. N-(2-Hydroxypropyl) Methacrylamide Based Cryogels—Synthesis and Biomimetic Modification for Stem Cell Applications, *Physiological research/Academia Scientiarum Bohemoslovaca*, 2015, vol. 64, pp. S19.
- [118] GREGOROVÁ, E., PABST, W., ŽIVCOVÁ, Z., SEDLÁŘOVÁ, I., HOLÍKOVÁ, S. Porous alumina ceramics prepared with wheat flour, *Journal of the European Ceramic Society*, 2010, vol. 30, pp. 2871.
- [119] GUO, X., ZHOU, Z., MA, G., WANG, S., ZHAO, S., ZHANG, Q. Effect of forming process on the integrity of pore-gradient Al<sub>2</sub>O<sub>3</sub> ceramic foams by gelcasting, *Ceramics International*, 2012, vol. 38, pp. 713.
- [120] ZHAO, Y., JIANG, L., LIAO, Y., WANG, C., LU, J., ZHANG, J., LI, W. Low temperature degradation of alumina-toughened zirconia in artificial saliva, *J. Wuhan Univ. Technol.-Mat. Sci. Edit.*, 2013, vol. 28, pp. 844.
- [121] KELLER, T. S. Predicting the compressive mechanical behavior of bone, *Journal of biomechanics*, 1994, vol. 27, pp. 1159.
- [122] JIANG, H.-J., XU, J., QIU, Z.-Y., MA, X.-L., ZHANG, Z.-Q., TAN, X.-X., CUI, Y., CUI, F.-Z. Mechanical Properties and Cytocompatibility Improvement of Vertebroplasty PMMA Bone Cements by Incorporating Mineralized Collagen, *Materials*, 2015, vol. 8, pp. 2616.
- [123] GIANNOUDIS, P. V., DINOPOULOS, H., TSIRIDIS, E. Bone substitutes: an update, *Injury*, 2005, vol. 36 Suppl 3, pp. S20.
- [124] CALORI, G. M., MAZZA, E., COLOMBO, M., RIPAMONTI, C. The use of bone-graft substitutes in large bone defects: any specific needs?, *Injury*, 2011, vol. 42 Suppl 2, pp. S56.
- [125] JANICKI, P., SCHMIDMAIER, G. What should be the characteristics of the ideal bone graft substitute? Combining scaffolds with growth factors and/or stem cells, *Injury*, 2011, vol. 42 Suppl 2, pp. S77.
- [126] HANNINK, G., ARTS, J. J. Bioresorbability, porosity and mechanical strength of bone substitutes: what is optimal for bone regeneration?, *Injury*, 2011, vol. 42 Suppl 2, pp. S22.
- [127] BLOKHUIS, T. J., ARTS, J. J. Bioactive and osteoinductive bone graft substitutes: definitions, facts and myths, *Injury*, 2011, vol. 42 Suppl 2, pp. S26.

- [128] PIETAK, A. M., REID, J. W., STOTT, M. J., SAYER, M. Silicon substitution in the calcium phosphate bioceramics, *Biomaterials*, 2007, vol. 28, pp. 4023.
- [129] RAVEY, M., PEARCE, E. M. Flexible polyurethane foam. I. Thermal decomposition of a polyether-based, water-blown commercial type of flexible polyurethane foam, *Journal of Applied Polymer Science*, 1997, vol. 63, pp. 47.
- [130] CHATTOPADHYAY, D. K., WEBSTER, D. C. Thermal stability and flame retardancy of polyurethanes, *Progress in Polymer Science*, 2009, vol. 34, pp. 1068.
- [131] LEVCHIK, S. V., WEIL, E. D. Thermal decomposition, combustion and fire-retardancy of polyurethanes—a review of the recent literature, *Polymer International*, 2004, vol. 53, pp. 1585.
- [132] BILBAO, R., MASTRAL, J. F., CEAMANOS, J., ALDEA, M. E. Kinetics of the thermal decomposition of polyurethane foams in nitrogen and air atmospheres, *Journal of Analytical and Applied Pyrolysis*, 1996, vol. 37, pp. 69.
- [133] CAKIC, S., LACNJEVAC, C., RAJKOVIC, M., RASKOVIC, L., STAMENKOVIC, J. Reticulation of Aqueous Polyurethane Systems Controlled by DSC Method, *Sensors*, 2006, vol. 6, pp. 536.
- [134] CANGEMI, J. M., CLARO NETO, S., CHIERICE, G. O., SANTOS, A. M. D. Study of the biodegradation of a polymer derived from castor oil by scanning electron microscopy, thermogravimetry and infrared spectroscopy, *Polímeros*, 2006, vol. 16, pp. 129.
- [135] CIHLÁŘ, J., BUCHAL, A., TRUNEC, M. Kinetics of thermal decomposition of hydroxyapatite bioceramics, *Journal of Materials Science*, 1999, vol. 34, pp. 6121.
- [136] LIAO, C.-J., LIN, F.-H., CHEN, K.-S., SUN, J.-S. Thermal decomposition and reconstitution of hydroxyapatite in air atmosphere, *Biomaterials*, 1999, vol. 20, pp. 1807.
- [137] REID, J. W., PIETAK, A., SAYER, M., DUNFIELD, D., SMITH, T. J. N. Phase formation and evolution in the silicon substituted tricalcium phosphate/apatite system, *Biomaterials*, 2005, vol. 26, pp. 2887.
- [138] SAYER, M., STRATILATOV, A., REID, J., CALDERIN, L., STOTT, M., YIN, X., MACKENZIE, M., SMITH, T., HENDRY, J., LANGSTAFF, S. Structure and composition of silicon-stabilized tricalcium phosphate, *Biomaterials*, 2003, vol. 24, pp. 369.
- [139] LANGSTAFF, S., SAYER, M., SMITH, T., PUGH, S., HESP, S., THOMPSON, W. Resorbable bioceramics based on stabilized calcium phosphates. Part I: rational design, sample preparation and material characterization, *Biomaterials*, 1999, vol. 20, pp. 1727.
- [140] REID, J. W., TUCK, L., SAYER, M., FARGO, K., HENDRY, J. A. Synthesis and characterization of single-phase silicon-substituted  $\alpha$ -tricalcium phosphate, *Biomaterials*, 2006, vol. 27, pp. 2916.
- [141] MATHEW, M., SCHROEDER, L. W., DICKENS, B., BROWN, W. E. The crystal structure of  $[\alpha]\text{-Ca}_3(\text{PO}_4)_2$ , *Acta Crystallographica Section B*, 1977, vol. 33, pp. 1325.
- [142] AZA, D., LUKLINSKA, MARTINEZ, ANSEAU, GUITIAN, AZA, D. Morphological and structural study of pseudowollastonite implants in bone, *Journal of Microscopy*, 2000, vol. 197, pp. 60.
- [143] SCHWARTZWALDER, K., SOMERS, H., SOMERS, A. US3090094. Method of making porous ceramic articles, 1963.
- [144] MASTROGIACOMO, M., CORSI, A., FRANCIOSO, E., DI COMITE, M., MONETTI, F., SCAGLIONE, S., FAVIA, A., CROVACE, A., BIANCO, P., CANCEDDA, R. Reconstruction of extensive long bone defects in sheep using resorbable bioceramics based on silicon stabilized tricalcium phosphate, *Tissue engineering*, 2006, vol. 12, pp. 1261.

- [145] MELDRUM, M.,HOWDEN, P. <Ann Occup Hyg-2002-Meldrum-27-30.pdf>, *The Annals of Occupational Hygiene*, 2002, vol. 46, pp. 27.
- [146] FUBINI, B., ZANETTI, G., ALTILIA, S., TIOZZO, R., LISON, D.,SAFFIOTTI, U. Relationship between surface properties and cellular responses to crystalline silica: studies with heat-treated cristobalite, *Chemical research in toxicology*, 1999, vol. 12, pp. 737.
- [147] SCHWARTZWALDER, K., SOMERS, H.,SOMERS, A. Method of making porous ceramic articles. 1963.
- [148] LAI, W., GARINO, J.,DUCHEYNE, P. Silicon excretion from bioactive glass implanted in rabbit bone, *Biomaterials*, 2002, vol. 23, pp. 213.
- [149] TUCK, L., ASTALA, R., REID, J. W., SAYER, M.,STOTT, M. J. Dissolution and re-crystallization processes in multiphase silicon stabilized tricalcium phosphate, *Journal of Materials Science: Materials in Medicine*, 2008, vol. 19, pp. 917.
- [150] PORTER, A. E. Nanoscale characterization of the interface between bone and hydroxyapatite implants and the effect of silicon on bone apposition, *Micron*, 2006, vol. 37, pp. 681.
- [151] VANDIVER, J., DEAN, D., PATEL, N., BOTELHO, C., BEST, S., SANTOS, J. D., LOPES, M. A., BONFIELD, W.,ORTIZ, C. Silicon addition to hydroxyapatite increases nanoscale electrostatic, van der Waals, and adhesive interactions, *Journal of Biomedical Materials Research Part A*, 2006, vol. 78, pp. 352.
- [152] AZA, D. P. N., GUITIAN, F.,DE AZA, S. Bioactivity of wollastonite ceramics: In vitro evaluation, *Scripta Metallurgica et Materialia*, 1994, vol. 31, pp. 1001.
- [153] DUCKWORTH, W. Discussion of Ryshkewitch Paper by Winston Duckworth\*, *Journal of the American Ceramic Society*, 1953, vol. 36, pp. 68.
- [154] RYSHKEWITCH, E. Compression Strength of Porous Sintered Alumina and Zirconia, *Journal of the American Ceramic Society*, 1953, vol. 36, pp. 65.
- [155] PACE, A., VALENZA, A.,VITALE, G. Mechanical characterisation of human cancellous bone tissue by static compression tests *I materiali biocompatibili per la medicina/Biomaterials for Medicine: Atti del Convegno Nazionale della Società Italiana Biomateriali. Palermo, 2-4 luglio 2014*, 2014, pp. 15.
- [156] SOMANI, K. P., KANSARA, S. S., PATEL, N. K.,RAKSHIT, A. K. Castor oil based polyurethane adhesives for wood-to-wood bonding, *International Journal of Adhesion and Adhesives*, 2003, vol. 23, pp. 269.
- [157] PISZCZYK, Ł., STRANKOWSKI, M., DANOWSKA, M., HEJNA, A.,HAPONIUK, J. T. Rigid polyurethane foams from a polyglycerol-based polyol, *European Polymer Journal*, 2014, vol. 57, pp. 143.
- [158] HUNGER, M.,BROUWERS, H. J. H. Flow analysis of water–powder mixtures: Application to specific surface area and shape factor, *Cement and Concrete Composites*, 2009, vol. 31, pp. 39.
- [159] OU, S.-F., CHIOU, S.-Y.,OU, K.-L. Phase transformation on hydroxyapatite decomposition, *Ceramics International*, 2013, vol. 39, pp. 3809.
- [160] SOFRONIA, A. M., BAIES, R., ANGHEL, E. M., MARINESCU, C. A.,TANASESCU, S. Thermal and structural characterization of synthetic and natural nanocrystalline hydroxyapatite, *Material Science and Engineering C Materials for Biological Application*, 2014, vol. 43, pp. 153.
- [161] AMINI, A. R., LAURENCIN, C. T.,NUKAVARAPU, S. P. Bone Tissue Engineering: Recent Advances and Challenges, *Critical reviews in biomedical engineering*, 2012, vol. 40, pp. 363.

- [162] SHARMIN, E., ZAFAR, F. Polyurethane: An Introduction, 2012, p 8.
- [163] PAYTON, E. J. Revisiting Sphere Unfolding Relationships for the Stereological Analysis of Segmented Digital Microstructure Images, *Journal of Minerals and Materials Characterization and Engineering*, 2012, vol. Vol.11, pp. 22.
- [165] TAKAHASHI, J., SUITO, H. Evaluation of the accuracy of the three-dimensional size distribution estimated from the schwartz-saltykov method, *Metall and Mat Trans A*, 2003, vol. 34, pp. 171.
- [166] KIM, S., KIM, B., LIM, H. Effect of isocyanate index on the properties of rigid polyurethane foams blown by HFC 365mfc, *Macromol. Res.*, 2008, vol. 16, pp. 467.
- [167] KAIRYTĖ, A., VĖJELIS, S. Evaluation of forming mixture composition impact on properties of water blown rigid polyurethane (PUR) foam from rapeseed oil polyol, *Industrial Crops and Products*, 2015, vol. 66, pp. 210.
- [168] SZYCHER, M. *Szycher's Handbook of Polyurethanes, Second Edition*; CRC Press, 2012.

## LIST OF ABBREVIATIONS

2D	two dimensional
3D	three dimensional
3D-P	three dimensional powder based printing
AFM	atomic force microscopy
ATZ	alumina toughened zirconia
A/W	apatite / wollastonite
BCP	biphasic calcium phosphates
CAD	computer aided design
CaP	calcium phosphate
DCP	anhydrous dicalcium phosphate
DCPD	dicalcium phosphate dehydrate
HA	hydroxyapatite
HCA	hydroxy carbonate apatite
MDI	methylene diphenyl diisocyanate
MSC	mesenchymal stem cells
MTS	(3-(4,5-dimethylthiazol-2-yl)-5-(3-carboxymethoxyphenyl)-2-(4-sulfophenyl)-2H-tetrazolium)
MTT	methylthiazol tetrazolium
OCP	octocalcium phosphate
PA	polyamide
PCL	polycaprolactone
PEG	polyethylene glycol
PGA	poly(glycolic acid)
PMMA	polymethyl methacrylate
PLA	poly(lactid acid)
PLGA	copolymer PLA and PGA
PPF	poly(propylene fumarate)
pphp	parts per hundred parts of polyol
PSZ	partially stabilized zirconia
PU	polyurethane
SBF	simulated body fluid
SEM	scanning electron microscopy
SLM	selective laser melting
TCP	tricalcium phosphate
TEOS	tetraethyl orthosilicate
TEM	transmission electron microscopy
TZP	tetragonal zirconia polycrystal

## LIST OF FIGURES

- Fig. 1** Hierarchical structure of bone [10].
- Fig. 2** Major components of bone: (a) isolated apatite crystals [11]; (b) collagen fibril [13].
- Fig. 3** Structure of hydroxyapatite [16].
- Fig. 4** Collagen: from top to bottom—collagen  $\alpha$ -helix composed of amino acids, single triple-helical molecule, 2-dimensional section through part of a fibril showing the staggered array, a collagen fibril [13].
- Fig. 5** Fracture surface of human femur [11].
- Fig. 6** The prevailing toughening mechanisms from the nano to macro structure [12].
- Fig. 7** Scheme of bone remodelling process [32].
- Fig. 8** Schematic illustration of the bone healing process [24].
- Fig. 9** Classification of bioceramic implants according to the bioreactivity and time dependence of formation of bone bonding at an implant interface: (A) 45S5 Bioglass, (B) Mina13 Ceravital, (C) 55S4.3 Bioglass, (D) A/W glass-ceramics, (E) HA, (F) KGy213Ceravital, (G)  $\text{Al}_2\text{O}_3\text{-Si}_3\text{N}_4$  [36].
- Fig. 10** Phase diagram of bioglasses, 6 wt%  $\text{P}_2\text{O}_5$  [70].
- Fig. 11** Classification of processing methods by pore size [88-90].
- Fig. 12** Scheme of fabrication process by partial sintering [88].
- Fig. 13** The scheme of sacrificial fugitive method [89].
- Fig. 14** Gradient macroporous foam prepared from  $\beta$ -TCP and PMMA balls of 600-700  $\mu\text{m}$  [93].
- Fig. 15** Microstructure of porous HA samples with 64% porosity [95].
- Fig. 16** The scheme of replica technique [89].
- Fig. 17** Polyurethane sponge impregnated by bioglass [100].
- Fig. 18** SEM image of ceramics derived from oak [102].
- Fig. 19** Scheme of direct foaming [89].
- Fig. 20** Alumina foam prepared by direct foaming of emulsified ceramic powder suspensions [103].
- Fig. 21** Solid freeform fabrication: (a) CAD image of porous scaffold, (b) schematic drawing representing the 3D printing process [107].
- Fig. 22** Overview of the image analysis process: (a) acquired image, (b) threshold image, (c) applied watershed algorithm, (d) identified pores.
- Fig. 23** SEM image of HA layer created on the surface after immersion in the SBF [111].
- Fig. 24** A scheme of preparation of ceramic scaffold by replication technique: (a) PU template, (b) template coated by suspension, (c) sintered ceramic body
- Fig. 25** Rheological behaviour of 6 wt. % dispersal sol
- Fig. 26** Concentration dependence vs. rheological behaviour of fused alumina suspensions
- Fig. 27** Macrostructure of alumina foam (A7250)
- Fig. 28** Particle size distribution of alumina powders
- Fig. 29** Cross-section of alumina core (a) before soaking in Disperal sol and (b) after soaking in Disperal sol 168 h and (c) after 5 $\times$  soaking in Disperal sol for 5 hours – newly formed small alumina particles are visible in pores
- Fig. 30** Microstructure of alumina strut A725 (a) before soaking in Disperal sol; (b) after soaking in Disperal sol – newly formed small rounded alumina particles are visible in pores



- Fig. 31** Detail of core strut filled by synthetic alumina
- Fig. 32** Microstructure of composite (from right to left: alumina core, alumina shell and hydroxyapatite layer)
- Fig. 33** Surface of alumina / alumina / hydroxyapatite scaffold after 14 days immersion in SBF: (a) typical cauliflower like structure of newly formed apatite; (b) detail of thin lamellae.
- Fig. 34** Compressive strength of alumina foams reinforced by boehmite sol in dependence of various soaking times.
- Fig. 35** Compressive strength core-shell alumina composites. A725 – alumina core; A725\_R35 – alumina core / alumina shell (35 wt. %); A725\_R50 – alumina core / alumina shell (50 wt. %);
- Fig. 36** Fracture behaviour under applied stress: (a) separate fracture of individual struts; (b) fracture in the whole specimen volume
- Fig. 37** Thermal analysis of commercial boehmite sol Disperal P3
- Fig. 38**  $\zeta$ -potential as a function of pH for the dispersion Disperal P3.
- Fig. 39** Effect of shear rate and suspension concentration on viscosity
- Fig. 40** Dependence of porosity on the number of layers.
- Fig. 41** Structure of the bioactive coatings: (a) a strut with HA coating; (b) cross section of ATZ scaffold coated by HA; (c) cross section of ATZ scaffold coated by  $\beta$ -TCP.
- Fig. 42** Compressive strength of ATZ scaffolds
- Fig. 43** Microstructure of the substrates and coatings before and after soaking in SBF.
- Fig. 44** Cell line MG-63 adhered to the scaffold: (a) on inner struts; (b) on outer struts.
- Fig. 45** Cell density adhered on ATZ
- Fig. 46** Structure of calcium phosphate scaffolds sintered at 1200 °C/3 h: (a) template 90 ppi, (b) template 75 ppi
- Fig. 47** TA curves of commercial reticulated PU foam coated by HA-10SiO<sub>2</sub> suspension
- Fig. 48** X-ray diffraction patterns of scaffolds containing 5–20 wt. % SiO<sub>2</sub>, sintered at 1250 °C for 3h and HA sintered at 1200 °C for 3h
- Fig. 49** HA scaffolds sintered at 1200 °C/3h; porosity of the PU template: (a) 60 ppi, (b) 75 ppi, (c) 90 ppi
- Fig. 50** HA-10SiO<sub>2</sub> scaffolds sintered at 1250 °C/3h; porosity of the PU template: (a) 45 ppi, (b) 60 ppi, (c) 75 ppi, (d) 90 ppi
- Fig. 51** Strut morphology (a) hollow strut HA5SiO<sub>2</sub>, 75 ppi; (b) hollow strut HA, 75 ppi
- Fig. 52** Surfaces of HA-SiO<sub>2</sub> scaffolds before and after 3 day incubation in Eagle Medium.
- Fig. 53** MG 63 cells adhered to the surface of CaP / silica scaffolds: (a) 5% SiO<sub>2</sub>, (b) 10% SiO<sub>2</sub>, (c) 15% SiO<sub>2</sub>, (d) 20% SiO<sub>2</sub>
- Fig. 54** Percentage of adhered cells on the surface after 3D cultivation
- Fig. 55** Morphology of cells adhered to HA and HA – SiO<sub>2</sub> scaffolds. Please note the different scale bar in the first image.
- Fig. 56** Cell viability assessment after 24 hours of cultivation. Cells seeded on scaffolds exhibited green fluorescence indicating viable cells (Merged images of red and green fluorescence) for both materials: (a) CaP, (b) Si-CaP
- Fig. 57** Morphological features of the cells growing in calcium phosphate: (a) 60 ppi, (b) 75 ppi, (c) 90 ppi and Silica/calcium phosphate (d) 60 ppi, (e) 75 ppi, (f) 90 ppi scaffolds. Red color stains actin and the blue visualizes chromatin. White arrows indicate formation of filopodias, green arrows cells forming sheets over the pores of scaffolds.

- Fig. 58** Detail representation of cellular adhesion and spreading of adipose-derived stem cells on hydroxyapatite scaffold (porosity A-60, B-75, C-90) and hydroxyapatite-silicium (D-60, E-75, F-90). White arrows indicate formation of filopodias. Scale bar 200  $\mu\text{m}$ .
- Fig. 59** Dependence of compressive strength on total porosity
- Fig. 60** TA analysis of polyurethane composite (HA100\_2\_105)
- Fig. 61** TA analysis of commercial hydroxyapatite (Fluka)
- Fig. 62** XRD patterns of (a) commercial HA powder; (b) HA powder calcined at 800  $^{\circ}\text{C}$ ; (c) HA sintered at 1050  $^{\circ}\text{C}/2\text{ h}$ ; (d) at 1200  $^{\circ}\text{C}/2\text{ h}$  and (e) at 1350 $^{\circ}\text{C}/2\text{ h}$ .
- Fig. 63** Influence of water and powder content on total porosity after burning the polyurethane. Width of columns is growing in dependence on  $I_{\text{NCO}}$  from 75 to 105.
- Fig. 64** Processing of  $\beta$ -TCP scaffold (TCP74\_0.5\_95). From left to right: shaped  $\beta$ -TCP/PU composite, heat treated at 800  $^{\circ}\text{C}$  and sintered at 1350 $^{\circ}\text{C}/2\text{h}$ ; (b) scaffold sintered at 1200  $^{\circ}\text{C}/2\text{ h}$ .
- Fig. 65** Scaffold prepared from uncalcined powder: (a) CaP/PU composite after hardening (HAu 100\_4\_105), (b) samples containing 0, 2, 4 pphp sintered at 1050  $^{\circ}\text{C}$ , (c) SEM micrograph of HAU 100\_2\_105\_1200.
- Fig. 66** CaP/PU foams having ha/pu ratio = 1 and  $I_{\text{NCO}} = 105$  (water content increasing from 0 wt.% (left) to 5 wt% /(right) of polyol)
- Fig. 67** CaP/PU foams having ha/polyol ratio = 1 and  $I_{\text{NCO}} = 105$  (water content increasing from 0 wt.% (left) to 5 wt% /(right) of polyol)
- Fig. 68** Influence of water and powder content on porosity calculated from weight, dimensions and theoretical density of hydroxyapatite
- Fig. 69** Overview of cross sections of ceramic scaffolds sintered at 1050  $^{\circ}\text{C}$ : top row:  $m_{\text{HA}} = m_{\text{polyurethane}}$ , from 0 (left) to 5 pphp (right); bottom row:  $m_{\text{HA}} = m_{\text{polyol}}$ , from 0 (left) to 3 pphp (right)
- Fig. 70** Histograms of measured pore sizes: (a)  $m_{\text{HA}} = m_{\text{polyurethane}}$ ; (b)  $m_{\text{HA}} = m_{\text{polyol}}$
- Fig. 71** The dependence of isocyanate index on apparent porosity
- Fig. 72** An overview of prepared composites with different isocyanate index
- Fig. 73** Ceramic foams with different isocyanate index after heat treatment at 1050  $^{\circ}\text{C}/2\text{h}$
- Fig. 74** Microstructures of scaffolds with different isocyanate indexes ( $I_{\text{NCO}} = 75, 105, 125$ ),  $\text{HA/PU} = 100\%$ , 2 %  $\text{H}_2\text{O}$ , sintered at 1350  $^{\circ}\text{C}/2\text{ h}$
- Fig. 75** Effect of HA / PU ratio on apparent porosity ( $I_{\text{NCO}} = 105$ ; 2%  $\text{H}_2\text{O}$ )
- Fig. 76** Structure of prepared composites with different HA / PU ratio (2 %  $\text{H}_2\text{O}$ ,  $I_{\text{NCO}} = 105$ )
- Fig. 77** Microstructure of ceramic scaffolds at different HA/PU ratio: 0.51 on the left and 1 on the right (2 %  $\text{H}_2\text{O}$ ,  $I_{\text{NCO}} = 105$ , 1200  $^{\circ}\text{C}/2\text{h}$ )
- Fig. 78** Overview of scaffolds containing 4%  $\text{H}_2\text{O}$ : (a) ha/pu = 0.4, (b) ha/pu = 0.6, (c) ha/pu = 0.8
- Fig. 79** Micrographs of HA100\_2\_105 scaffold sintered at different temperatures: (a) HA/PU composite before calcination; (b) scaffold sintered at 1050  $^{\circ}\text{C}$ ; (c) 1200  $^{\circ}\text{C}$ ; (d) 1350  $^{\circ}\text{C}$  (the magnification is the same for all 4 photos).
- Fig. 80** Microstructures of HA100\_2\_105 scaffold sintered at different temperatures: (a) HA/PU composite before calcination; (b) scaffold sintered at 1050  $^{\circ}\text{C}$ ; (c) 1200  $^{\circ}\text{C}$ ; (d) 1350  $^{\circ}\text{C}$  (the magnification is the same for all 4 photos).
- Fig. 81** Compressive stress dependence on time of loading

## LIST OF TABLES

- Table 1** Young's modulus of bone and its components (GPa) [26-29].
- Table 2** Strength of bone [26, 27].
- Table 3** Mechanical properties of bioinert ceramics [52, 53]
- Table 4** Mechanical properties of bioglass and glass-ceramics [73].
- Table 5** Mechanical properties of calcium phosphates [74].
- Table 6** Polymer templates and their characterisation
- Table 7** Types of PVA and their molecular weight and degree of hydrolysis
- Table 8** Nominal ion concentrations (in mM) of SBF in comparison to the human blood plasma [110].
- Table 9** Composition of suspensions used for alumina scaffolds ("A" in sample identification refers to core suspension, "D" and "R" refers to shell layers)
- Table 10** Composition of suspensions used for ATZ scaffolds
- Table 11** Compositions of HA/SiO<sub>2</sub> suspensions
- Table 12** Compositions of studied composite foams
- Table 13** Summary of obtained porosities and densitis of foam composites
- Table 14** Porosity, strut thickness, cell size and pore size of ATZ scaffolds
- Table 15** Phases present in the scaffolds after heat treatment at 1200 °C (HA) and 1250 °C (HA-SiO<sub>2</sub>)
- Table 16** Crystallographic parameters of pure and silicon substituted calcium phosphate phases
- Table 17** Theoretical density of scaffold components
- Table 18** Pore sizes of HA-SiO<sub>2</sub> and HA
- Table 19** Linear shrinkage of scaffolds after sintering at 1250 °C/3h
- Table 20** Scaffold composition and total porosity at different temperatures
- Table 21** Pore sizes estimated from cross section of scaffolds sintered at 1050 °C/2 h